SIMULATION OF EXTREME RAINFALL AND FLOOD EVENTS IN WEST AFRICA

BY
NIMON POUWEREOU
B.Sc, M.Sc (Meteorology)
MET/19/3753

A Thesis in the Department of Meteorology and Climate Science, School of Earth and Mineral Sciences, submitted to the School of Postgraduate Studies, in partial fulfillment of the requirements for the award of Doctor of Philosophy in Meteorology and Climate Science of The Federal University of Technology, Akure, Nigeria

MAY, 2023

DECLARATION

I hereby declare that this Thesis was written by me and is a correct record of my own research work. It has not been presented in any previous application for any degree of this or any other University. All citations and sources of information are clearly acknowledged by means of references.

Candidate's Name: NIMON POUWEREOU

Signature: Date:

CERTIFICATION

We certify that this Thesis entitled "Simulation of Extreme Rainfall and Flood Events in West Africa" is the outcome of the research carried out by NIMON POUWEREOU under the West African Science Service Center on Climate Change and Adapted Land-Use Doctorate Research Programme in West African Climate Systems (WASCAL DRP-WACS) in the Department of Meteorology and Climate, The Federal University of Technology, Akure.

Dr. A. Akinbobola - - - - - - - - - - - - - - - - - - -
(Major Surpervisor) Signature Date
Department of Meteorology and Climate Science,
Federal University of Technology,
Akure, Nigeria

Dr. B. J. Abiodun - - - - - - - - - - - - - - - - - - -
(Co-Surpervisor) Signature Date
Environmental and Geographical Science,
University of Cape Town,
South Africa

Prof. H. Kunstmann - - - - - - - - - - - - - - - - - - -
(Advisor) Signature Date
Institute of Geography,
University of Augsburg, Germany

Prof. Zachariah Debo Adeyewa - - - - - - - - - - - - - - - - - - -
(Director) Signature Date
Doctoral Research Program – West African Climate Systems
West African Science Service Center on Climate Change and Adapted Land Use (DRP-WACS, WASCAL),
Federal University of Technology,
Akure, Nigeria.

ABSTRACT

It is well known that extreme rainfall events that usually devastate the socio-economic activities in West Africa are inadequately simulated by many conventional uniform-grid global climate models, but little is known about how well they are simulated by the emerging variable-resolution global climate models. The present study examines the performance and sensitivity of the Model for Prediction Across Scales-Atmosphere (MPAS-A or simply 'MPAS') in simulating extreme rainfall characteristics over West Africa. Eight indices were used to characterise extreme events. Firstly, the uniform grid version of MPAS (60km resolution) was applied to simulate global climate for the period 1981–2010, and the capability of the model was quantified to capture the characteristics of extreme rainfall events over that period. Secondly, a series of simulations were performed with the variable-grid version of the model to study the sensitivity of the simulated extreme rainfall events to local enhancements in model resolution (i.e., 15km, 10km, and 3km) over West Africa, using two cases of extreme rainfall over the Oti River basin. The results show that MPAS gives a realistic simulation of the spatial distribution of most of the eight extreme rainfall indices with a high pattern correlation coefficient ($r>0.8$). However, the model overestimates the magnitude of some indices (e.g., the annual number of wet days and the maximum number of consecutive wet days) over the Guinea highlands and along the Guinea coast and Cameroon Mountain and underestimates others over the entire region. The local refinement of model resolution improves its performance in simulating extreme rainfall events over the river basin. The results of the study have applications in improving and implementing MPAS for extreme rainfall predictions over West Africa.

Floods are among the most destructive natural disasters with associated adverse impacts on society and the environment, and the present study also assesses the capability of

HEC-RAS model version 6.1 in simulating flood events in Mango along the Oti River in Togo. Actual flood events in October 2020 were initially simulated as a model verification, and hypothetic modeling scenarios were simulated to explore the effects of fluvial and combined fluvial and pluvial floods over selected areas A and B. The results indicate that HEC-RAS gives a realistic simulation of the flood extent, which agrees with the local topography. However, while the model underestimates the expanse in some parts of the simulation area, it overestimates it in others, especially in areas A and B. In addition, the combined fluvial and pluvial floods aggravate the impacts of the events over the two areas, as the flood extent and depths are more significant than the ones produced by a single type of flooding. The results of the study have applications in improving and implementing HEC-RAS for flood events predictions over West Africa.

Keywords: Extreme rainfall event, Global climate model, MPAS-A, Oti River basin, Flood Event, Hydraulic model, HEC-RAS

DEDICATION

This Thesis is dedicated to the Almighty GOD, the giver of knowledge, understanding, and wisdom, who made it possible for this research to be successfully executed and to all taxpayers whose money is used to support research and development in developing countries.

ACKNOWLEDGEMENT

The German Federal Ministry of Education and Research (BMBF) primarily funded this research through the West African Science Service Center on Climate Change and Adapted Land-Use Doctorate Research Programme in West African Climate Systems (WASCAL DRP-WACS) host in the Federal University of Technology Akure, Nigeria.

I am grateful to my Major Supervisor, Dr. A. Akinbobola, Co-Supervisor, Dr. Babatunde J. Abiodun, and Advisor, Prof. H. Kunstmann, for their encouragement, constructive criticism, insightful suggestions, and comments throughout the conduct of this research.

I would like to thank my colleagues and friends at the University of Cape Town (UCT). A special thanks to the Atmospheric Science peer-review group led by my wonderful Co-Supervisor, Dr. Babatunde J. Abiodun, for reading, analysing, and debating our work together - it was both collegiate and helpful.

TABLE OF CONTENTS

LIST OF TABLES

LIST OF FIGURES

LIST OF EQUATIONS

LIST OF ABBREVIATIONS

AEJ	Africa Easterly Jet
AEW	Africa Early Waves
ARW	Advanced Research WRF model
CAPE	Convective Available Potential Energy
CFSR	Climate Forecast System Reanalysis
Copernicus-EMS	Copernicus Emergency Management Service
COSMO-CLM	COSMOS Climate Limited-area Model
CAM-EULAG	Community Atmospheric Model EULAG Dynamic core
CHIRPS	Climate Hazards Group InfraRed Precipitation with Station data
CMIP6	Coupled Model Intercomparison Project Phase 6
CMIP5	Coupled Model Intercomparison Project Phase 5
CIN	Convective Inhibition
DD	Dynamical Downscaling
DEM	Digital Elevation Model
DWE	Diffusion Wave Equations
EMDAT	Emergency Events Database
ECHO	European Union Humanitarian Office
ECHAM5	European Centre Hamburg Model
ECMWF	European Center for Medium-Range Weather Forecasts
FAO	Food and Agriculture Organization
FV3-GFDL	Finite-Volume on a Cubed-Sphere Model - Geophysical Fluid Dynamics Laboratory
GCMs	Global Climate Models
GFS	Global Forecast System

GIS	Geographic Information System
GDP	Gross Domestic Product
GRB	Gambia River Basin
GFDL-ESM4	GFDL Earth System Model
HEC-RAS	Hydrologic Engineering Center's River Analysis System
HadRM3P	Hadley Centre regional climate model
HPC	High-Performance Computing
ITCZ	Intertropical Convergence Zone
ITD	Intertropical Discontinuity
MAE	Mean Absolute Error
MCS	Mesoscale Convective System
MIROC6	Model for Interdisciplinary Research on Climate Version 6
MSE	Mean Square Error
MPAS	Model for Prediction Across Scale
NMHS	National Meteorological and Hydrological Services
NOAA	National Oceanic and Atmospheric Administration
NWP	Numerical Weather Prediction
OCHA	Office for the Coordination of Humanitarian Affairs
ORB	Oti River Basin
RegCM3	Regional Climate Model Version 3
RCA4	Rossby Centre Regional Climate Model Version 4
RCM	Regional Climate Model
SD	Statistical Downscaling
SWE	Shallow Water equations
STD	Standard Deviation

TEJ	Tropical Easterly Jet
VGCM	Variable Grid Climate Model
WA	West Africa
WERE	Widespread Extreme Rainfall Events

CHAPTER ONE

1.0 INTRODUCTION

1.1 BACKGROUND OF THE STUDY

The climate of West Africa is influenced by two main air masses. The first is a warm, moist, tropical maritime air mass that carries moisture inland from the Atlantic Ocean and is responsible for most of the rainfall in the region. This air mass reaches its northernmost extent between 18 and 21 °N in July or August (FAO, 1985). The second air mass is a hot, dusty, dry continental air mass that originates from the Sahara high-pressure system and blows from the northeast over the area (FAO, 1985; Nicholson 2008, 2009). This air mass creates hot and arid conditions over land and moves southwards, reaching its southernmost position over the Guinea zone in January between 5 and 7 degrees north. Both air masses contribute significantly to the temperature and rainfall variability in West Africa. The meeting point of the two air masses is called the Inter-Tropical Convergence Zone (ITCZ) over the ocean and the Intertropical Discontinuity (ITD) over land (Abiodun et al., 2008; Nicholson 2008, 2009). The ITD reaches its southernmost position at about 7 degrees north in January over the Guinea zone and around 22 degrees north in August over the Sahel (Peter and Tetzlaff, 1988). The above discussed systems, constitute the monsoon circulation which is the prevailing rainfall-producing system in West Africa and provides about 75% to 90% of the total rainfall in the region (Hagos and Cook, 2007a). However, multiple dynamical atmospheric rainfall-producing features such as monsoon flow, African Easterly Jet (AEJ), Tropical Easterly Jet (TEJ), African Easterly Waves (AEW), and Mesoscale Convective Systems (MCS) modulate the rain-producing systems over West

Africa (Fortune 1980; Gaye et al., 2005) and may even lead to extreme rainfall in the region (Laurent et al., 1998; Fink et al., 2006).

Extreme rainfall is one of the most devastating weather events that threatens human life and property. In West Africa, extreme rainfall often induces floods that cause severe damage, loss of property and death (Engel et al., 2017b; Balogun et al., 2019; Balogun et al., 2021). For example, on 1 September 2009, an extreme rainfall event in Ouagadougou (Burkina Faso) produced more than 263 mm of rainfall within ten hours, induced floods that destroyed property, damaged roads, displaced 150,000 people and killed nine people. In 2007 alone, extreme rainfall-induced floods displaced more than one million people and killed 500 in Burkina Faso, Togo, Mali and Niger (Di Baldassarre et al., 2010). Over the period 1981–2014, extreme rainfall events affected more than 2.3 million people, rendered nearly half a million people homeless and killed more than 3,000 (Engel et al., 2017a; Guha-Sapir et al., 2016; EMDAT, 2015). Meanwhile, several studies have indicated that global warming may increase the frequency and intensity of extreme rainfall over West Africa in the future (Akinsanola and Zhou, 2019; Diedhiou et al., 2018). For example, Sylla et al. (2016) projected a future increase of about 40% in extreme rainfall intensity in most countries in West Africa, while other countries are projected to experience a lower increase of about 20%. Similarly, Vizy and Cook (2012) projected an increase in the number of extreme rainfall days of 10–30% between April and October over West Africa. Accurate weather forecasts from global climate models (GCMs) and regional climate models (RCMs) can help reduce the devastating impacts of extreme rainfall events by providing reliable early warning information to foster better decision-making and preparation against these events. However, there remains a large degree of uncertainty regarding the reliability of the current climate models in simulating extreme rainfall over West Africa. For instance,

many Global Climate Models (GCMs) have low horizontal resolutions that cannot effectively capture the regional or local atmospheric processes responsible for extreme rainfall, making it necessary to utilise Regional Climate Models (RCMs) for more precise local predictions (Sylla et al., 2016; Køltzow et al., 2011; Salathé et al., 2010; Abiodun et al., 2017). Though the extensive usage of RCMs has improved the simulation of extreme rainfall over the region (Akinsanola and Zhou, 2019), there are still some limitations related, for example, to the lateral boundary condition problems, which compromise the quality of the simulated regional or local scale features.

An alternative approach to address the issues concerning GCMs and RCMs raised previously is by using variable-resolution or stretch-grid GCMs (hereafter VGCMs), for regional climate research (Fox-Rabinovitz et al., 2008; Fox-Rabinovitz et al., 2001; Abiodun et al., 2011; Maoyi et al., 2021). According to Maoyi et al. (2021) and Abiodun et al. (2011) the use of VGCM illustrates the benefits over contemporary GCMs in modeling various climatic characteristics over the Southwest Indian Ocean and over West Africa respectively. Nevertheless, as the development and application of VGCMs for regional research are still relatively recent, further research is required to assess their reliability in modeling extreme rainfall events over West Africa.

Though, skillful VGCMs may help improve the forecast of the extreme rainfall events, it is important to assess how these events could affect the West African communities in terms of flood, which is crucial for flood early warning system in West Africa. Indeed, flood is a natural process that occurred when the water rises to overflow land that is not normally submerged (Ward, 1978). Those lands are sometimes referred as floodplain. Floods are one of the most disastrous hazards that threaten socioeconomic activities worldwide. In the last 20 years, it accounted for 43% of all disasters and has impacted the world's highest population (EM-DAT, 20015; CRED, 2015). The socio-

economic impacts of floods are usually more devastating in developing countries, especially in West Africa, where poor communities are more vulnerable. In West Africa, floods often cause colossal damage by demolishing infrastructures, damaging agricultural products, and killing people (Tschakert et al., 2010; Komi et al., 2017; Wagner et al., 2021). For example, in 2007, West Africa recorded the worst flooding it had ever faced in 30 years. In Togo, the event affected more than 125000 people, displaced 13700, and killed 23 people. The same event also affected 93000 people, displaced 28000, and killed 46 in Burkina Faso (Tschakert et al., 2010). In 2010, flood events greatly impacted the West African community, affecting 1.6 million people and killing 307, and in Togo alone, they caused damages and losses worth over $38 million (Ntajal et al., 2016). In October 2020, flood events badly affected the Oti River basin in Togo, rendering 57 thousand people and killing 11 (EM-DAT, 2020; ECHO, 2020; Copernicus-EMS, 2020). Although flood events affecting West Africa result from multiple factors, rainfall events are the most important and remain the trigger. Recent studies (Sylla et al., 2016; Mukherjee et al., 2018) highlight that global warming may increase the frequency and intensity of heavy rainfall, and the loss of lives and economic damages may escalate. However, skillful forecasts of heavy rain and associated flood events may reduce the socioeconomic impacts of these events. While most flood early warning systems in WA countries usually rely on rainfall forecasts, there is not much effort put in place to translate those heavy rain forecasts into flood hazards forecasts, especially in National Meteorological and Hydrological Services (NMHS), which may help society, policymakers, and humanitarian agencies make effective emergency response plans. Hence, there is a need to extend rainfall forecasts to flood hazard and risk forecasts.

1.2 STATEMENT OF PROBLEM

The application of climate models is useful for studying extreme events at global and regional scales and, more importantly, extreme rainfall events and their associated features over West Africa. Despite significant advancements in climate modeling, there is still a considerable level of uncertainty surrounding the accuracy of current climate models in simulating extreme rainfall events across West Africa. These uncertainties could influence the accuracy of the model outputs and, thus, hinder using findings derived from model results to make and implement sound economic plans and policies. In addition, studies have shown that many GCMs often have low horizontal resolutions, which can lead to inadequate representation of the regional and local atmospheric processes that drive extreme rainfall events. Other sources of errors from RCMs are related to the lateral boundary condition problems. All these factors limit the accuracy of representing the atmospheric phenomenon of interest and, thus, influence the simulation of extreme rainfall events for reliable information in extreme rainfall-induced flood events. For these reasons, studies have introduced and applied Global Climate Models (GCMs) with variable-resolution or stretch-grid capabilities. Despite the promising advancements and emerging applications of Variable-Grid Climate Models (VGCMs) in regional climate studies, further research is required to assess their efficacy and accuracy in predicting extreme rainfall occurrences across West Africa. On the other hand, for reliable early flood warning information, it is essential to translate the forecast of extreme rainfall into flood hazards and risk forecasts. Hydraulic modeling has emerged as a viable method for predicting and mitigating flood hazards and risks in recent times. Most studies on inland flood hazards in Africa are based on either fluvial or pluvial floods. Other studies showed that extreme rainfall often generates both pluvial and fluvial floods and that considering the individual flood type may underestimate the

potential damages. Therefore, assessing flood events by considering the combined fluvial and pluvial flood is more relevant for flood hazards and risk forecasts.

1.3 AIM AND OBJECTIVES

1.3.1 Aim

The aim of this study is to evaluate the capability of the MPAS model in simulating extreme rainfall, as well as evaluate the performance of the HEC-RAS model in simulating flood events in West Africa.

1.3.2 Objectives

The Specific objectives of the research are to:

(i) evaluate the performance of the Model for Prediction Across Scale (MPAS) in simulating the extreme rainfall characteristics over West Africa;

(ii) assess the sensitivity of the MPAS model in simulating two extreme rainfall events over the Oti River Basin (ORB) in Togo, West Africa;

(iii) examine the performance of the Hydrologic Engineering Center and River Analysis System model (HECRAS) in simulating actual flood events over the Oti River Basin (ORB); and

(iv) assess the composite of pluvial and fluvial flood risk over the ORB using the HECRAS model.

1.4 JUSTIFICATION

The rationale behind this research is to identify a global climate model with stretched-grid capability and a hydraulic model whose output can be used as an integral input to provide sound climate information that will guide policy formulation and decision-making in climate-related sectors of the economy at the national and regional

scale. Model evaluation, application, and development are the most vital areas explored in past and present-day research, particularly in a data-sparse region like Africa. It is, therefore, critical to constantly evaluate the available models, which are subjected to modifications and regular updates. More so, there has been more demand for reliable simulation of extreme rainfall and flood events because of the recurrent flood hazards and their projected increase in frequency and intensity (Sylla et al., 2016; Mukherjee et al., 2018). In recent years, few studies have provided important information on variable-resolution or stretched-grid GCMs (VGCMs), which enable smooth resolution transitions and achieve high resolution in specific regions of interest (Kramer et al., 2018; Skamarock et al., 2010; Du et al., 1999; Ringler et al., 2008; nevertheless, none studies tested the capability of VGCMs in simulating extreme rainfall over West Africa. Also, it is crucial to extend the severe rainfall forecast to the flood hazard and risk forecasts, which is essential for flood early warning information in West Africa. Hence, there is a need for the current study to consolidate previous work by providing a comprehensive evaluation of VGCMs and hydraulic models on extreme rainfall and flood events simulation.

1.5 THE CONTRIBUTION OF THE RESEARCH TO KNOWLEDGE

The outcome of this research will be helpful for the model development community in pinpointing the specific areas of model structures that require modification for enhancing model outputs. Also, to close the gaps in our scientific understanding of how the variable-resolution GCMs simulate extreme regional rainfall and how the hydraulic model can be applied to flood hazard and risk forecasts. Using this information, policymakers can make informed decisions and develop robust policies to improve sustainable economic planning and promote climate-resilient development.

Additionally, these measures will mitigate risks and challenges faced by crucial sectors of the economy, including agriculture, water resources, public health, energy, and other weather-sensitive industries.

CHAPTER TWO

2.0 LITERATURE REVIEW

This chapter comprehensively reviews the modeling of extreme rainfall and flood events studies. It starts by reviewing the three main methods used to identify and define extreme rainfall in the literature and summarizes the findings of previous studies on the capability of climate models (Global and Regional Climate models) to simulate extreme rainfall. It also summarises the findings of previous studies on the capability of hydraulic models to simulate flood events over Western Africa.

2.1 SIMULATION OF EXTREME RAINFALL EVENTS USING CLIMATE MODELS

2.1.1 Identification of Extreme Rainfall Events

There is no unique definition for extreme rainfall events, as previous studies have adopted different methods to define extreme rainfall events (e.g., Tarhule, 2005; Barnston and Mason, 2011). These methods use the characteristics of extreme rainfall events to identify or use the impacts of extreme rainfall events to detect the events. For instance, Groisman et al. (2001) and Klein Tank and Zwiers (2009) defined and identified extreme rainfall events based on the characteristics of the events (i.e., frequency, persistence, intensity, and amplitude). In contrast, Tarhule (2005) and Barnston and Mason (2011) defined and identified extreme rainfall events based on the devastating and destructive impacts of the event on society. Though this study has used two methods in determining extreme rainfall (threshold values and percentiles), the review in this section discusses the three main methods as identified by Groisman et al. (2001). These methods are return periods, threshold values, and percentiles.

2.1.2 The Return-Period Method

Several studies have given different attributes for return-period methods (e.g., Sanderson, 2010; Chu et al., 2009). For instance, Sanderson (2010) indicated that the return period is the frequency of an event, while the magnitude of the associated rainfall event is called the return value. Chu et al. (2009) and Vezzoli et al. (2012) referred to the return period, also known as the recurrence interval, as the average gap (in years) between rainfall events of a given magnitude or more significant. This method, common among building engineers and hydrologists, has been used to describe the characteristics of extreme events in different parts of the world. With this method, Sanderson (2010) used 46 years to calculate the return value of daily rainfall events over 40 towns and cities in the United Kingdom. Melice and Reason (2007) applied the method over a 65-year data series to estimate the frequency of the occurrence of destructive rainfall in George (South Africa). Over West Africa, Panthou et al. (2012) estimated the frequency of extreme rainfall events with a 100-year return value in the Central Sahel Zone using the return period. The main shortcoming of this method is that it requires a long rainfall time series. Sanderson (2010) shows that applying the return period method on a short-time rainfall series may lead to high return value uncertainty.

2.1.3 Identifying Extreme Rainfall Events Using Threshold Values

The threshold values for identifying extreme rainfall are widely used, and the method is well established in the literature (e.g., Groisman et al., 2001; Dyson et al., 2009; Zhang et al., 2011). This method identifies an extreme event over an area using a rainfall threshold value suitable for the area. Any rainfall amounts equal to or greater than the threshold value is considered an extreme event. Because of its simplicity (compared to the return period), this method is widely used and preferred to the return-

period approach. For example, Panthou et al. (2014) used threshold values of 30.0- and 60.0-mm day^{-1} to identify and study the characteristics of extreme rainfall events in the north and south of the Central Sahel, respectively. Hountondji et al. (2011) applied a threshold value of 79.6 mm day-1 to obtain extreme rainfall events over 21 stations in Benin for the period 1960-2000. Groisman et al. (2001) studied the spatial distribution of heavy rain events over the United States using 100 mm day-1 at a 1° x 1° grid resolution. However, some studies (i.e., Dyson et al., 2009; Zhang et al., 2011; Abba Omar, 2014) have pointed out that this method has a significant weakness. The weakness is that, as various regions of the world receive different amounts of rainfall and require different threshold values, it is challenging to compare extreme rainfall events over the areas. Moreover, Klein Tank and Zwiers (2009) and Zhang et al. (2011) showed that the threshold value method is inappropriate for the spatial comparison of extreme rainfall distribution over an area or a region.

2.1.4 Percentile Values

To overcome the shortcomings of the threshold-values method, some studies have used the percentile-values method in identifying an extreme rainfall event (i.e., Grimm and Tedeschi, 2009; Abiodun et al., 2013; Ly et al., 2013). For example, Ly et al. (2013) defined an event as extreme rainfall if it is equal to or above the 99th percentile of daily precipitation in the Sahel zone of West Africa. Likewise, Abiodun et al. (2013) described the spatial distribution of extreme rainfall events using the 99.5th percentile of daily rainfall over Nigeria. Moreover, other studies employ a different approach to applying this method. For example, Grimm and Tedeschi (2009) defined extreme rainfall using the mean of three consecutive rainfall days above the 90th percentile distribution. Moreover, Yabi and Afouda (2012) identified any year with a 20% increase

in annual total rainfall above the yearly mean rainfall as an extreme rainfall year over Benin. However, the percentile value method is more valuable than the return period or threshold values. This is because there is an even distribution of the days equal to or greater than the set percentile. Furthermore, unlike the return period method, this method does not need a long-term dataset and applies to all regions (Klein Tank & Zwiers, 2009; Zhang et al., 2011; Abba Omar, 2014). Moreover, this method is suitable for evaluating the changes in event characteristics, intensity, and frequency and allows the spatial comparison of complex topography over a region such as West Africa (Zhang et al., 2011). Therefore, of these three methods described above, the percentile-threshold method is the most appropriate for the present study. Thus, following Crétat et al. (2014), the present study used the 95th percentile of daily rainfall to define an extreme rainfall event over West Africa. The implementation of the method for this study is detailed in Chapter Three.

2.1.5 Favorable Atmospheric Conditions for Extreme Rainfall Events in West Africa

Several studies have identified different processes that favor extreme rainfall in West Africa (Reed et al., 1977; Fortune, 1980; Lavaysse et al., 2006, Pathe et al., 2009). For instance, Pathe et al., 2009 attribute heavy rainfall over West Africa to warm SST conditions over the Tropical Atlantic Ocean and El Nino conditions over the Pacific Ocean. On the other hand, Reed et al. (1977), Fortune (1980), and Lavaysse et al. (2006) attribute the phenomenon to the complex interaction and variability in rainfall-producing features in the WAM systems (i.e., MCSs, AEJ, TEJ, and AEWs). While Nicholson (2008 and 2009) found that an increase in the strength of TEJ usually leads to an increase in extreme rainfall in the West African Sahel, Laurent et al. (1998) and

Fink et al. (2006) found that more MCSs lead to more extreme rainfall in the Sahel. Furthermore, Ruti and Dell' Aquila (2010), Abatan (2011), and Crétat et al. (2014) have reported a strong link between extreme rainfall and AEWs in West Africa. Their findings revealed that extreme rainfall strongly depends on the wave pattern of the AEWs. Crétat et al. (2014), in particular, found a link between extreme rainfall and the two AEWs types (3-5 days and 6-9 days wave periods) over West Africa. Furthermore, the study showed that the 3-5 days AEWs mainly account for extreme rainfall over West Africa (especially south of latitude 15°N). Also, some studies argued that most of the heavy rainfall in West Africa comes from MCSs and that these MCSs are usually embedded in the AEWs (Fink and Reiner, 2003; Fink et al., 2006; Crétat et al., 2014). Hence, understanding the thermodynamic conditions associated with these atmospheric circulations is crucial to understanding the characteristics of extreme rainfall over West Africa. Therefore, the emphasis of the present study will be on understanding the link between the thermodynamic conditions and extreme rainfall in West Africa.

2.1.6 Simulating Extreme Rainfall Events using Global Climate Models (GCMs)

Global climate models (GCMs) are a complex mathematical representation of the major climate system components (atmosphere, land surface, ocean, and sea ice) and their interactions. They are accredited tools for climate simulation. Some studies have discussed the performance of Global Climate Models (GCMs) in simulating the characteristics of extreme rainfall events over West Africa (Faye and Akinsanola, 2022; Klutse et al., 2021; Kamiguchi et al., 2006; IPCC, 2007; Vigaud et al., 2009; Crétat et al., 2013; Niang et al. 2014). For example, Sow et al. (2020) showed that most CMIP5 global models capture relatively well the annual cycle of the fraction of precipitation accounted by the very wet days R95ptot, while Klutse et al. (2021) showed that in some

cases, CMIP6 global models capture the frequency of heavy rainfall in the region. Also, Faye and Akinsanola (2022) found that the CMIP6 global models reasonably reproduce the patterns of extreme rainfall indices over the WA region. Furthermore, Crétat et al. (2013) found that three out of the four GCMs in their study simulated a realistic magnitude of intense rainfall over Africa. However, while GCMs may be skillful in rainfall at the global or continental scale, they cannot resolve the regional circulation patterns that lead to extreme hydrological events like extreme rainfall events at the regional scale due to their coarse horizontal resolution (Christensen and Christensen, 2003). Giorgi et al. (2001), Wang et al. (2004), and Rummukainen (2010) pointed out that GCMs' low and coarse horizontal resolution results in their inability to simulate the finer scale regional and local forcings (e.g., complex terrain and topography, land-ocean contrasts) that controls the regional climate. Giorgi et al. (2009) argued that the low resolution of the GCMs hinders them from simulating extreme events that are important to climate information users. Sylla et al. (2012) and Crétat et al. (2013) also found that GCMs failed to correctly reproduce key features of the local atmospheric circulation due to the low resolution of the models. These shortcomings are a significant source of uncertainty in simulating extreme rainfall characteristics, frequency, and intensity over West Africa (Cook and Vizy, 2006; Sylla et al., 2012; Crétat et al., 2013). For instance, Crétat et al. (2013) stated that GCMs simulations often overestimate extreme rainfall's frequency (and underestimate the intensity) over West Africa. In light of these shortcomings, downscaling, a method to improve outputs from GCM outputs, was initiated to meet the increasing demand for climate variability and projection at a regional scale (Endris et al., 2015). Downscaling, a means of acquiring small-grid scale information from fields with lower resolution, provides decision-makers with the needed information for impact assessment at a local scale in connection with

information from the GCMs (Benestad, 2008). Two approaches to downscaling are reported in the literature: Statistical and Dynamical downscaling.

2.1.7 Statistical Downscaling

Previous studies have used Statistical Downscaling (SD) to obtain regional climate information from GCMs (e.g., Hewitson and Crane, 1996; Di Vittorio and Miller, 2013). SD is used to establish a statistical correlation between global scale climate variables (surface pressure) and local climate variables such as rainfall of an area (Endris et al., 2015). The relationship is used to acquire regional climate information by mapping it to GCM data (Hewitson and Crane, 1996). According to Di Vittorio and Miller (2013), the SD method adopts the statistical relationships between low-resolution GCM or RCM data and the point measurement at an observation station. Statistical relationships are estimated for a calibration period, validated separately, and applied for another period assuming temporal stationarity (Di Vittorio and Miller, 2013). Furthermore, regional information can be obtained using the equations to downscale GCM outputs. This involves using the equations to investigate the differences between global and local or regional climates. Abiodun et al. (2013) statistically downscaled different GCMs simulations and found an increase in the frequency of extreme rainfall days across the ecological zones of Nigeria due to global warming. Goswani et al. (2006) revealed that significant spatial contradictions and the inability to account for the topographic effects on extreme rainfall events are some of the defects of the SD technique. Hence, discarding the geomorphology of the study area makes SD inappropriate for forecasting extreme rainfall events (Goswani et al., 2006).

2.1.8 Dynamical Downscaling

Several studies have documented the dynamic downscaling (DD) techniques for providing regional information from GCMs (i.e., Wang et al., 2004; Seth et al., 2007; and Endris et al., 2015). Unlike SD, the DD method applies conservation laws to provide regional climate information over the chosen domain about climate variability and change projections via numerical models (Endris et al., 2015). In this technique, a GCM provides an initial condition and a continuous lateral boundary condition to an RCM's integration, while the RCM provides the finer-scale regional information. Many studies have used the DD technique to provide regional climate information for different purposes, including climate predictability studies (Lawal et al., 2015), seasonal climate prediction (Wang et al., 2004), climate change projection (Giorgi and Mearns, 1991 and Giorgi, 2006), and the impact of land-cover change on projected future climate (Abiodun et al., 2012; Naik and Abiodun, 2016). The technique has also been successfully used in West Africa for climate-change studies (Vigaud et al., 2009; Diallo et al., 2012). For example, Diallo et al. (2012) employed the DD approach to project future changes in precipitation and temperature over West Africa for the early twenty-first century, using four RCMs (RegCM3, RCA, REMO, and HadRM3P) to downscale two GCM (ECHAM5 and HadCM3) outputs. Some of the advantages of the DD method are that it captures atmospheric processes like rainfall induced by topography and uses coarse resolution GCMs output to provide higher-resolution information up to 10-50 km (Giorgi et al., 2009), as well as the fact that it responds to different external forcings and does not assume temporal stationarity in the SD method (Endris et al., 2015).

2.1.9 Simulating Extreme Rainfall Events using Regional Climate Models (RCMs)

Studies have shown that using RCMs has improved our knowledge about the different interactions among the atmospheric features that induce extreme rainfall at regional or local scales (Jenkins et al., 2005; Moufouma-Okia and Rowell, 2010; Sylla et al., 2011; Browne and Sylla, 2012). For instance, Crétat et al. (2013) showed that the nesting of RCM (WRF 3.5) reproduces spatial and temporal characteristics of extreme rainfall events as the observed datasets over Africa. Also, Sylla et al. (2012) and Haensler et al. (2013) successfully applied RCM to reveal how topography can induce extreme rainfall in West Africa, showing RCMs' ability to capture and resolve complex topography. Akinsanola and Zhou (2018) showed that RCA4 and COSMO-CLM RCMs represent observed extreme rainfall patterns over the WA region and add significant value to the driven GCMs. But RCM downscaling usually involves lateral boundary condition problems and prevents the two-way interactions between larger scales and regional scale features, as a result, compromising the quality of the simulated regional or local scale features (Michaelis et al., 2019; Small et al., 2014; Marbaix et al., 2003).

The need to address this problem has led to the introduction and application of variable-resolution or stretch-grid GCMs (hereafter VGCMs) for regional climate studies (M. Fox-Rabinovitz et al., 2008; M. Fox-Rabinovitz et al., 2001; Abiodun et al., 2011; Maoyi et al., 2018). For example, Maoyi et al. (2018) applied VGCM (called CAM-EULAG) to give a realistic climate simulation over the Southwest Indian Ocean, and Abiodun et al. (2011) demonstrated the advantages of VGCM over the contemporary GCMs in simulating various atmospheric features in West Africa. Nevertheless, given that the developments and applications of VGCMs for regional

studies are still relatively new, there is a need for more studies on their reliability in simulating extreme rainfall events over West Africa.

2.1.10 Example of Stretched-Grid Global Climate Models (VGCMs)

2.1.10.1 Finite-Volume on a Cubed-Sphere Model (GFDL FV3)

In 2016, NOAA built one of the world's best global weather models, a priority for the agency and the nation. In addition, NOAA announced the selection of a new dynamic core, the engine of a numerical weather prediction model, and has begun developing a state-of-the-art global weather forecasting model to replace the U.S. Global Forecast System (GFS). The latest global model is also called the GFS. As with the current GFS, the latest GFS developed one run in the background of NOAA's suite of weather and climate models improving skill across all NOAA's forecast mission areas.

The new dynamic core, Finite-Volume on a Cubed-Sphere (FV3), was developed by NOAA's Geophysical Fluid Dynamics Laboratory in Princeton, New Jersey. The FV3 core has brought a new level of accuracy and numeric efficiency to the model's representation of atmospheric processes, such as air motions. This makes possible simulations of clouds and storms at resolutions not yet used in a global operational model. In addition, FV3 improves the representation of small-scale weather features such as hurricanes while maintaining the quality of large-scale global circulation. The FV3 core enables the model to provide localized forecasts for several weather events simultaneously, all while generating a global forecast every six hours. Looking ten years ahead, the GFS model with the FV3 core can run in higher resolution and zoom in (Figure 2.1) on smaller and smaller storm systems to provide forecasters with better pictures of how storms will evolve.

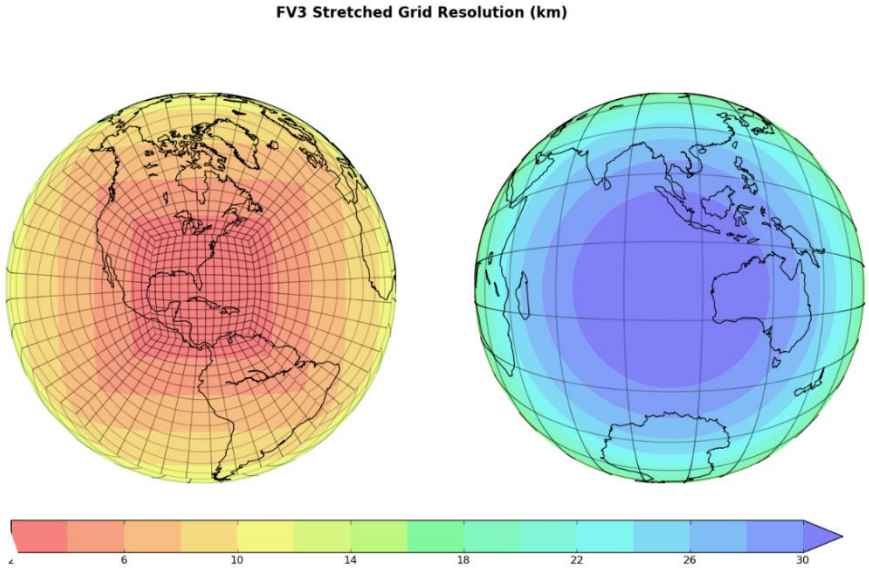

Figure 2.1: An example of FV3's capability to zoom in on critical weather events. The model resolution has been enhanced to represent better hurricanes threatening the Southeastern US. The reverse side is a coarser resolution because it is less concerned. Source: NOAA to develop new global weather model | National Oceanic and Atmospheric Administration

2.1.10.2 Models employing stretched spherical coordinates

The formulation of three global grid-point atmospheric models, GOES-SG, GEM, and LMDZ, is based on spherical coordinates. These models incorporate a stretching technique similar to the approach proposed by Staniforth and Mitchell (1978) for numerical weather prediction on a hemispheric polar stereographic grid. A fine-resolution window, typically with a grid spacing of approximately 0.5°, is present in all three models. The resolution degrades to about 2° in the far field along each grid axis. The buffer region between the inner window and the far field is characterized by a constant rate of longitude and latitude degradation, up to 10% per grid point, until the desired coarse grid spacing is attained in the far field. As Caian and Geleyn (1997) suggested in their study of ARPEGE, more aggressive stretching factors may be utilized for short-term numerical weather prediction applications.

Figure 2.2 presents a stretched spherical grid, which has a comparable number of points in its fine-resolution window, as an illustration. In this example, a far-field resolution of 2.715° is defined, and the buffer zone grid length increases at a rate of 4% per cell. The total number of grid points for this stretched spherical grid example is 34,632. Notably, models utilizing stretched spherical grids often have approximately twice the number of grid points compared to a Schmidt-transformation model that encompasses a similar high-resolution region (typical values are reported by Fox-Rabinovitz et al., 2006). Although this increases the computational cost, it may offer some benefits for the simulations due to the less coarse grid cells in the far-field region. Furthermore, the independent longitudinal and latitudinal grid-stretching may result in a lack of isotropy in the cells in the coarse region; however, no associated detrimental behavior has been reported.

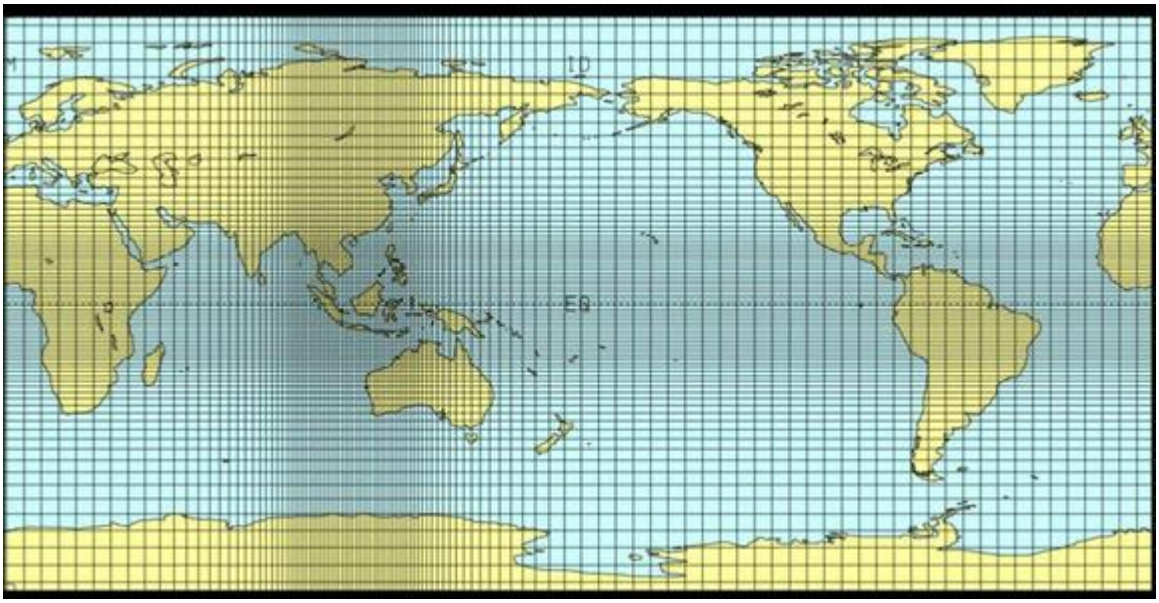

Figure 2.2: Example of a stretched spherical grid having resolution of 0.56° over the central region increasing to 2.43° afar, plotting every second grid line. Source: John L. McGregor, 2013.

2.1.10.3 Model for Prediction Across Scales-Atmosphere (MPAS-A)

The MPAS atmospheric component utilizes an unstructured centroidal Voronoi mesh and C-grid staggering state variables for horizontal discretization in fluid flow solvers. The variable resolution meshes are capable of smoothly varying transitions, which is demonstrated in Figure 2.3. This feature is believed to address issues commonly associated with traditional mesh refinement strategies, such as abrupt transitions in one-way and two-way grid nesting. The flexible MPAS meshes allow researchers to pursue high-resolution numerical weather prediction NWP) and regional climate applications, in addition to global uniform-resolution NWP and climate applications. The MPAS atmospheric dynamical core addresses the fully compressible non-hydrostatic equations of motion. The horizontal Voronoi mesh, depicted to the right, uses a C-grid staggering of the state variables (Figure 2.4). The normal velocity on Voronoi cell faces defines the horizontal velocity u, while the remaining state variables are defined at the cell centers. The triangular mesh displayed in dashed lines in the figure represents the Voronoi mesh's dual. The variable resolution meshes are mostly hexagonal, although pentagons and heptagons are sometimes present. The C-grid-staggered Voronoi mesh's significant advancements are detailed in Thuburn et al. (2009) and Ringler et al. (2010).

The numerical schemes implemented in the MPAS atmospheric component closely resemble those utilized in the Advanced Research WRF model. However, there are notable distinctions between the two models. For example, the ARW model uses rectangular meshes and hydrostatic pressure (mass) vertical coordinates. In contrast, MPAS adopts a vector-invariant format for the horizontal momentum equation and a complete version of the WRF transport scheme detailed in Skamarock and Gassmann, (2011).

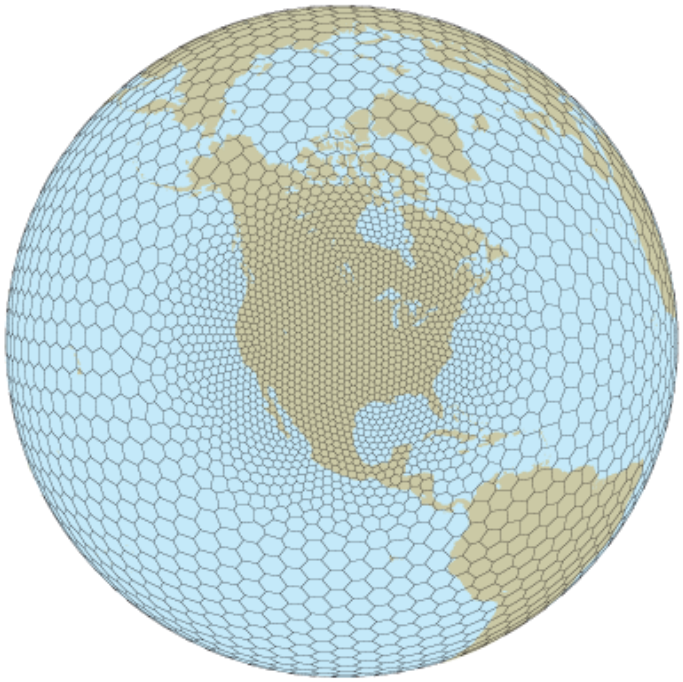

Figure 2.3: A variable resolution MPAS Voronoi mesh. Source: MPAS Home page

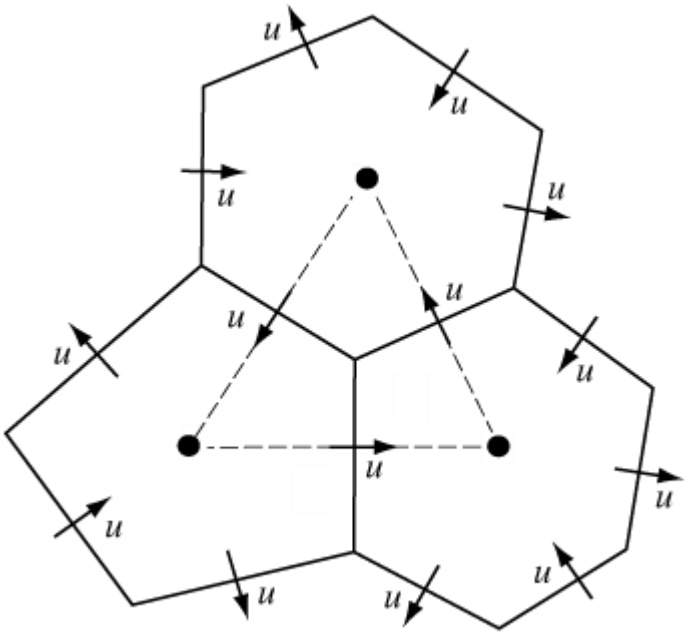

Figure 2.4: C-grid staggered variables on the horizontal Voronoi mesh. Normal velocities are defined on the cell faces and all other scalar variables are defined at the cell centers. Vertical vorticity is defined at the cell vertices. Source: MPAS Home page

2.1.11 Simulation of extreme rainfall characteristics using MPAS-A model

Model for Prediction Across Scales (hereafter MPAS), which uses unstructured variable resolution meshes that allow for smooth resolutions transition towards the desired high resolution in the region of interest (Kramer et al., 2018; Skamarock et al., 2010; Du et al., 1999; Ringler et al., 2008), is an example of the new VGCMs. Studies have employed the MPAS model to simulate and study different atmospheric features that produce extreme precipitation over various regions of the world (Michaelis et al., 2019; Zhao et al., 2019; Kramer et al., 2018). For instance, Davis et al. (2016) used two configurations of the MPAS model (15 km uniform and 60-15 km variable meshes) to simulate the characteristics of a tropical cyclone in the eastern North Pacific. Huang et al. (2017) applied the model at 15 km resolution to study the track of typhoon Morakot and the associated extreme rainfall over Taiwan. Zhao et al. (2019) also used it to simulate the characteristics of extreme rainfall events over East China. While Kramer et al. (2020) used it to simulate three severe weather events in Europe, Schwartz (2014) used it to assess the characteristics of diurnal precipitation over the United States. Despite the wide usage of the MPAS model across the world, only one study (Heinzeller et al., 2016) has tested the reliability of MPAS simulation over West Africa, and the focus of the study was not on extreme rainfall events. Hence, to harness the potential MPAS model for early warning systems over West Africa, there is a need for information on how well the model simulates the characteristics of extreme rainfall over the sub-continent.

2.2 SIMULATION OF FLOOD EVENTS USING HYDRAULIC MODELS

2.2.1 Overview on Flood

Floods occur naturally when the water rises and overflows onto land that is not usually submerged, also known as floodplains (Ward, 1978). They are one of the most destructive natural threats to life on Earth, and sometimes they are human-made (Ohl et al., 2000). Inundations, which are submerged lands from overflowing rivers and lakes, occur when water overflows or breaks levees. Floods can also arise from the sea due to high tides and in otherwise dry areas due to the accumulation of heavy rainfall. Different types of floods can be categorized based on their source and the processes involved. Examples include river floods, flash floods, dam-break floods, ice-jam floods, glacial-lake floods, urban floods, coastal floods, and hurricane-related floods. Climate, precipitation, temperature, and landscape are the main drivers and modulators of most types of floods (Shroder et al., 2015).

2.2.2 Hydrologic Modeling

Hydrological simulation has been in use since the 1850s, and it has undergone rapid development in modeling because of the easy accessibility of powerful software (Singh, 2018). Flood modeling simplifies actual events by simulating natural flood occurrences using input data, hydraulic properties, and boundary conditions of a specific area. For example, a flood model can be created for a particular river basin based on different boundary conditions or input information, which may affect the model's performance. In addition, flood risk activity and hydraulic properties can be estimated and calculated over a specific period by simulation. Hodges (2009) defines Hydrodynamic modeling as "the art and science of applying conservation equations for

momentum, continuity, and transport to represent evolving velocity, density, and scalar fields." This modeling offers insights into spatial and temporal changes in physical processes that may be observed but are less apparent in field data (Hodges, 2014).

Hydrodynamic models are a valuable tool for creating flood hazard maps, and researchers can use numerical, physical, or historical data mapping methods to develop these maps. Numerical modeling is a popular choice among hydrologists due to its ability to simulate real-world events efficiently, even with limited data, and at a lower cost than physical modeling. Physical modeling can also be helpful in flood hazard mapping, especially in areas where significant social and economic damage is likely. Historical data mapping is useful for calibrating parameters in numerical models (Bellos, 2012). Hydrodynamic models are mathematical models that attempt to reproduce fluid movement by solving formulas based on physics rules. Simulations can be classified as 1D, 2D, or 3D depending on their spatial representation of floodplain streams (Teng et al., 2017).

In recent years, hydraulic modeling has proved to be a practical approach for flood hazard and risk forecasts. It provides flood extent, depth, and velocity, which are essential for flood risk management (Pinos & Timbe, 2019; Rangari et al., 2019; Ongdas et al., 2020). Studies have used different hydraulic models to assess flood hazards in different regions of the world (e.g., Pinos and Timbe, 2019; Ntajal et al., 2016; Sharma & Regonda, 2021; Iroume et al., 2022; Komi et al., 2017). For example, Komi et al. (2017) used LISFLOOD-FP hydraulic model to assess flood extent along the Oti river in northern Togo, West Africa. Using the HEC-RAS model, Iroume et al. (2022) investigated the major urban flood in Douala (Cameroon). Pinos and Timbe (2019) used four different hydraulic models (HEC-RAS, Iber, Flood Modeller, and PCSWMM) to generate flood inundation maps for comparison in the Santa Barbara River in the

Ecuadorian Andes. Rangari et al. (2019) also used HEC-RAS to generate the depth of urban flood inundation of Hyderabad in India. Nevertheless, studies have discussed the advantages of using 1D and 2D hydraulic models in simulating different flood events (Gharbi et al., 2016; Mangukiya and Yadav, 2022; Manfreda et al., 2015). While the 1D hydraulic models accurately represent the channel processes, the 2D hydraulic models are well designed to assess the flood wave dynamics in the floodplain when the channel capacity has exceeded, and the flow is spread across a large area in the downstream terrain (Ongdas et al., 2020; Mihu-pintilie et al., 2019; Shustikova et al., 2019). Other studies have argued that 2D hydraulic models are mainly used for flood extent mapping and flood risk estimation because they provide more detailed and reliable results in complex flow simulations(Teng et al., 2017; Lea et al., 2019). In addition, Lea et al. (2019) showed that the 2D models that solve full shallow water equations can accurately simulate the timing and duration of inundation. Despite the wide usage of hydraulic models to assess flood hazards, few studies have conducted hydraulic modeling in assessing flood hazards in Togo, especially along the Oti river (e.g., Komi et al., 2017), and the focus was on 1D modeling. Hence, to improve the accuracy of flood mapping and the early warning systems in this region of WA, there is a need for more flood hazard assessment using 2D hydraulic modeling.

Most studies on inland flood hazards in Africa are based on either pluvial or fluvial floods (Ntanganedzeni & Nobert, 2021; Komi et al., 2017). For example, simulating the stream flow data, Ntanganedzeni and Nobert (2021) assessed flood risk hazards along the Luvuvhu river in Limpopo province in South Africa. Considering fluvial floods, Komi et al. (2017) assessed the flood hazard extent over the Oti river basin in Togo, West Africa. However, Tiepolo et al. (2021) argued that flood hazard assessments often fail to meet disaster risk reduction needs locally because they usually

consider only one type of hazard (pluvial or fluvial floods). For instance, Chen et al. (2010) showed that extreme rainfall often generates both pluvial and fluvial floods and that considering the individual flood type may ~~considerably~~ underestimate the potential damages. To improve flood hazard assessment and meet disaster risk reduction needs, studies suggested and assessed inland compound floods hazards, that is, the combination of pluvial and fluvial floods, in different parts of the world (Chen et al., 2010; Apel et al., 2016; Patra et al., 2016). For instance, applying the coupled hydraulic models, Chen et al. (2010) and Apel et al. (2016) simulated the combined pluvial and fluvial flood events in urban areas at Bradford (UK) and Can Tho city, respectively. Láng-Ritter et al. (2022) investigated the impact of the inland compound floods (fluvial and flash floods) in southeast Spain to enhance decision support. Also, Patra et al. (2016) modeled the combined flow in the drain and rainfall-induced catchment flooding to develop a flood inundation map in northern India. Even though several studies have investigated inland compound floods and the fact that it is relevant for disaster risk reduction, none have been done over the Oti river basin in Togo. Even though, Komi et al., 2017 conducted flood modeling study in the Oti river basin in Togo, the study focused only on the fluvial flood. Hence, there is a need of a combined fluvial and pluvial floods study along Oti river in Mango.

2.2.3 Overview on HEC-RAS model

In the early 1990s, the Hydrologic Engineering Center developed a suite of Windows-based software applications called HEC-RAS, the first computer program. As HEC's flagship software, it replaced HEC-2 and could perform water surface profile computations. HEC-RAS's capabilities have expanded significantly over the years, with earlier versions only allowing for 1D steady-state analysis. In January 2001, Version 3.0

was released, which added 1D unsteady flow computations (Dewberry, 2016). The most recent version of HEC-RAS, Version 5.0, was released in 2016 and allowed for two-dimensional unsteady flow calculations.

2.2.3.1 One-Dimensional Steady and Unsteady Modeling

In its early versions, HEC-RAS could compute water surface profiles for channels with the steady-state gradually varied flow. A Steady-state refers to a situation where the channel's discharge remains constant over time. Gradually varied flow conditions indicate that the water surface elevations do not change significantly over distance. To determine water surface profiles in 1D steady-state, the program applies the Conservation of Energy from one cross-section to the next along the channel's length, using the Standard Step Method.

In natural channels, it is uncommon for the flow to be steady or constant. Instead, the flow rate varies over time, which is referred to as unsteady flow. Unsteady flow routing is the process of determining depths and flows at different locations within the channel at different times. This implies that velocity, discharge, and depths depend on both location (distance along the stream channel) and time. Figure 2.5 depicts this scenario, where at time t, Cross-Section A has a specific discharge and depth, while at time $t+\Delta t$, the same location may have a different discharge and depth. With unsteady flow routing, it is possible to determine the depth and discharge at numerous locations at different points in time.

The Saint-Venant equations, also known as the shallow water equations, were formulated by Barre de Saint-Venant in the late 1800s to solve 1D unsteady flow routing problems. These equations are derived from applying the principles of Conservation of

Mass (Equation 2.1) and Conservation of Momentum (Equation 2.2) to a small control volume of fluid, as explained by Brunner (2016).

$$\frac{dA_T}{dt} + \frac{dQ}{dx} - q = 0 \qquad \textbf{Equation 2.1}$$

$$\frac{dQ}{dt} + \frac{dQV}{dx} + gA\left(\frac{dZ}{dx} + S_f\right) = 0 \qquad \textbf{Equation 2.2}$$

Where A is the area of cross-section, t is a time, Q is the flow, X is the distance along the channel, q is a source or sink term, V is a velocity of flow, g is the gravity acceleration, S_f is the friction slope and dz/dx is the water surface slope.

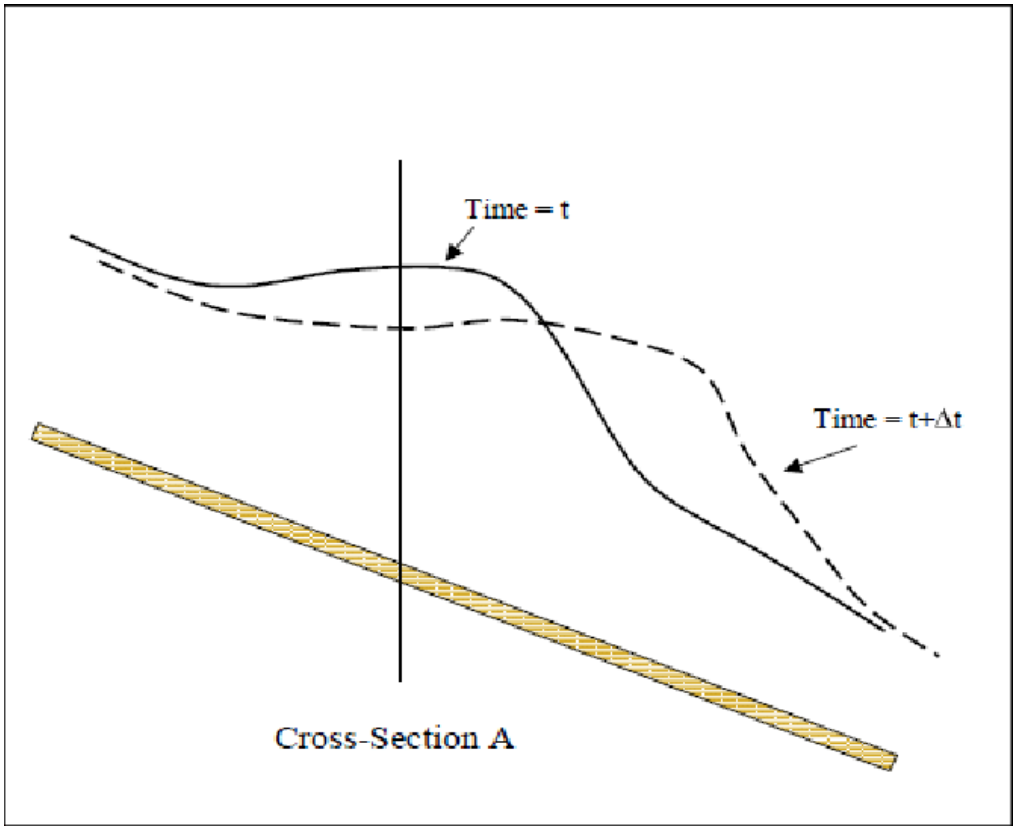

Figure 2.5: An Unsteady Flow Routing Concept (Chase, 2016)

2.2.3.2 Two-Dimensional Unsteady Modeling

In 2D modeling, the river and adjacent floodplain areas are divided into individual cells called grid cells, 2D flow cells, or computational grid cells. This process involves discretizing the area into a collection of cells with elevation and roughness data to represent the ground surface and friction effects. HEC-RAS uses the sub-grid bathymetry approach, which involves multiple GIS cells within each grid cell, as illustrated in Figure 2.6. Each GIS cell has a unique elevation, and the collection of grid cells makes up the terrain model. The terrain model defines the continuous ground geometry necessary for analyzing floodplains with two-dimensional behavior.

A cell face is an interface between two grid cells, consisting of ground elevations from the GIS cells. In hydraulic terms, a cell face is equivalent to a cross-section, as depicted in Figure 2.7. Since the ground geometry is available through the GIS cell information, hydraulic properties such as cross-sectional area, wetted perimeter, hydraulic radius, and conveyance can be calculated for any water surface elevation. Moreover, the topography within a grid cell allows for the development of a relationship between the storage volume in the cell and the water surface elevation, known as a stage storage curve. Therefore, the model computes a water surface elevation at each grid cell for each point in time, with the grid cells' size determining the model's resolution and results.

In general, HEC-RAS 2D permits varying water surfaces along any transect, unlike its 1D counterpart which only accommodates a single surface per cross-section. Furthermore, the 2D mesh is significantly more intricate than the cross-sections integrated in the 1D version, thereby lending the 2D results a more sophisticated appearance. Hence, this study aims the use of HEC-RAS 2D in simulating flood event over the study area.

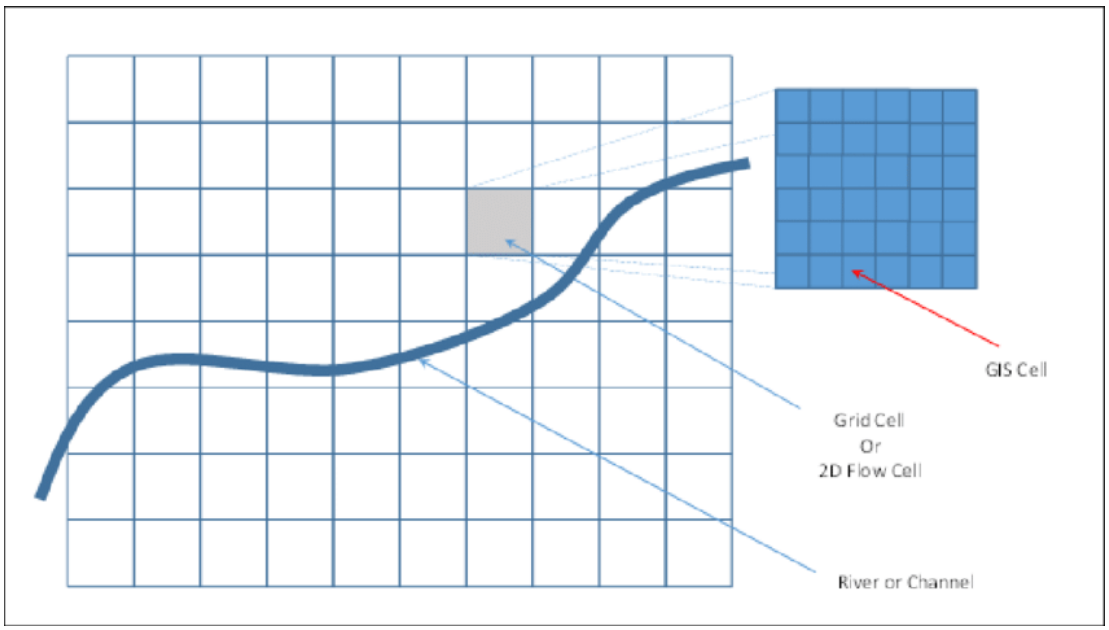

Figure 2.6: Grid Cells and GIS Cells

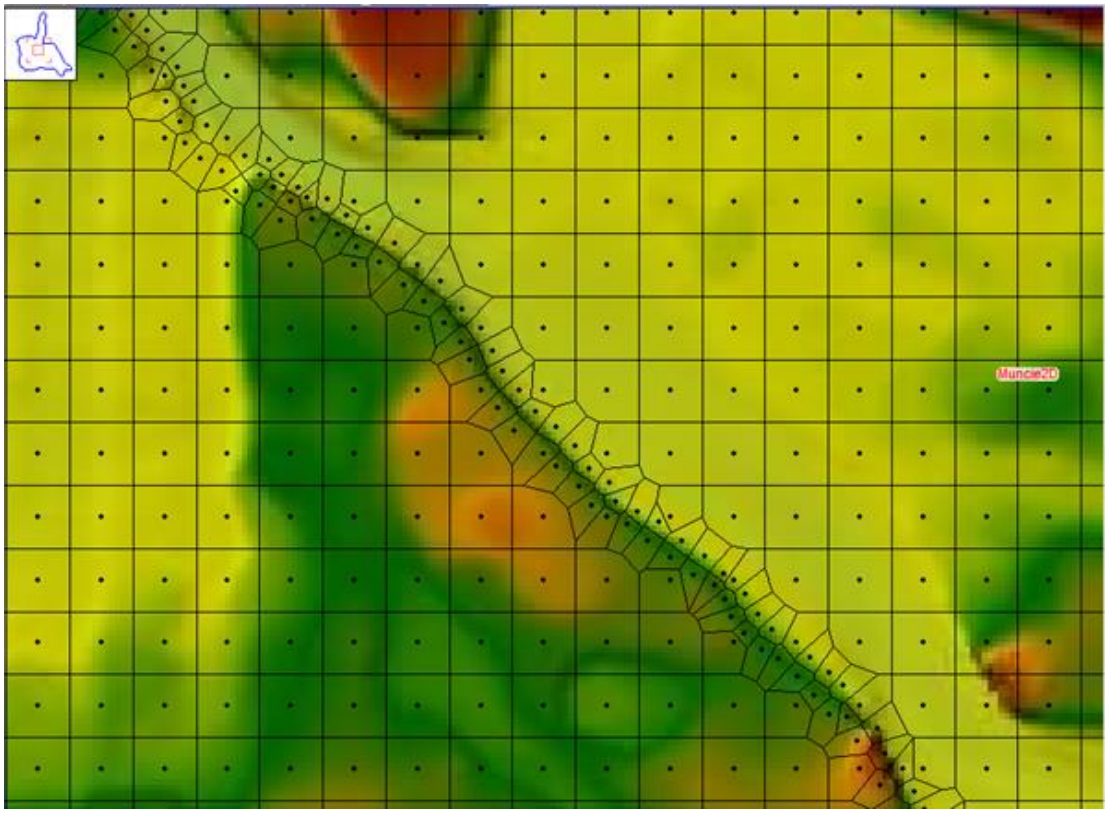

Figure 2.7: Ground Geometry at Cell Face

2.3 GAP IN LITERATURE

West African communities face varying degrees of risk from extreme rainfall-induced flood events. Therefore, high-quality scientific research is crucial to understand better the characteristics and impacts of these events on the region's environment and economy, and thus help reduce their consequences by providing reliable warning information. Long-term observations and measurements of weather and climate parameters such as temperature, rainfall, relative humidity, wind speed, direction, and their derivatives are key to understanding the region's climate. Unfortunately, observation networks in West Africa are sparse, making it challenging to comprehend the underlying drivers of climate. Reanalysis datasets and satellite products have emerged in recent decades, providing valuable insights into some atmospheric processes. While these products have contributed significantly to our understanding of extreme events, they cannot predict how the region's weather or climate system will respond to future changes, highlighting the need for climate models.

Global Climate Models (GCMs) can simulate various atmospheric phenomena. For example, they can assess extreme rainfall-induced flood events at different spatial and temporal scales, historically or for future conditions (Sylla et al., 2013). However, studies have shown that the horizontal resolution of most Global Climate Models (GCMs) is inadequate in representing regional or local atmospheric processes responsible for extreme rainfall events. As a result, the use of Regional Climate Models (RCMs) is necessary to obtain more precise information at the local level. But RCMs also have limitations. One of their main issues is that they can be affected by lateral boundary condition problems, which can hinder two-way interactions between larger scales and regional-scale features. This can compromise the quality of the simulated

regional or local scale features, as noted by Michaelis et al. (2019), Small et al. (2014), and Marbaix et al. (2003).

In response to this issue, variable resolution or stretch-grid GCMs (VGCMs) have been introduced and applied for regional climate studies. Studies have shown the ability of VGCMs to simulate the climate over the Southwest Indian Ocean realistically and demonstrated the benefits of their usage in simulating various atmospheric features in West Africa compared to contemporary GCMs. However, since the development and application of VGCMs for regional studies are still relatively new, more research is necessary to assess their reliability in simulating extreme rainfall events over West Africa.

The Model for Prediction Across Scales-Atmosphere (MPAS) is a new type of Variable Grid Climate Model (VGCM) that uses unstructured variable resolution meshes to achieve high resolution in specific regions of interest and enable smooth resolution transitions. Numerous studies have employed the MPAS model to simulate and study different atmospheric features that lead to extreme precipitation over various world regions. For example, researchers have used the model to study tropical cyclones in the eastern North Pacific, track Typhoon Morakot and the associated extreme rainfall over Taiwan, and simulate the characteristics of extreme rainfall events over East China. While the model has been widely used worldwide, only one study has tested its reliability over West Africa, and that study did not focus on extreme rainfall events. Therefore, further research is necessary to explore the MPAS model's potential for providing early warning information over West Africa to examine how well the model simulates extreme rainfall characteristics in the subcontinent. Hence, there is a need to evaluate the performance of a VGCM called Model for Prediction Across Scale-

Atmosphere (MPAS) to simulate extreme rainfall events, focusing on the widespread extreme rainfall events in West Africa and the associated atmospheric circulations.

On the other hand, for a relevant early warning system related to extreme rainfall-induced flood events is vital to translate the extreme rainfall forecasts into flood forecasts which are essential for flood hazard mapping. Hydraulic modeling has emerged as a practical approach for flood hazard and risk forecasting in recent years. This method offers critical flood-related information, including flood extent, depth, and velocity, essential for effective flood risk management. Though several studies have used different hydraulic models to assess flood hazards in other regions, only a few have been done in Togo, especially along the Oti River (e.g., Komi et al., 2017), and the focus was on 1D modeling. In addition, the majority of studies on inland flood hazards in Africa focus on either pluvial or fluvial floods; and according to Tiepolo et al. (2021), flood hazard assessments frequently fail to address local disaster risk reduction needs as they tend to concentrate on a single type of flood hazard (pluvial or fluvial floods). Even though several studies have investigated the combined fluvial and pluvial floods in other regions, studies have yet to be done over the Oti River basin in Togo. Komi et al (2017) are the only study on flood hazards in the Oti River basin in Togo (Komi et al., 2017) and only the fluvial flood was considered. Hence, the present study uses the HEC-RAS 2D hydraulic model to simulate different scenarios of inland compound flood events, focusing on the Oti river in Mango, Togo (West Africa).

CHAPTER THREE

3.0 MATERIALS AND METHODS

3.1 STUDY AREA

3.1.1 Study area for climate model simulation

The area selected for the climate model simulation in this study is the West Africa region (20°W–25°E; 0°–25°N) with a focus on the Oti River and Gambia River basins (Figure 3.1). While most of the Oti River basin is located in the Savanna climate zone, the Gambia River basin (GRB) is in the Sahel climate zone. These basins were selected because, as transboundary areas, they each play a crucial role in the socio-economic activities of the region.

The Oti River basin is a sub-basin of the Volta basin in West Africa, with an estimated area of about 72,000 km2. It is shared among four countries (Ghana, Burkina Faso, Benin and Togo) and lies between 7° and 12.3° latitude North and between longitude 0.5°W and 2.5°E (Kwawuvi et al., 2022; Amisigo et al., 2015). The movement of the Inter-tropical Discontinuity (ITD) related to the West African Monsoon controls the basin's climate. The period of April to October represents the rainy season in the basin, with the annual rainfall varying between 1,100mm and 1,400mm (Klassou and Komi 2021). In Togo, the Oti River basin covers several economic regions (the western part of Central, Plateaux, and the whole Kara and Savannah regions). It is known to play a vital role in the country’s economy through its contributions to the overall GDP (37.7% of the national GDP in 2006) (Yomo et al., 2019).

The GRB covers Guinea (Conakry) and Senegal with a total surface area of 8,262km2 at the gauging station of Mako (Bodian et al., 2018). It experiences a Sahelian climate, characterised by a long dry season (November to May) and a short-wet season

(June to October). Average temperatures in Gambia range from 18°C to 30°C during the dry season and 23°C to 33°C during the wet season. The mean annual rainfall is 1,208mm in the basin at the gauging station of Mako (Bodian et al., 2018). In terms of economic significance and preoccupation of local populations, it is impossible to overestimate the role of agriculture (broadly defined) in the development of the basin. Agriculture is the backbone of the GRB economy (Cheikh, 2018) and the primary source of most individual or regional income, directly or indirectly. About 85% of the population earns its livelihood from crop farming, animal husbandry, or related rural activities; more than 2/3 of the region's gross domestic product is also derived from these activities.

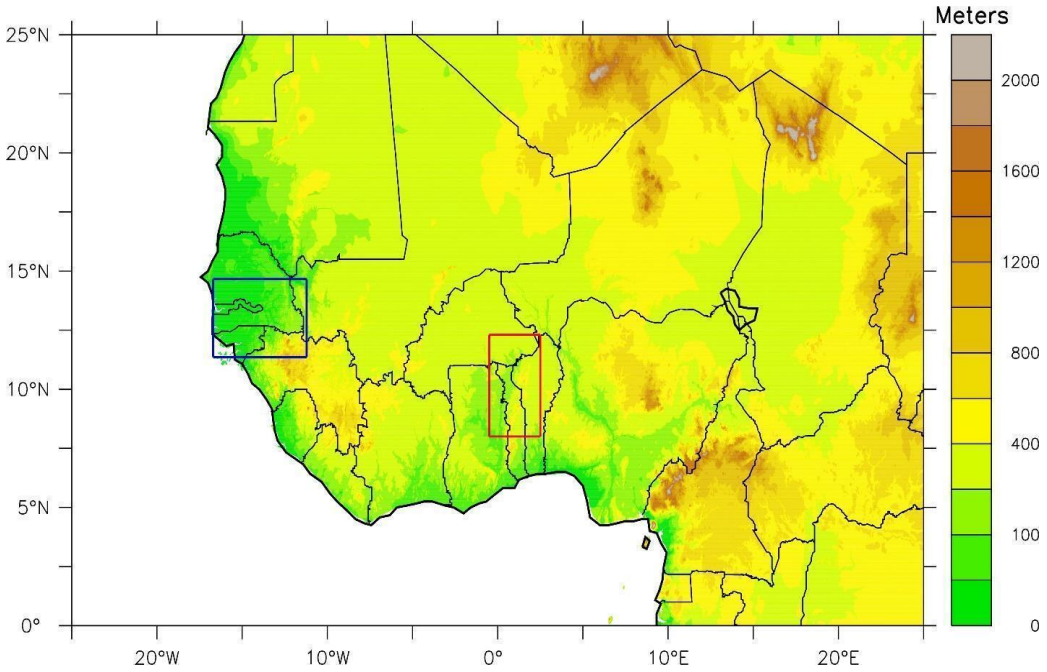

Figure 3.1: Study area showing its topography in meters. The red box (Oti basin) and the blue box (Gambia basin) are the areas over which the study investigates the rainfall intensity versus frequency and the widespread extreme rainfall events (WERE

3.1.2 Study area for hydraulic simulation

The study was conducted in Mango City, in northern Togo, along the Oti River, focusing on two selected areas (Figure 3.2). Within the Oti River basin, a sub-basin of the Volta basin in West Africa, the study area is located in the Savanna climate zone. Its climate is controlled by the Inter-Tropical Discontinuity (ITD) movement, which is related to the West African Monsoon. As a result, the area experiences a single wet season from April to October (Batebana et al., 2015), with the annual rainfall varying between 1,100mm and 1,400mm (Klassou & Komi, 2021).

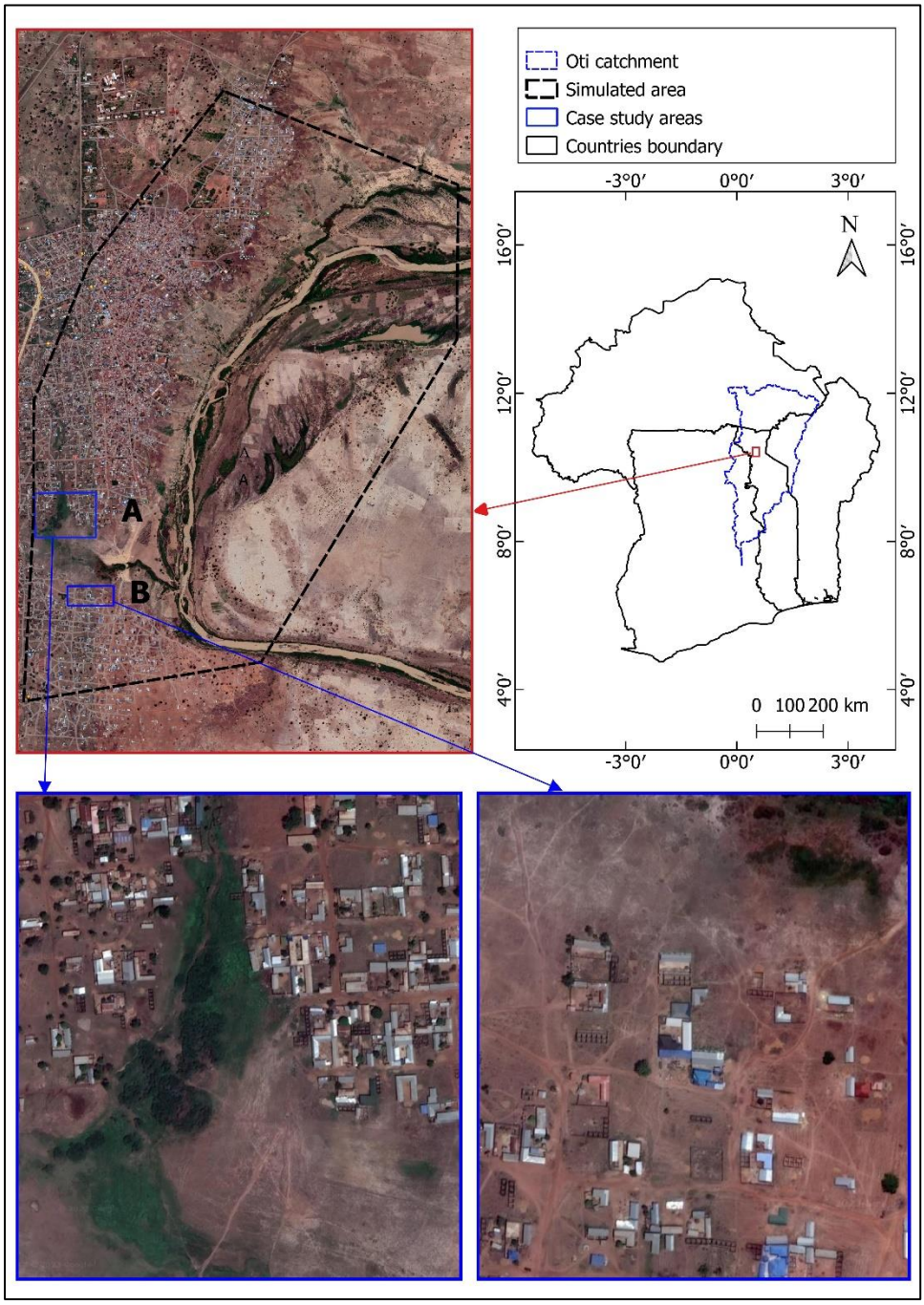

Figure 3.2: Study area showing the HEC-RAS simulation area and the two small areas named A and B used to examine the composite fluvial and pluvial floods

3.2 DATASETS

First, this study analysed observation, reanalysis, and climate model simulation datasets. Four observation datasets, which are from four different sources (Table 3.1), were used to evaluate the model simulation. The reanalysis datasets that were used come from the European Center for Medium-Range Weather Forecasts (ECMWF) reanalysis v5 (ERA5) and the Climate Forecast System Reanalysis (CFSR); the details of these reanalysis datasets are also given in Table 3.1. The climate model data is from the Model for Prediction Across Scale simulation (details in the method section). The main climate variables used were daily rainfall, specific humidity, air temperature, geopotential height, zonal and meridional wind and Convective Available Potential Energy (CAPE).

Secondly, river discharge datasets recorded at daily timescales from 2015-2020 along the Oti River in Mango were used in this study for the hydraulic modeling. The datasets were obtained from the National Hydrological Service of Togo. Also, digital elevation model (DEM) data derived from the Sentinel 2 imagery at 10 m resolution was used for the HEC-RAS model geometry configuration. The Land-Use was also the important dataset used in this study. It was obtained from Sentinel 2 Lan Use database. The Land Use data was used to assign Manning's values which were then associated with the model geometry.

Table 3.1: Information on the four observations and two reanalysis datasets used in the study. The period 1981–2010 was analysed for all the datasets in the study

Dataset	Full name	Type	Resolution	References
AgMERRA	Climate forcing datasets for agricultural modelling	Reanalysis-based multiple-source	0.25°	Rienecker et al. (2011)
AgCFSR	Climate forcing dataset for agricultural modeling	Reanalysis-based multiple-source	0.25°	Rienecker et al. (2011)
CHIRPS	Climate hazard group infrared precipitation with stations	Satellite and ground-based data	0.05°	Funk et al. (2015)
WFDEI-CRU	Water and global change forcing data methodology applied to ERA-interim (Climate Research Unit)	Reanalysis-based multiple-source	0.5°	Weedon et al. (2014)
ERA5	European Centre for Medium-Range Weather Forecasts Reanalysis 5	Reanalysis dataset	0.25°	Hersbach et al. (2020)
CFSR	Climate Forecast System Reanalysis	Reanalysis dataset	0.5°	

3.3 METHODS

3.3.1 Performance of the MPAS Global Climate Model

3.3.1.1 Characterising extreme and widespread extreme rainfall events

The extreme rainfall events over West Africa were characterised using eight rainfall indices (Table 3.2). Following the definition of the Expert Team on Climate Change Detection and Indices (Tank et al., 2009), the indices were calculated at each grid point over the study area. At each grid point, the threshold for an extreme rainfall event was defined as the 95^{th} percentile of the daily rainfall over the grid point. Accordingly, any daily rainfall equal to or greater than this threshold was considered an extreme rainfall event. A widespread extreme rainfall event (WERE) was said to occur over any of the two basins if there was a simultaneous occurrence of extreme rainfall events over at least 70% of the basin (Figure 3.3). To evaluate the performance of the MPAS model in reproducing extreme rainfall over Western Africa, we compared the simulated indices for the period 1981–2010 (long run) with the mean of the indices from the four observation datasets. To provide context for the model bias, the biases of the model were compared to the uncertainties of the observations. The model performance was also quantified with spatial correlation coefficient (r) between the simulated and the observed rainfall indices.

Table 3.2: Description of rainfall indices used in the study

Rainfall indices	**Description**
WDAYS	Wet days. Annual count of days with daily rainfall greater or equal to 1mm (Tank et al., 2009).
Rx5day	Maximum consecutive 5-day rainfall.
R20mm	Annual count of days when daily rainfall ≥20mm (Tank et al., 2009).
CWD	The maximum number of consecutive wet days (Tank et al., 2009).
RTOT	Annual total rainfall on wet days (Tank et al., 2009).
SDII	SDII is the intensity of normal rainfall, calculated as RTOT divided by WDAYS (Tank et al., 2009).
R97.5p	All-day percentile. The R97.5th percentile rainfall on all days. (Schär et al., 2016). Any daily rainfall above this threshold (R97.5p) is considered an extreme event.
R97.5pTOT	Annual total rainfall when daily rainfall is greater than or equal to R97.5p (Schär et al., 2016).

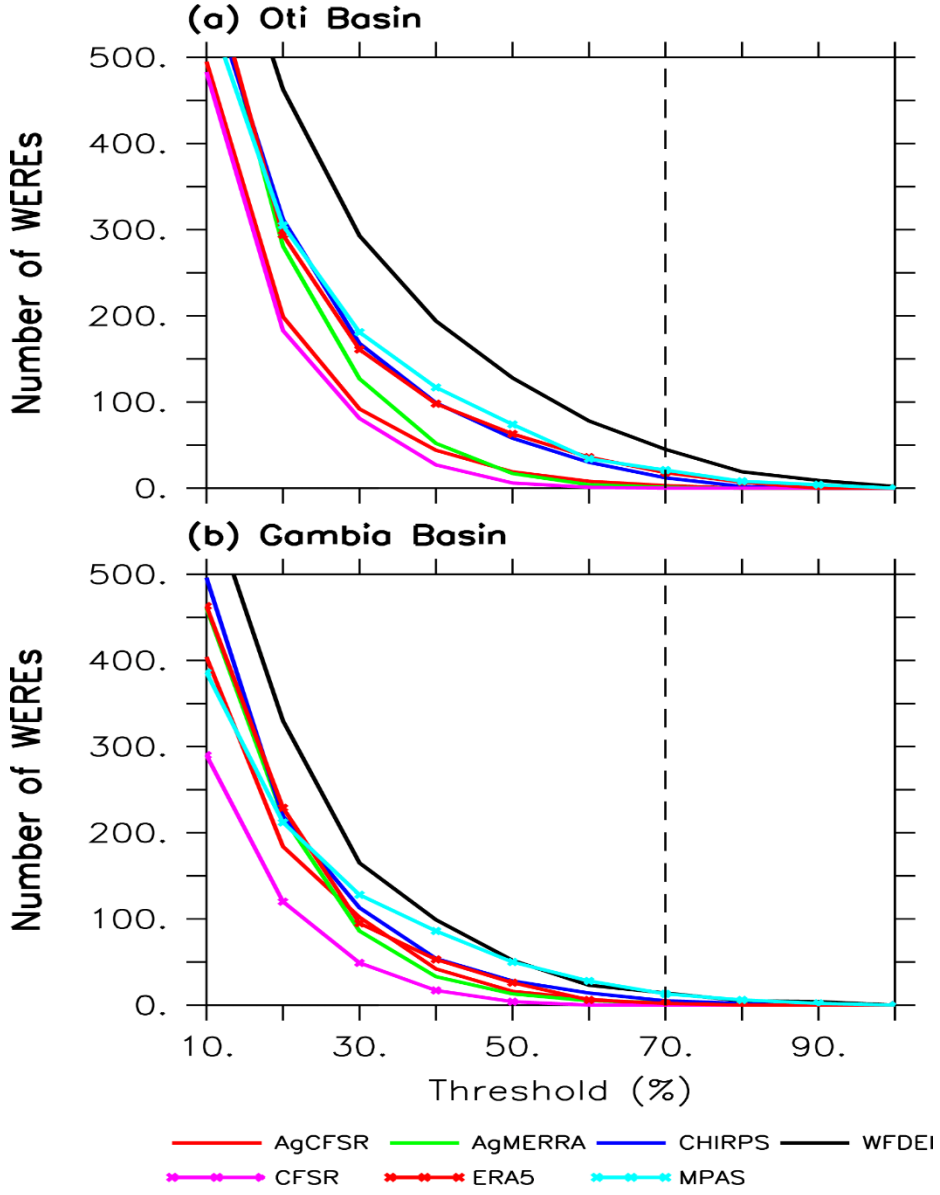

Figure 3.3: Variation in the number of WEREs (over the Oti and the Gambia river basins) with the WERE threshold criteria. The threshold criteria refer to the minimum percentage area of basins that simultaneously experience an extreme event as depicted by observation

3.3.1.2 MPAS model evaluation method for the long run simulation

Different evaluation metrics are available to evaluate the performance of a model. Nevertheless, no single metric can capture all relevant aspects. Therefore, it is crucial to consider different metrics and comprehend the kind of insights they can offer. In this research, though two metrics (correlation and systematic errors) of the model outputs are calculated to evaluate the model's performance, other metrics are also described. These metrics assess the correlation strength, systematic errors, and accuracy of the model compared to observations and are described below.

One of the statistics used is correlation coefficient (r), a measure of the strength of the linear relationship between model and observations.

$$r = \frac{1}{(n-1)} \sum_{i=1}^{n} \left(\frac{M_i - \overline{M}}{\sigma M}\right)\left(\frac{O_i - \overline{O}}{\sigma O}\right) \quad \textbf{Equation 3.1}$$

where *O* represents Observation or Reanalysis, *M* model output, σ standard deviation, and n number of data points in the series.

The Mean Bias (B) is another statistic that indicates the mean over or underestimate of predictions. It has the same units as the quantities being considered.

$$B = \frac{1}{n} \sum_{i=1}^{n} (M_i - O_i) \quad \textbf{Equation 3.2}$$

Lastly, the Mean Absolute Error (MAE) statistics that determine the mean error between model and observation regardless of whether it is an over or underestimate. It also has the same units as the quantities being considered;

$$MAE = \frac{1}{n} \sum_{i=1}^{n} |M_i - O_i| \quad \textbf{Equation 3.3}$$

3.3.1.3 Case study: extreme rainfall events over the Oti River basin

The sensitivity of MPAS in simulating two selected extreme rainfall events over the Oti River basin were assessed. The selection of the events was based on their devastating and destructive impacts on society. For example, the rainy season of 2007 caused widespread flooding from extreme rainfall events that affected 792,676 people in West Africa and caused 210 deaths (Samimi et al., 2012; OCHA, 2007). Togo was among the countries that was most affected, especially the city of Mango in the Oti River basin, with 127,880 people and 23 deaths. On 1 July 2007, Mango city experienced one of these heavy rainfall-induced flood events along the Oti River, with 77.7mm of rain recorded at the local weather station. Ten years later, on 22 July 2017, the same region in the Oti River basin experienced heavy rainfall along the Oti River in Mango, where rainfall of 109.5 mm was recorded at Mango's weather station.

3.3.1.4 MPAS Model description and experimental set-up

The current study used the atmospheric core of the MPAS model, developed by the National Center for Atmospheric Research (Skamarock et al., 2010; Donkin and Abiodun, 2022; Zhao et al., 2019). The fully compressible non-hydrostatic equations of motion solved in the MPAS atmosphere dynamical core is described in Skamarock et al. (2012). MPAS uses Voronoi tessellations to create irregular multigonal grid cells around grid points to create a global irregular grid (Kramer et al., 2020; Skamarock et al., 2012). As a result, it allows smooth transitions from coarse to fine resolution, in contrast to the nesting techniques of traditional regional models. MPAS thus overcomes issues commonly associated with local refinement, where the transitions are often abrupt (Donkin and Abiodun, 2022; Duda et al., 2019). In addition, MPAS model has the capability of selecting individual parameterization schemes for various physical

processes in the atmosphere (e.g., convection, microphysics, etc.) as well as the capacity to select a suite of parameterization schemes (mesoscale reference or convection-permitting) to facilitate and ensure a choice of compatible schemes (Duda et al., 2019). This study used the mesoscale reference suite, and its corresponding parameterization schemes are summarised in Table 3.3.

MPAS was used to perform five experiments (Table 3.4). The goal of the first experiment was to assess how well the model reproduces the characteristics of West African extreme rainfall events over a long period, while the goal of the other experiments was to investigate the sensitivity of the simulated extreme event to the model boundary condition and local enhancement in the horizontal grid resolution over a short period. The first experiment consisted of only one simulation called MPAS_Clim, in which the model was applied at 60km uniform-grid resolution (Figure 3.3a) to produce 30 years and 1 month of climate data. The simulation was initialised with CFSR reanalysis data (on 1 December 1980 at 00h00 UTC) and forced with observed sea surface temperature data from the CFSR reanalysis dataset. However, only the data of the last 30 years of simulation was analysed in this study, as the data of the first month was discarded as model spin-up.

The second experiment was similar to the first experiment, except that it consisted of two simulations (called MPAS60_CFSR and MPAS60_ERA5) and the simulations only covered 7 days. While the MPAS60_CFSR simulation was initialised with CFSR, MPAS60_ERA5 was initialised with ERA5. The remaining three experiments were similar to the second experiment except that the simulations in these experiments used variable-resolution grid mesh with higher resolution (i.e., 15km, 10km, and 3km, respectively) over West Africa and 60km resolution outside the domain

(Figure 3.3b-c-d). Across all the experiments, the MPAS simulation used 41 vertical levels up to about 44km height.

Table 3.3: Parameterization schemes included in the default MPAS physics suites used in this study

Parameterization	**Mesoscale reference**
Microphysics	WSM-6
Convection	New Tiedtke
PBL	YSU
GWDO	YSU GWDO
Longwave radiation	RRTMG
Shortwave radiation	RRTMG
Cloud	Fraction
Surface layer	Monin Obukhov
Land surface model	Noah

Table 3.4: MPAS experiments performed in the study. The indicated simulation periods exclude the simulation spin up-time

Experiments	**Simulation**	**Horizontal resolution**	**Initial condition**	**Duration**
1	MPAS_Clim	60 km uniform	CFSR	30 years
2	MPAS60_CFSR	60 km uniform	CFSR	7 days
	MPAS60_ERA5	60 km uniform	ERA5	
3	MPAS15_CFSR	60-15 km variable	CFSR	7 days
	MPAS15_ERA5	60-15 km variable	ERA5	
4	MPAS10_CFSR	60-10 km variable	CFSR	7 days
	MPAS10_ERA5	60-10 km variable	ERA5	
5	MPAS03_CFSR	60-03 km variable	CFSR	7 days
	MPAS03_ERA5	60-03 km variable	ERA5	

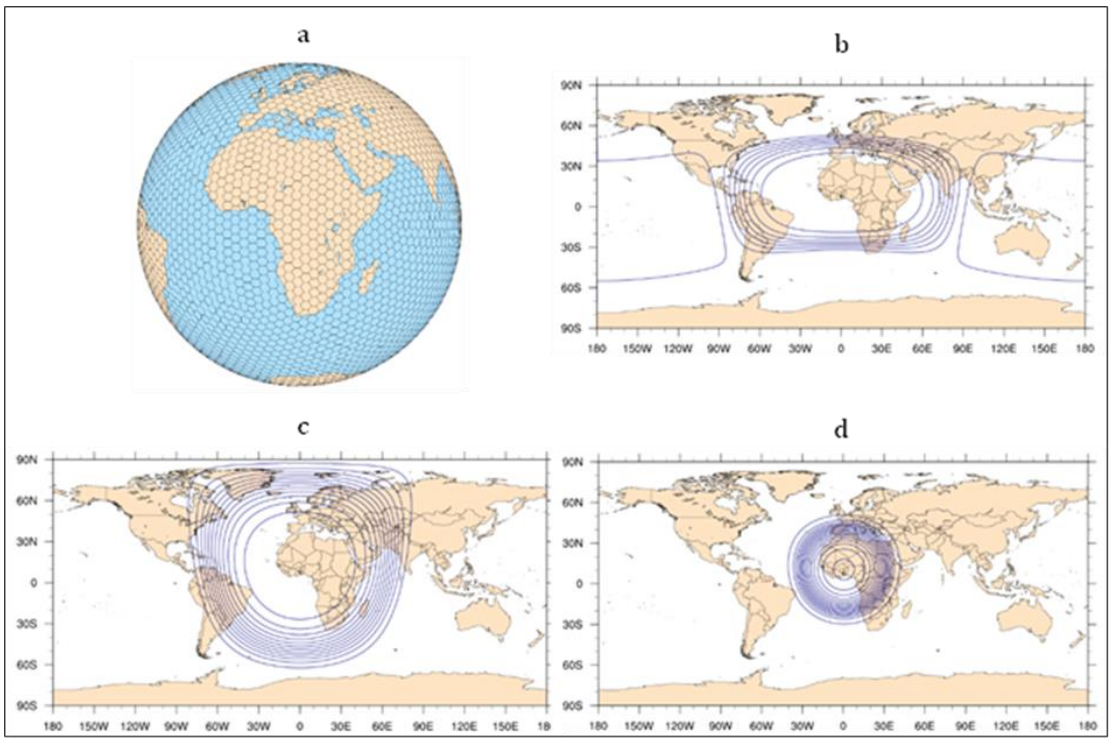

Figure 3.4: MPAS mesh resolution used in the simulations: (a) 60km uniform resolution for the long run (30 years simulation) and for the sensitivity simulations to initial condition dataset; b-c-d show the MPAS domain used in the resolution sensitivity simulation

3.3.2 Performance of HEC-RAS Hydraulic Model

3.3.2.1 Evaluation and application of the HEC-RAS model in simulating actual and hypothetic flood events

Flooding is a prevalent disaster that can result in significant economic and property loss, as well as loss of human life. While it may not be possible to prevent such events, advancements in hydraulic modeling allow us to identify flood-prone areas, potential inundation depth, and extent, which can then be used to create flood risk maps for specific locations. These risk maps can help identify critical zones, disseminate early warnings to residents during a potential flood, and assist in making emergency decisions.

In this study, we first evaluated the performance of HEC-RAS 2D model version 6.1, in simulating the actual flood event, in terms of flood extent in Mango on 17 October along the Oti River. Indeed, in October 2020, Togo was severely affected by the flooding of the Oti River and its tributaries. Almost 57,000 people were affected, with 11 fatalities (ECHO, 2020; Copernicus-EMSR470: Flood in Togo). In that regard, Togo authorities needed the situation of flood extent, especially in Mango, to assess the impacts on settlements, agricultural systems, and infrastructure damages. Unfortunately, though the event started on 5 October 2020, the flood extent was made available for the 17 October situation by the Copernicus Emergency Management Service (EMS) after the Togolese authorities activated the case on 13 October. The flood situation on 17 October 2020 is shown in Figure 3.5 (source: Copernicus), and table 3.5 shows the event's consequences within the area of interest.

Secondly, we simulated fourteen hypothetical hydrographs scenarios (Figure 3.6) to assess the effect of the maximum flow over the selected areas named A and B, shown in Figure 3.2. In addition to the hypothetical hydrograph, rainfall scenarios were

designed to evaluate the effects of the combined fluvial and pluvial floods over areas A and B. Both fluvial and combined fluvial and pluvial were then compared.

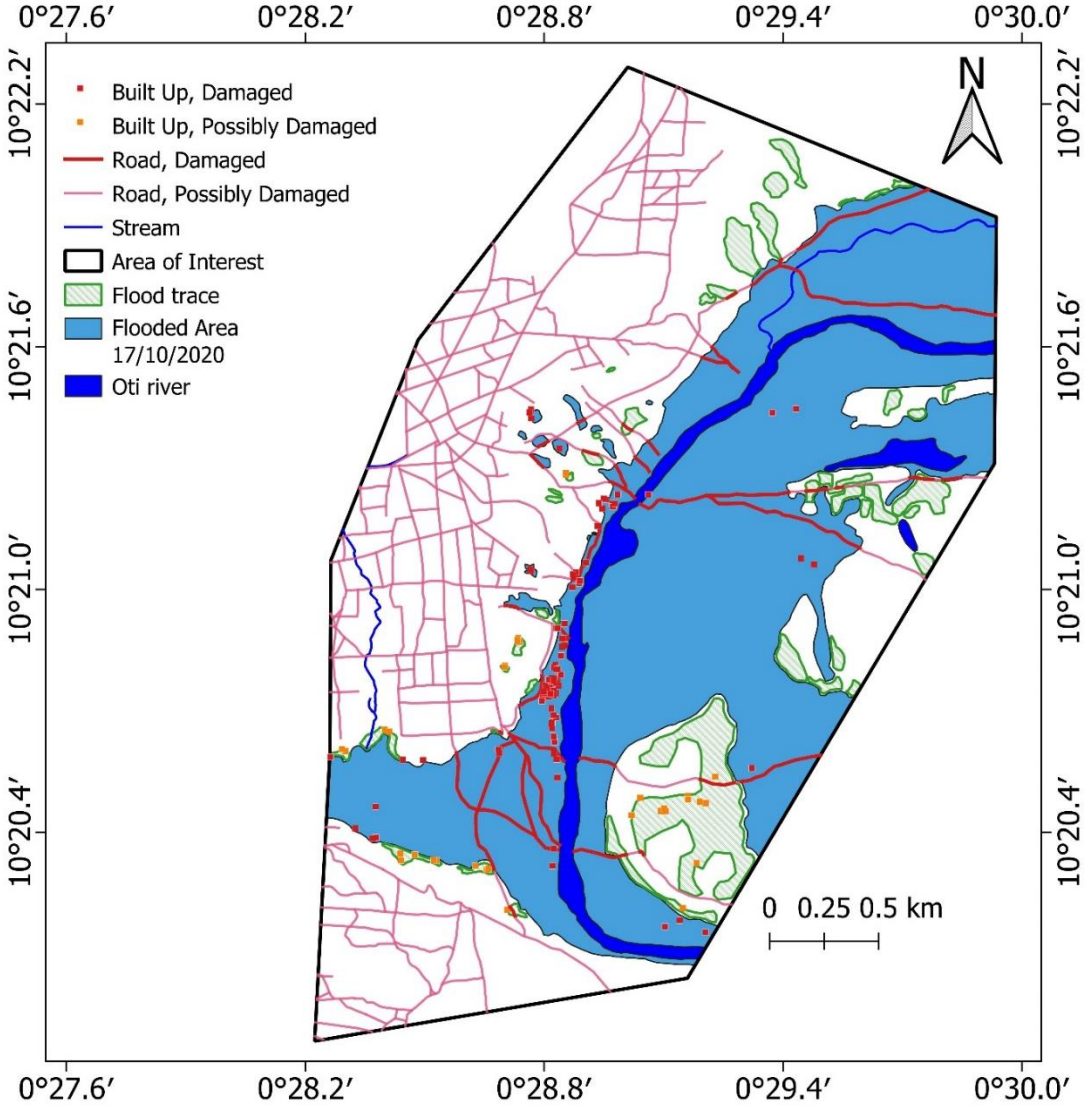

Figure 3.5: Situation of observed flood event on 17 October 2020 in Mango city showing its various impacts (Source: Copernicus EMSR470)

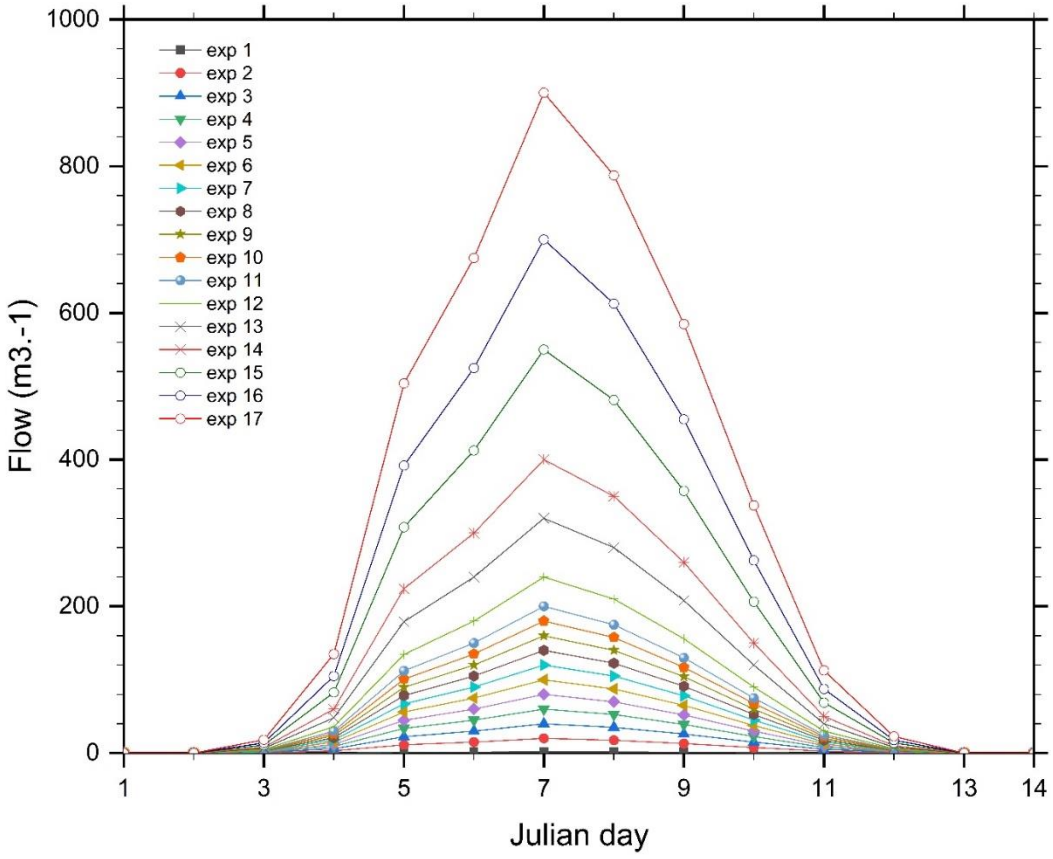

Figure 3.6: The fourteen hypothetical hydrographs scenarios to investigate the impacts of the maximum flow as well as the effects of the combined fluvial and pluvial flood over areas A and B.

Table 3.5: Summary of the flood impacts in Mango in October 2020 (Source: Copernicus-EMSR470)

Consequences within the Area Of Interest (AOI)							
	Unit of measurement		Destroyed	Damaged	Possibly damaged	Total affected	Total in AOI
Flooded area	ha					363.3	
Flood trace	ha					47.6	
Estimated population	Number of inhabitants					91243	
Settlements	Residential Buildings	No.	0	83	37	120	120
Transportation	Local Road	km	0.0	7.4	0.5	8.0	50.4
	Cart Track	km	0.0	1.1	0.1	1.1	4.6

3.3.2.2 HEC-RAS model description and Experiment

The HEC-RAS 2D model, version 6.1, provides three equation sets that can be utilized to compute the flow of water over the computational mesh. These include the Diffusion Wave equations (DWE; Equation 3.4) and the Shallow Water equations (SWE; Equation 3.5), which employ either the Eulerian-Lagrangian method or the Eulerian method, which is more momentum conservative.

$$\begin{cases} g\frac{\partial H}{\partial x} + C_f u = 0 \\ g\frac{\partial H}{\partial y} + C_f v = 0 \end{cases} \quad \textbf{Equation 3.4}$$

$$\begin{cases} \frac{Du}{Dt} - fv = -g\frac{\partial H}{\partial x} + v_t\nabla_u^2 - C_f u + \frac{\tau_{sx}}{\rho h} \\ \frac{Dv}{Dt} + fu = -g\frac{\partial H}{\partial y} + v_t\nabla_v^2 - C_f v + \frac{\tau_{sy}}{\rho h} \end{cases} \quad \textbf{Equation 3.5}$$

The time step of the model is determined based on the Courant-Friedrichs-Lewy condition in order to maintain numerical stability (Equation 3.6).

$$\mathrm{C} = \frac{V\Delta T}{\Delta x} \leq 1.0 \quad (with\ \mathrm{C}_{max} = 3.0) \quad \textbf{Equation 3.6}$$

where C is the Courant number, V is the velocity (m s^{-1}), ΔT is the time step (s), and Δx is the grid cell size (m).

The model geometry was built in Ras Mapper and HEC-RAS editor using the DEM (Figure 3.5b) to represent the ground surface. In addition, Manning's values associated with each zone were defined according to land use and land cover classes (Figure3.5a). Ras Mapper was used to build a computational mesh at 10 m spatial resolution on the entire study area—the final mesh contained over 138000 cells comprising three to eight faces. While one external boundary condition was set to flow hydrograph upstream of the Oti River, the second external boundary condition was set

to normal depth. Also, the friction slope was estimated near the outlet of the simulation domain. The model was run between 01 September 2020 00:00 and 31 September 2020 00:00 with a computational interval of 5 s using HEC-RAS version 6.1, set up on Windows 11 (64-bits), and run on High-Performance Computing environment (HPC). The Model outputs interval was set to 1 day for model performance. A diffusion Wave Equation was used in this simulation, and all other HEC-RAS unsteady computation options and tolerances were set to default.

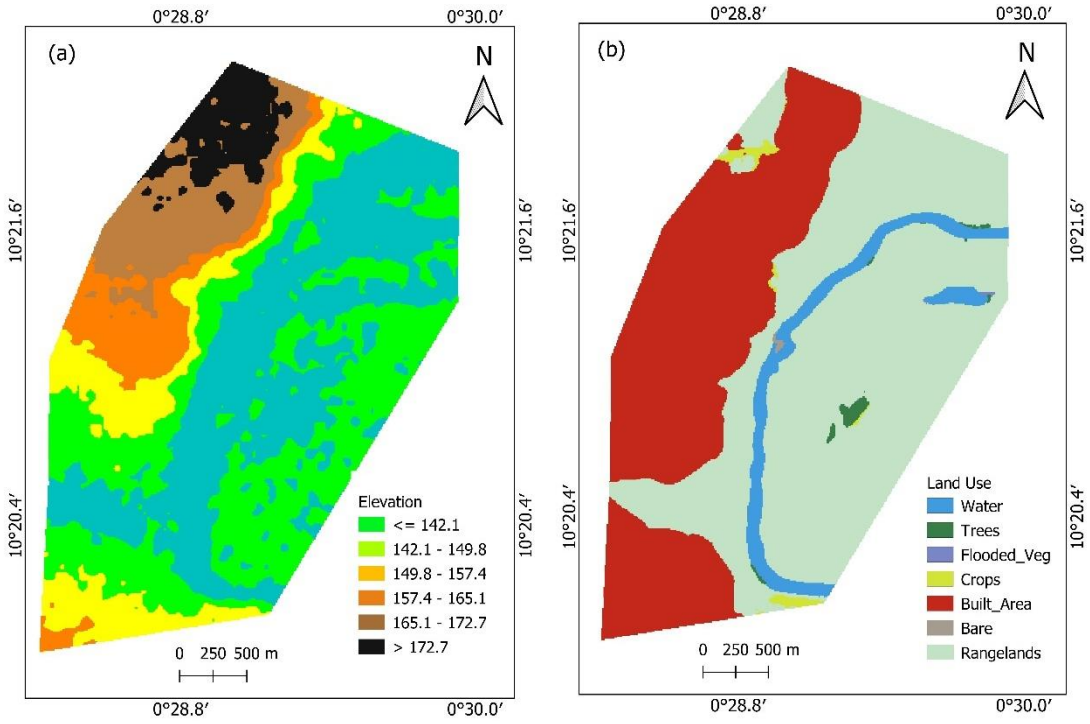

Figure 3.7. The Digital Elevation Model (a) and the Land Use (b) used to set up the model geometry and the associated Manning's values for HEC-RAS simulations.

CHAPTER FOUR

4.0 RESULTS AND DISCUSSIONS

4.1 SIMULATION OF EXTREME RAINFALL USING MPAS MODEL

4.1.1 Performance of MPAS model

This section assesses the performance of the MPAS model in simulating the characteristics of extreme rainfall over West Africa. The study uses four observation datasets (AgCFSR, AgMERRA, CHIRPS and WFDEI-CRU) to evaluate the model simulation. To put the model performance in the proper perspective, the study first discusses the uncertainties in these observed datasets, then compares the model biases with the uncertainties. In addition, two reanalysis datasets are used to serve as an interface between the MPAS model data and the observation datasets.

4.1.1.1 Spatial pattern of rainfall indices over West Africa

Figures 4.1 and 4.2 show notable uncertainties in observed datasets for all rainfall indices, as indicated by the standard deviation (STD) among the observations. For most indices (e.g., R20mm, R97.5p, R97.5pTOT, CWD, RTOT), the uncertainty level increases with the magnitude of the rainfall indices. For example, in the R20mm, the highest uncertainties (STD $\geq$ 40 days year^{-1}) occur over the mountain regions where the highest R20mm are observed ($\geq$ 72 days year^{-1}) and the lowest uncertainties (STD $\leq$ 5 days year^{-1}) occur over the areas above the latitude 15°N where the lowest R20mm are observed ($\leq$ 24 days year^{-1}). This high level of uncertainty over the mountain regions may be due to the low resolution of some observed rainfall datasets. Several studies have reported similar uncertainties in the observed rainfall datasets over Africa in general (e.g., Klutse et al., 2021; Abiodun et al., 2019; Sylla et al., 2015). They also

attributed the uncertainty to the differences in the resolutions of datasets. However, lowering the uncertainty in the observation dataset over Africa is essential for model development and evaluation.

The MPAS simulation gives credible representations of the spatial patterns of rainfall indices over Western Africa (Figures 4.1 and 4.2, fourth column). For most indices (e.g., R97.5p, R97.5PTOT, RTOT, WDAYS, CWD and Rx5day), MPAS reproduces the observed spatial patterns with a high correlation ($r > 0.8$). However, the model overestimates some indices (e.g., WDAYS and CWD) over the Guinea highlands and along the Guinea coast and Cameroon Mountain (Figure 4.3), and underestimates others (e.g., RTOT, SDII, R97.5p, R97.5PTOT, Rx5day, R20mm, and Rx5day) almost over the entire region (Figures 4.3 and 4.4). Even though the model overestimates WDAYS (by more than 18 days) and CWD (by more than 20 days) over these regions (Figure 4.3h-p), the model biases of both indices are still within the observation uncertainties (±30 days). Although MPAS overestimates the WDAYS, it underestimates the RTOT (by 500mm year-1, Figure 4.3d), possibly because the model underestimates the SDII (by more than 3.6mm day-1, Figure 4.3l) over these regions. Moreover, the MPAS simulation underestimates the indices related to extreme rainfall (R97.5p, R97.5pTOT, and R20mm) (Figure 4.4d-h) over West Africa, suggesting that the physics suite used in the simulation may underestimate the convective available potential energy or the moisture convergence flux over the region. This underestimation could also be because the CFSR data used to initialise the model underestimates the R97.5p and overestimates the R97.5pTOT, with biases out of the observation uncertainty (Figure 4.4c-g). Several other studies show a similar bias over West Africa (Faye and Akinsanola, 2022; Klutse et al., 2021). For example, Faye and Akinsanola (2022) found that most GCMs from the CMIP6 (EC-Earth3 HadGEM3-GC31-LL, UKESM1-LL,

MRI-ESM2-0 and EC-Earth3-Veg) also underestimate Rx5day and R95pTOT over the entire region of West Africa. Klutse et al. (2021) also reported an overestimation of CWD over the Guinea highlands and along the Guinea coast and Cameroon Mountain in most CMIP6 global models.

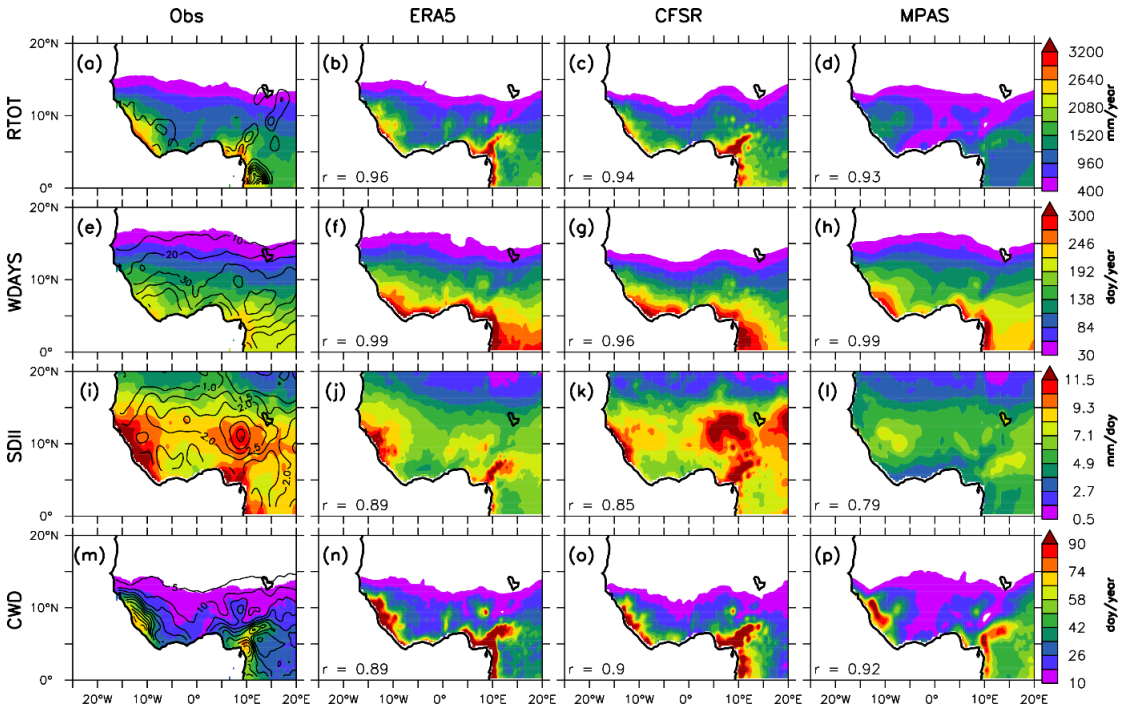

Figure 4.1: The spatial pattern of rainfall indices (RTOT, WDAYS, SDII, and CWD) over western Africa. The first column is for the mean of observation datasets (AgCFSR, AgMERRA, CHIRPS, WFDEI-CRU), the second for ERA5, the third for CFSR data, and the fourth column for the MPAS model. In the first column, the contours represent the standard deviation among the observation data; r indicates the spatial correlation between the datasets and the observed mean.

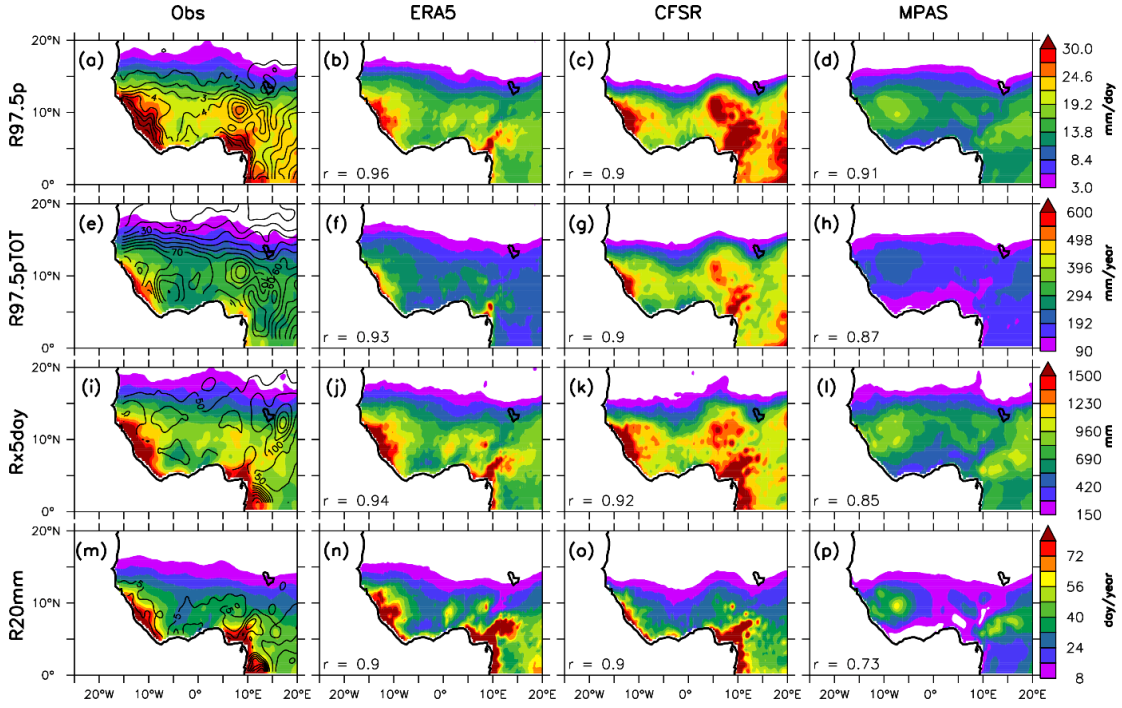

Figure 4.2: Spatial pattern of rainfall indices (R97.5p, R97.5pTOT, Rx5day, and R20mm) over western Africa. The first column is for the mean of the observation datasets (AgCFSR, AgMERRA, CHIRPS, WFDEI-CRU), the second for ERA5, the third for CFSR data, and the fourth column for the MPAS model. In the first column, the contours represent the standard deviation among the observation data; r indicates the spatial correlation between the datasets and the observed mean.

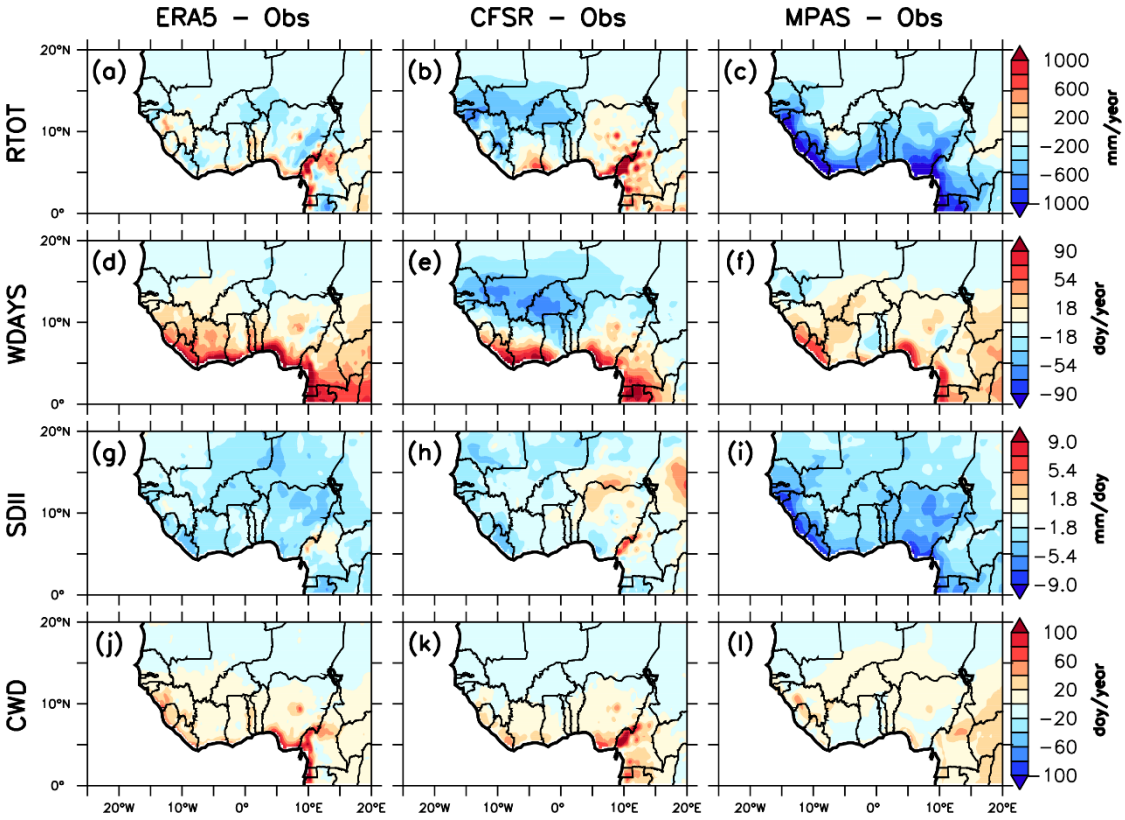

Figure 4.3: The spatial pattern of biases in rainfall indices (RTOT, WDAYS, SDII, and CWD) over western Africa as shown in ERA5, CFSR, and MPAS model datasets to the observation mean.

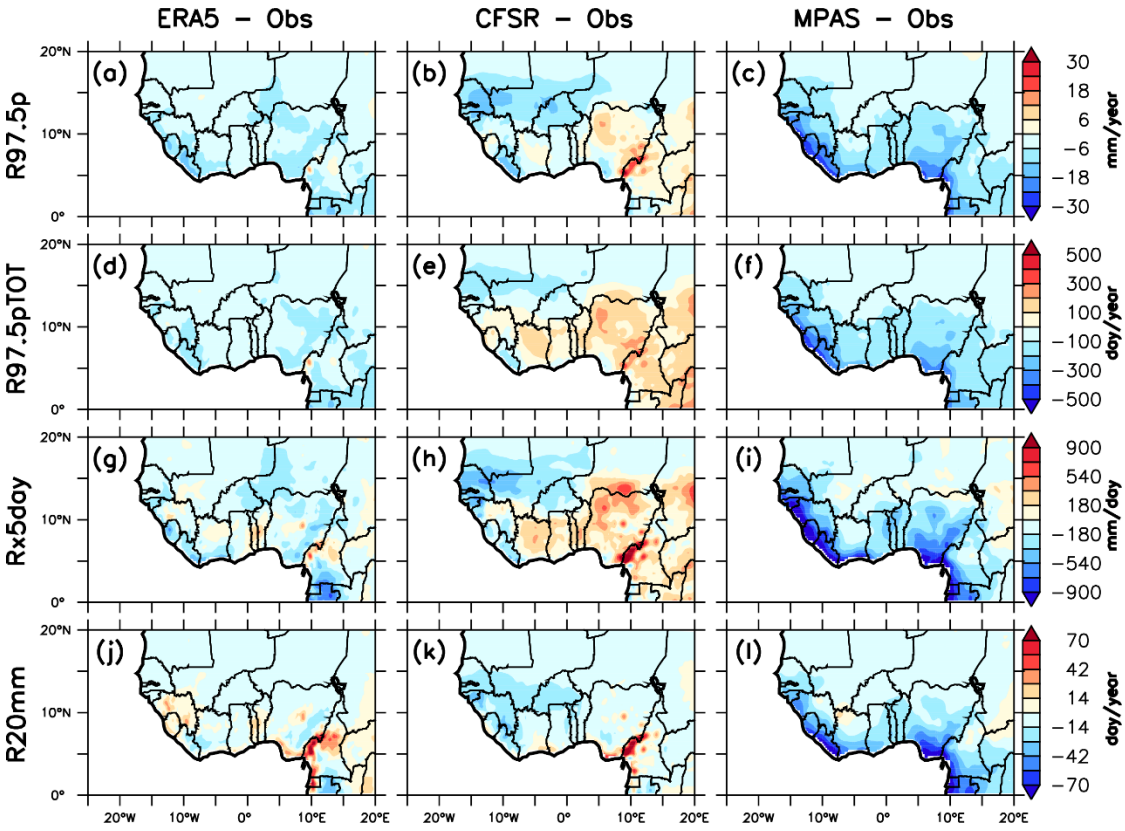

Figure 4.4: The spatial pattern of biases in rainfall indices (R97.5p, R97.5TOT, Rx5day, and R20mm) over western Africa as shown in ERA5, CFSR, and MPAS model datasets to the observation mean.

4.1.1.2 Rainfall characteristics over the selected basins in West Africa

Figure 4.5c-d shows that MPAS captures the rainfall intensity-frequency curves (rainfall frequency decreases with an increase in intensity) over the two river basins. However, MPAS also shows substantial discrepancy when compared to observation datasets (Figure 4.5a-b). For instance, in both basins, the curve of the MPAS simulation is out of the range of the observation spread. It lies at the lower end of the observed spread (Figure 4.5c-d), meaning that the model underestimates the frequency of heavy rainfall over these areas. While MPAS reports the highest intensity of rain to be 50mm day^{-1} over the Oti basin, it is about 100mm day^{-1} over the Gambia basin. Over the Oti basin, the curve of reanalysis data (CFSR) falls within the observed spread until the rainfall intensity reaches 80mm day^{-1}, after which it lies at the upper end of the spread. The highest intensity rainfall of CFSR and ERA5 datasets reaches 150mm day^{-1} and 120mm day^{-1}, respectively, whereas the one of MPAS reaches only 50mm day^{-1}. Again, CSFR and ERA5 exhibit the highest intense rainfall over the Gambia basin, with 180mm day^{-1} and 160mm day^{-1}, respectively, compared to MPAS simulation with 100mm day^{-1}. Overall, the performance of MPAS in simulating the rainfall intensity-frequency is similar to those of CMIP6 reported by Klutse et al. (2021). Klutse et al. (2021) showed that some CMIP6 models (MIROC6 and GFDL-ESM4) underestimate the frequency of heavy rainfall over West Africa. Furthermore, Crétat et al. (2014) argued that the limited skill of most GCMs in simulating the frequency of intense rainfall is because of the too frequent triggering of convection independent of their horizontal resolution.

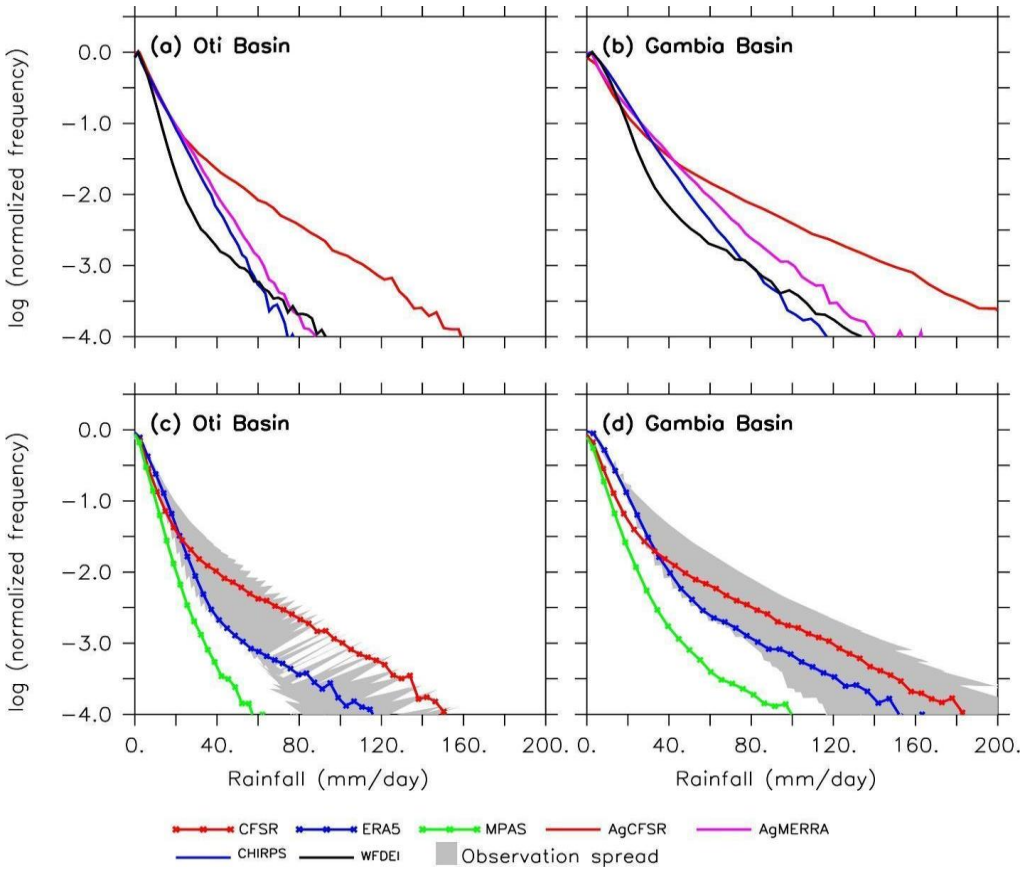

Figure 4.5: The rainfall intensity–frequency curves over Oti and Gambia basins in West Africa as depicted by observation datasets (first row), MPAS model, and reanalysis datasets (ERA5, CFSR) in the second row. The grey area shows the observation spread.

4.1.1.3 Temporal variation of widespread extreme rainfall events in JJAS season

Figure 4.6 presents the monthly variation of widespread extreme rainfall events (WEREs) over the Oti River and the Gambia River basins during the June to September wet season (JJAS). It shows that MPAS simulates the highest number of WEREs in September. While the MPAS model reports 33 WEREs in September (the highest), the observed mean reports its highest number of WEREs in August (21 events). Notably, MPAS reports a higher number of WEREs in August (23 events) than the observed mean reports, even if MPAS does not report August to be the month featuring most WEREs overall, as stated above. While the MPAS model shows fewer WEREs compared to the observation mean in June and July over the basin, CFSR does not report any WEREs at all. On the other hand, MPAS shows a discrepancy in comparison with the peculiar observation datasets. In most months, WFDEI reports more WEREs over the basin. For example, in July and August, while WFDEI reports a more significant number of WEREs (40 in July and 55 in August) than MPAS (4 in July and 23 in August) over the Oti basins, AgCFSR and AgMERRA report fewer than the MPAS model, meaning that the model bias is within the observed spread. Meanwhile, the occurrence of WEREs can be attributed to several factors. For example, Roxy et al. (2017) showed that, in general, WEREs could result from nearly stationary and accumulating humidity levels over the region before the events. In addition, the south-westerly strengthening transport of moisture from the Atlantic Ocean towards the area could engender intensified precipitation over the subcontinent.

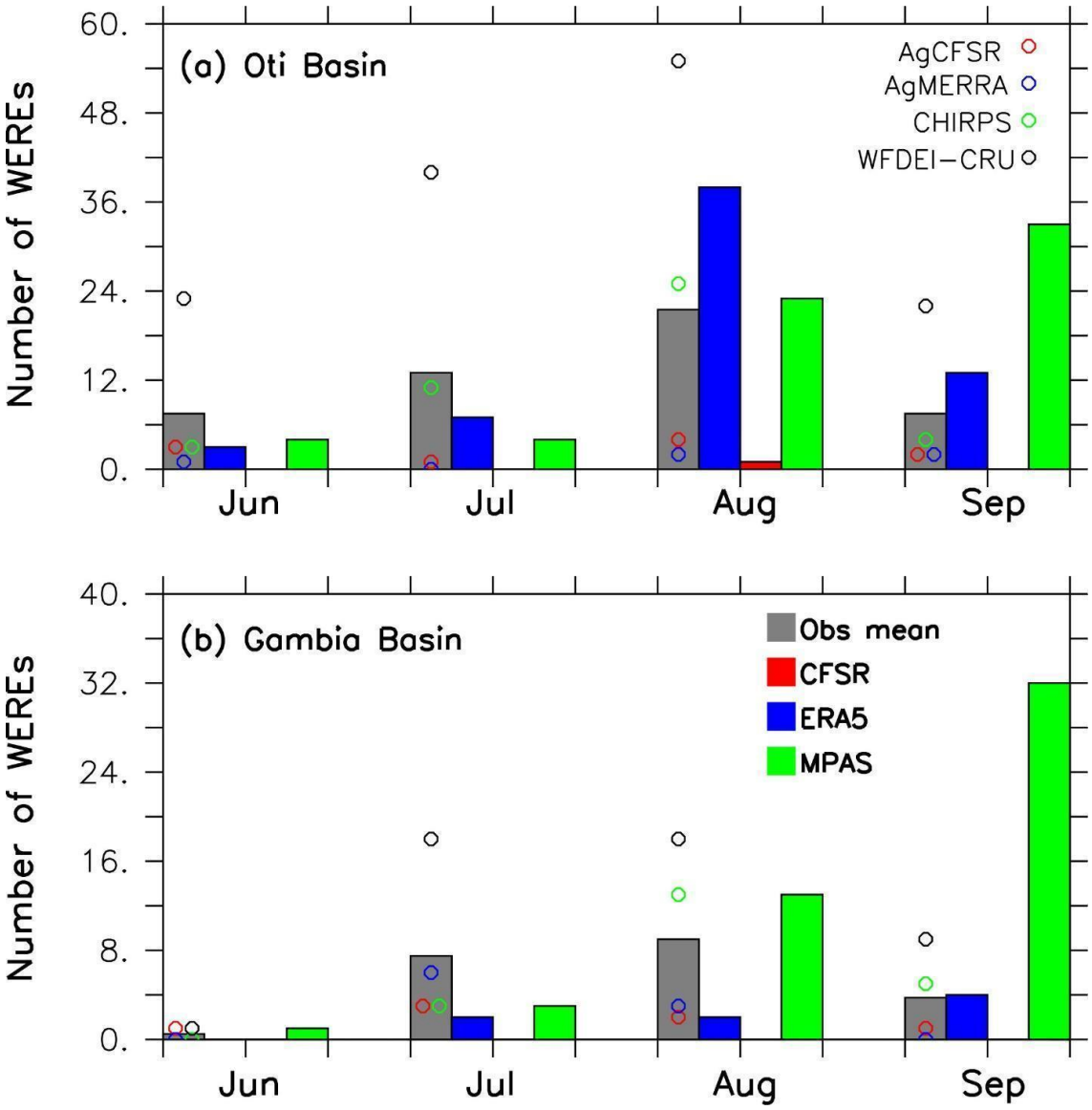

Figure 4.6: Monthly variation of widespread extreme rainfall events over Oti and the Gambia basins (1981–2010) as shown by observed datasets (AgMERA, AgCFSR, CHIRPS, and WFDEI-CRU), the mean observation datasets, the simulated (MPAS) and the reanalysis (ERA5 and CFSR) datasets.

4.1.2 Sensitivity of the simulated extreme rainfall events over Oti River basin

In this section, the sensitivity of MPAS to initial conditions is discussed, along with its model resolution in simulating two extreme rainfall events over the Oti River basin in Togo. These events occurred on 1 July 2007 (Case Study 1) and 22 July 2017 (Case Study 2).

4.1.2.1 Sensitivity to initial condition datasets

Figure 4.7 shows that regardless of the initial conditions, MPAS60 gives a credible representation of the three observed (CHIRPS, Figure 4.7a) rainfall regimes (over the Guinea highland, Oti River basin, and along Cameroon Mountain) in Case Study 1 (Figure 4.7a-e-f). However, it underestimates the spatial rainfall intensity over the Oti River basin, as shown in Figure 4.7d. While MPAS60_CFSR simulation shifts the peak of the temporal evolution of rainfall over the Oti River basin one day before the event, MPAS60_ERA5 simulates almost a constant rainfall before, during and after the event (Figure 4.7d). Why MPAS60_CFSR shifts this peak of rainfall a day earlier could be because the model triggers earlier convective activities. In addition, the two simulations (MPAS60_CFSR and MPAS60_ERA5) present the same pattern of moisture flux from the Atlantic Ocean, which diverges over the area. This could explain the underestimation of the rainfall peak and the spatial distribution of the rainfall intensity depicted in the model. Concerning the datasets used to initialise the model, the ERA5 data (Figure 4.7c) replicates the three rainfall regimes shown in the observation field (CHIRPS) and, more importantly, over the Oti River basin. In contrast, the CFSR data (Figure 4.7b) replicates only two rainfall regimes (over the Guinea highland and along Cameroon Mountain). As a consequence, the ERA5 data shows the peak of the temporal evolution of the rainfall over the Oti River basin as in the observation data

(Figure 4.7d). By contrast, the CFSR data shifts the peak to a day after the event. This could be explained by the convergence of the moisture flux at 850hPa from the ocean over the area in the case of the ERA5 dataset and its divergence in the case of CFSR (Figure 4.7b-c; vectors).

In Case Study 2, both MPAS60_CFSR and MPAS60_ERA5 simulations exhibit a similar rainfall pattern across West Africa (Figures 4.7k and 4.7l). For instance, regardless of the initial conditions, MPAS60 simulates the highest rainfall intensity over the Guinea highland, the northern part of Cote d'Ivoire, and the eastern part of West Africa. However, the simulations fail to replicate the rainfall intensity over the Oti River basin, as shown in the observation dataset (Figure 4.7g). This is consistent with the simulated temporal evolution of rainfall over the Oti River basin, where the model underestimates and shifts the peak as the observation data does (Figure 4.7j). The simulated moisture flux at 850hPa could explain this result (Figure 4.7k-l). The two simulations show a similar pattern of moisture flux over the area, where its sources are mainly from the continent. In addition, the moisture flux divergence over the Oti River basin cannot favour the upward motion during the event, producing less rainfall than the observed field. Again, in Case Study 2, CFSR and ERA5 datasets replicate the main rainfall regime shown in the observation field (CHIRPS; Figure 4.7g)—the only major difference is that the location of this rainfall pattern is shifted eastward in both CFRSR and ERA5 datasets (Figure 4.7h-i). By comparison, the CFSR dataset replicates the spatial pattern of the rainfall intensity over the Oti River basin and the peak of the temporal evolution of the rainfall better than the ERA5 (Figure 4.7j). Overall, using CFSR data as the initial condition, the model better represents the extreme rainfall event in Case Study 1. However, using ERA5 as the initial condition gives a better result in Case Study 2.

There needs to be more than moisture flux and its convergence to explain the performance of the MPAS model at 60km resolution in simulating the extreme rainfall events and how the reanalysis datasets (CFSR and ERA5) replicate the observed extreme rainfall events as discussed previously. Thus, for further context, Figure 4.8 (Case Study 1, 1 July 2007) and Figure 4.9 (Case Study 2, 22 July 2017) show the temporal evolution of the vertical profile of the Moist Static Energy (MSE), the specific humidity, and the temporal evolution of Convective Available Potential Energy (CAPE) before, during and after the events. In general, the vertical structure of the atmospheric condition from the MPAS simulations is similar in both cases. For instance, in both cases, MPAS simulations (MPAS60_CFSR and MPAS60_ERA5) feature a relatively high MSE gradient (between the surface and the mid-level of the atmosphere) a day before the events (Figures 4.8e-f and 4.9e-f). This relatively high MSE gradient is associated with a higher value of CAPE (Figure 4.8g-h and 4.9g-h), meaning that the atmosphere was more unstable that day, producing a stronger updraft. These atmospheric conditions are consistent with the fact that the MPAS model (MPAS60_CFSR and MPAS60_ERA5) simulates the peak of the temporal evolution of rainfall a day before the events, as in the observation dataset (Figures 4.8g-h and 4.9g-h). In addition, the reanalysis datasets that were used to initialise the model (CFSR and ERA5) in the two cases present a similar vertical profile of the MSE and the CAPE (Figures 4.8a-b and 4.9a-b). For example, the high MSE gradient is observed a day before the extreme rainfall event day (30 June 2007 in Case Study 1 and 21 July 2017 in Case Study 2), and its associated CAPE is the highest (Figures 4.8c-d and 4.9c-d). However, although this is a good atmospheric condition for relatively strong convection, the corresponding amount of rainfall is not the peak in the temporal evolution of rainfall. For instance, in Case Study 1, the timing of the peak CAPE and the peak rainfall is

delayed by two days for the CFSR dataset and by one day for the ERA5 dataset. By contrast, in Case Study 2, this timing is delayed by one day for the CFSR dataset and two days for the ERA5 dataset. These conditions could be attributed to the time evolution of Convective Inhibition (CIN).

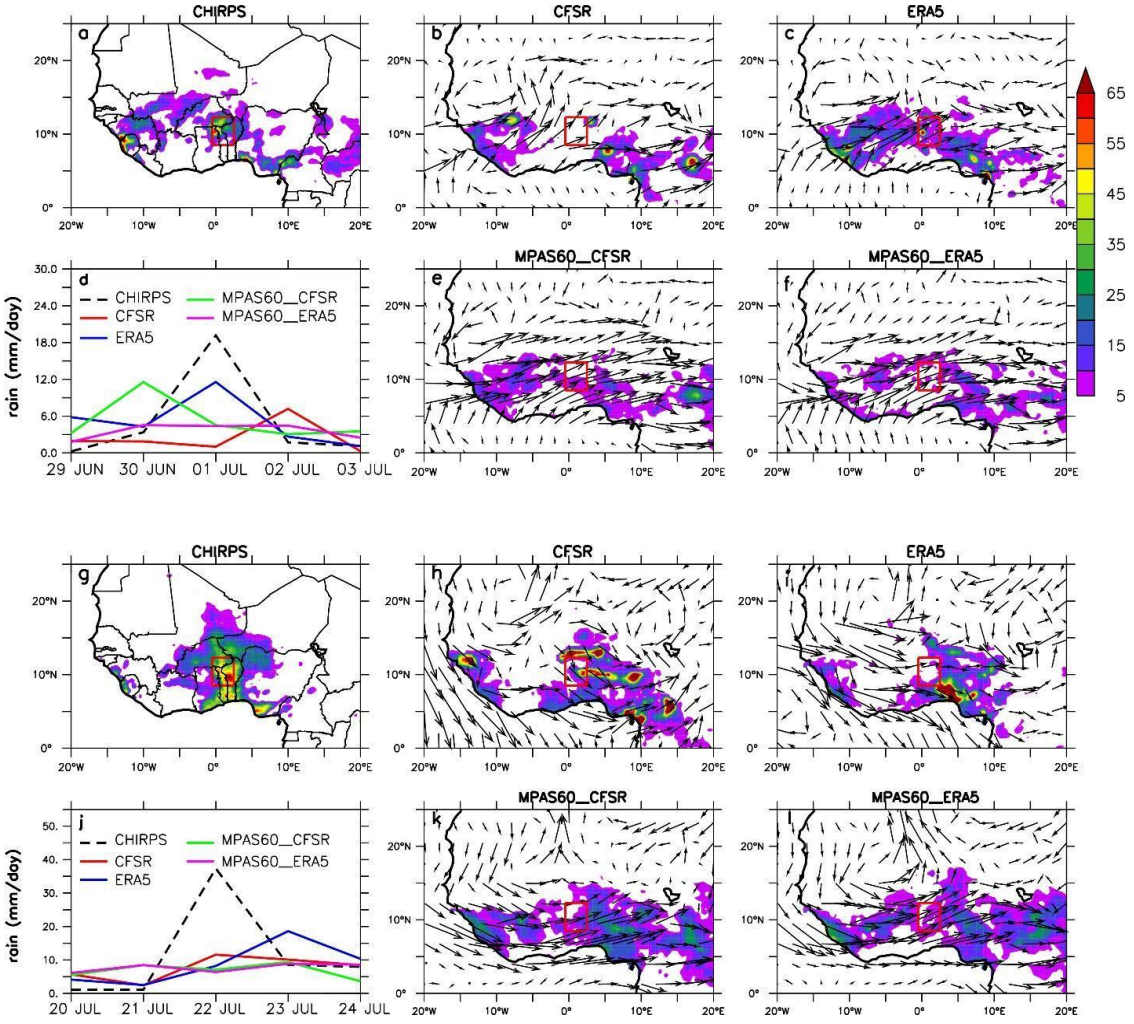

Figure 4.7: Simulated extreme rainfall event (shaded, in mm/day) using CFSR and ERA5 as initial conditions datasets: a-b-c-d-e-f for 1 July 2007 (Case Study 1) and g-h-i-j-k-l for 22 July 2017 (Case Study 2). The vectors show the moisture flux at 850hPa (units: 10^3 g $kg^{-1}ms^{-1}$).

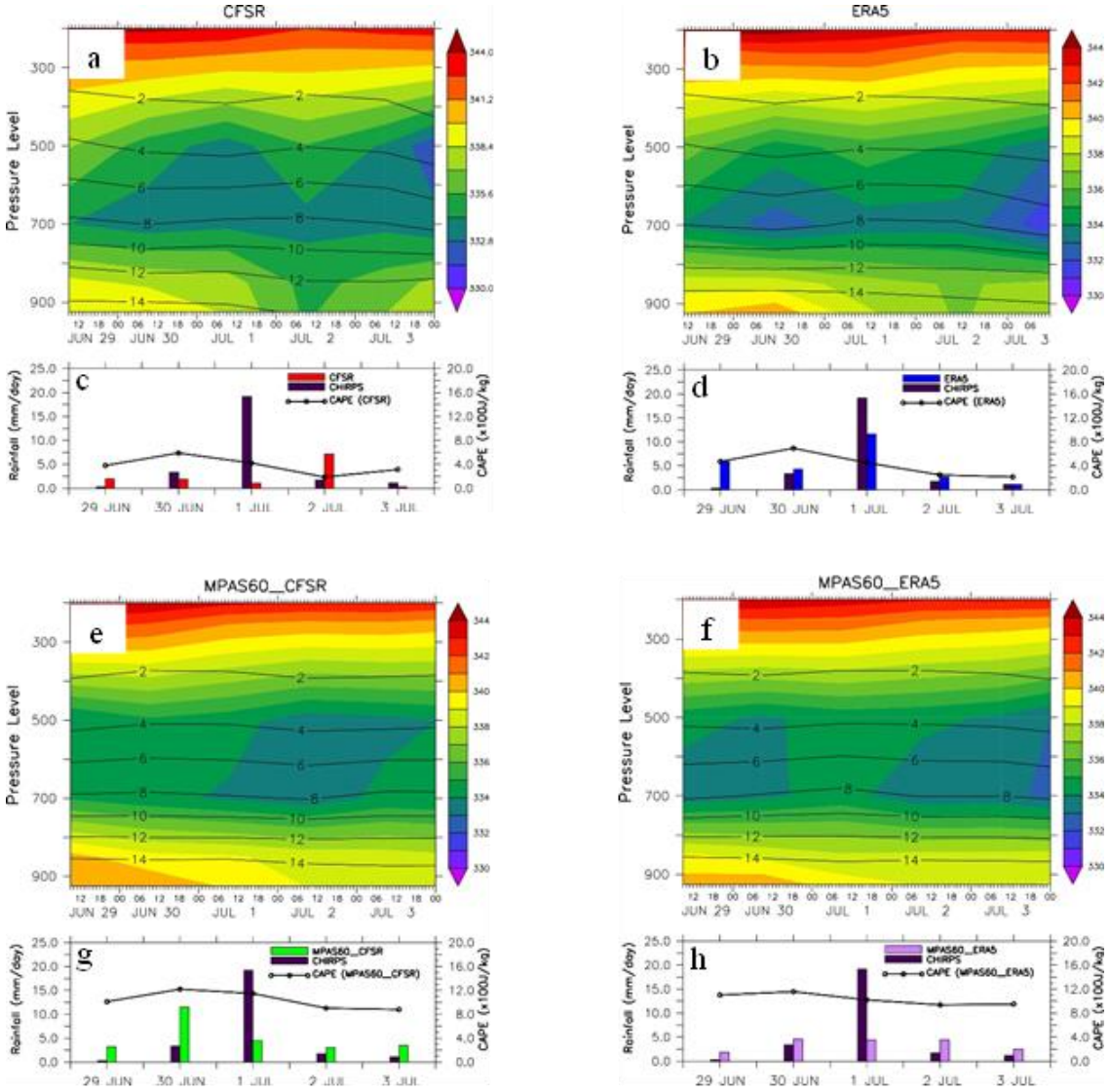

Figure 4.8: The temporal evolution of the vertical profile of the Moist Static Energy (MSE; shaded) and the specific humidity (contour) on 1 July 2007 (Case Study 1) is shown in panels a-b-e-f for the CFSR dataset, ERA5, MPAS60_CFSR, and MPAS60_ERA5) respectively. The temporal evolution of rainfall and the CAPE are shown in panels c-d-g-h. The black bars represent the observed rainfall (CHIRPS), and the red bars represent the CFSR rainfall, the blue bars represent the ERA5 rainfall. The green bars represent the MPAS60_CFSR rainfall, the purple bars represent the MPAS60_ERA5, and the black line represents the simulated CAPE for both initial datasets. All the values are averaged over the Oti River basin.

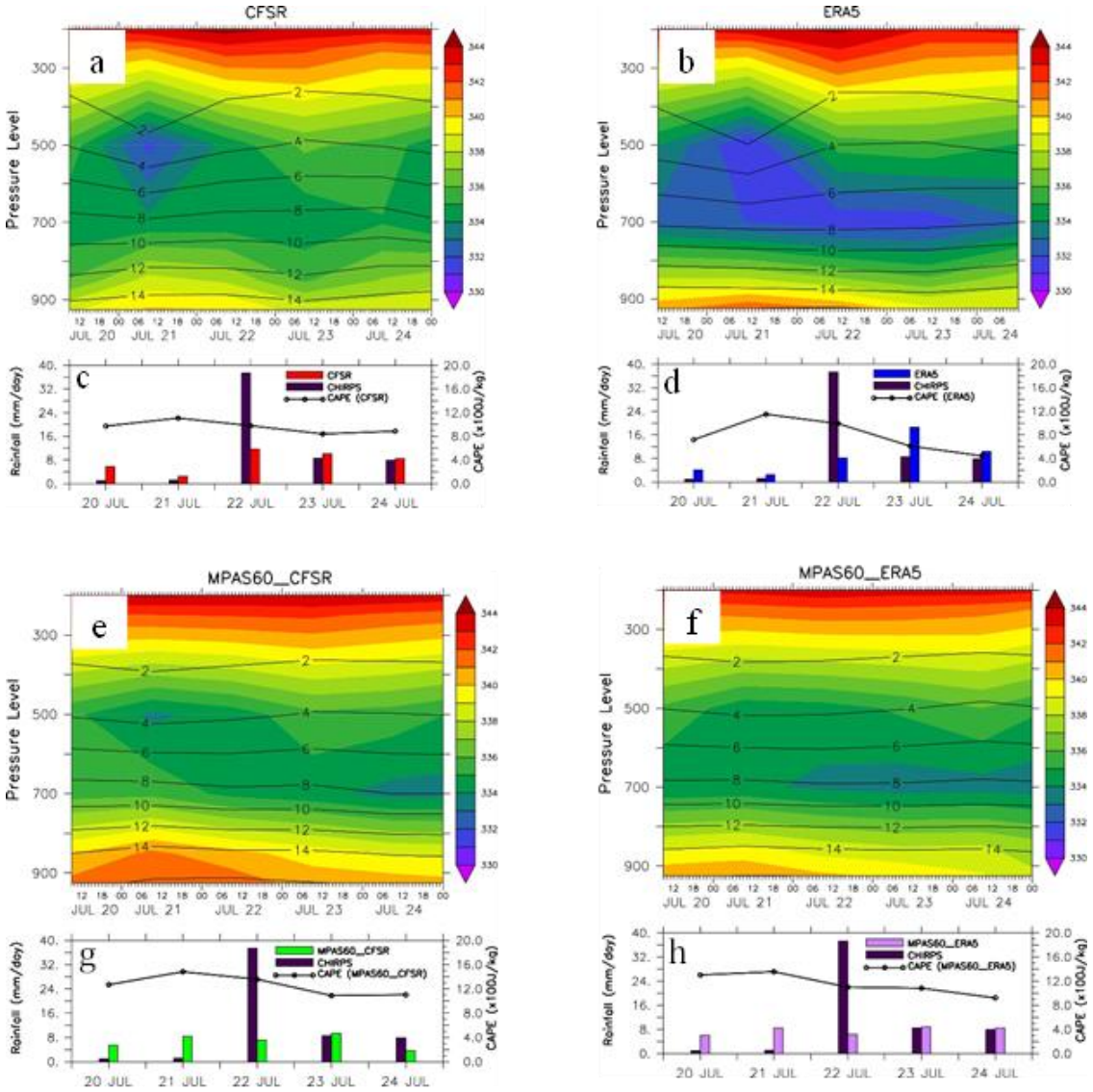

Figure 4.9: The temporal evolution of the vertical profile of the Moist Static Energy (MSE; shaded) and the specific humidity (contour) on 22 July 2007 (Case Study 1) is shown in panels a-b-e-f for the CFSR dataset, ERA5, MPAS60_CFSR, and MPAS60_ERA5) respectively. The temporal evolution of rainfall and the CAPE are shown in panels c-d-g-h. The black bars represent the observed rainfall (CHIRPS), and the red bars represent the CFSR rainfall, the blue bars represent the ERA5 rainfall. The green bars represent the MPAS60_CFSR rainfall, the purple bars represent the MPAS60_ERA5, and the black line represents the simulated CAPE for both initial datasets. All the values are averaged over the Oti River basin

4.1.2.2 Sensitivity to model resolution

Figure 4.10 shows the sensitivity of MPAS in simulating the extreme rainfall events to initial conditions and model resolution in Case Study 1. It shows that regardless of the initial condition (CFSR and ERA5 datasets), MPAS15, MPAS10 and MPAS03 give similar rainfall regimes across West Africa. In the case of CFSR data used as the initial condition, the model simulations (MPAS15, MPAS10 and MPAS03) feature the highest rainfall intensity over the south-eastern part of Nigeria and along Cameroon Mountain (Figure 4.10a-b-c). Though the simulation underestimated the observed extreme rainfall intensity over the Oti River basin (Figure 4.7a), the MPAS model at 60–03km variable resolution did improve the simulation of the extreme rainfall events compared to the simulated events at 60–10km and 60–15km. The strong convergence of moisture flux at 850hPa from the ocean over the Oti River basin (Figure 4.10c) may explain the improvement of the simulated rainfall intensity at 60–03km resolution. In addition, the MPAS simulations replicated the peak of the temporal evolution of rainfall over the Oti River basin as the observed dataset does, and the peak increases as the model resolution increases (Figure 4.10g). Using ERA5 to initialise the model, the simulations (MPAS_15, MPAS_10 and MPAS03) also gave similar rainfall regimes over West Africa, where the highest rainfall intensity features, extending from Nigeria to the Central African Republic (Figure 4.10d-e-f). Furthermore, the model improves the simulation of the extreme rainfall events over the Oti River basin as the model resolution increases. However, the model underestimates the spatial pattern of the observed rainfall intensity over the Oti River basin (Figure 4.7a) and shifts the peak of the temporal evolution of the rainfall (Figure 4.10h). Overall, using CFSR to initialise the model at 60–03km variable resolution improved the simulation of the extreme rainfall events of the Oti River basin.

In Case Study 2, the MPAS simulations (MPAS15, MPAS10 and MPAS03) feature similar rainfall patterns over West Africa, independent of the data used as the initial condition (Figure 4.11a-b-c-d-e-f). For example, all the simulations feature the highest rainfall intensity over the Guinea highland, the north-western part of Cote d'Ivoire, and the eastern part of West Africa. However, the simulations seem to shift the rainfall pattern westward over the Oti River basin shown in the observation dataset (Figure 4.7g). Nevertheless, regardless of the initial conditions (CFSR and ERA5), the MPAS model at 60–03km improved the simulation of the extreme rainfall events over the Oti River basin compared to the model at 60–15km and 60–10km. The moisture flux field at 850hPa is not enough to explain this result since most of the moisture is from the continent (Figure 4.11; vector). In addition, the temporal evolution of the rainfall over the Oti River basin shows that the model simulates the peak a day before the event using CFSR and ERA5 as initial conditions (Figure 4.11g-a).

To understand the extreme rainfall events simulation over the Oti River basin at different model resolutions using CFSR and ERA5 datasets as initial conditions, one cannot rely only on the moisture flux. In Case Study 1, and considering the CFSR as the initial condition dataset, the vertical structure of the MSE from the three MPAS simulations (MPAS15, MPAS10 and MPAS03) is similar (Figures 4.12a, 4.13a and 4.14a). For example, the three simulations feature the highest MSE gradient and the highest CAPE on 30 June 2007 (a day before the event), meaning a strong convective activity that day. However, the simulated maximum precipitation occurred the following day, as in the observation data (Figures 4.12c, 4.13c and 4.14c). This result is consistent with the study by Lee et al. (2007) that used three general circulation models to examine the relation between CAPE and rainfall at diurnal scales. The study found several hours of time lag between maximum CAPE and maximum rainfall over the tropical region.

Subrahmanyam et al. (2015) argued that the relationship between CAPE and rain is crucial in developing convective parameterization schemes for numerical models. Considering the ERA5 dataset as the initial condition, the three MPAS simulations (MPAS15, MPAS10 and MPAS03) also feature the highest MSE gradient (between the surface and the middle altitude of the atmosphere) and the CAPE on 30 June 2007 (Figures 4.12b, 4.13b and 4.14b). Still, the simulated maximum rainfall timing is significantly shifted with respect to the maximum CAPE by two days and with respect to the observed maximum rainfall by one day (Figures 4.12d, 4.13d and 4.14d).

In Case Study 2, and considering the CFSR dataset as the initial condition, the MSE gradient and the CAPE distributions are similar for the three simulations (Figures 4.12e, 4.13e and 4.14e). For instance, the MPAS simulations feature the highest MSE gradient on 21 July 2017, while the corresponding CAPE is not the highest (Figures 4.12g, 4.13g and 4.14g). Though this CAPE value is not the highest in the simulations (but > 1200 J/kg), the model simulates the maximum rainfall on 21 July 2017 (a day before the event) for the three resolutions (60–15km, 60–10km, and 60–03km). This could be because the CAPE values that day were high enough to trigger a relatively strong convective activity. Similarly, with the ERA5 dataset as the initial condition, the MPAS simulations (MPAS15, MPAS10 and MPAS03) show the same MSE gradient pattern and CAPE's temporal evolution (Figures 4.12f-h, 4.13f-h and 4.14f-h). For example, the CAPE value decreases with a decreasing MSE gradient. However, the highest simulated CAPE for the three resolutions does not match the simulated rainfall peak. Instead, the simulated maximum rainfall timing is significantly shifted with respect to the maximum CAPE by four days for the three resolutions. Overall, the simulations show that using CFSR as the initial condition at 60–03km variable

resolution improves the simulation of the extreme rainfall events over Oti River basin in both cases.

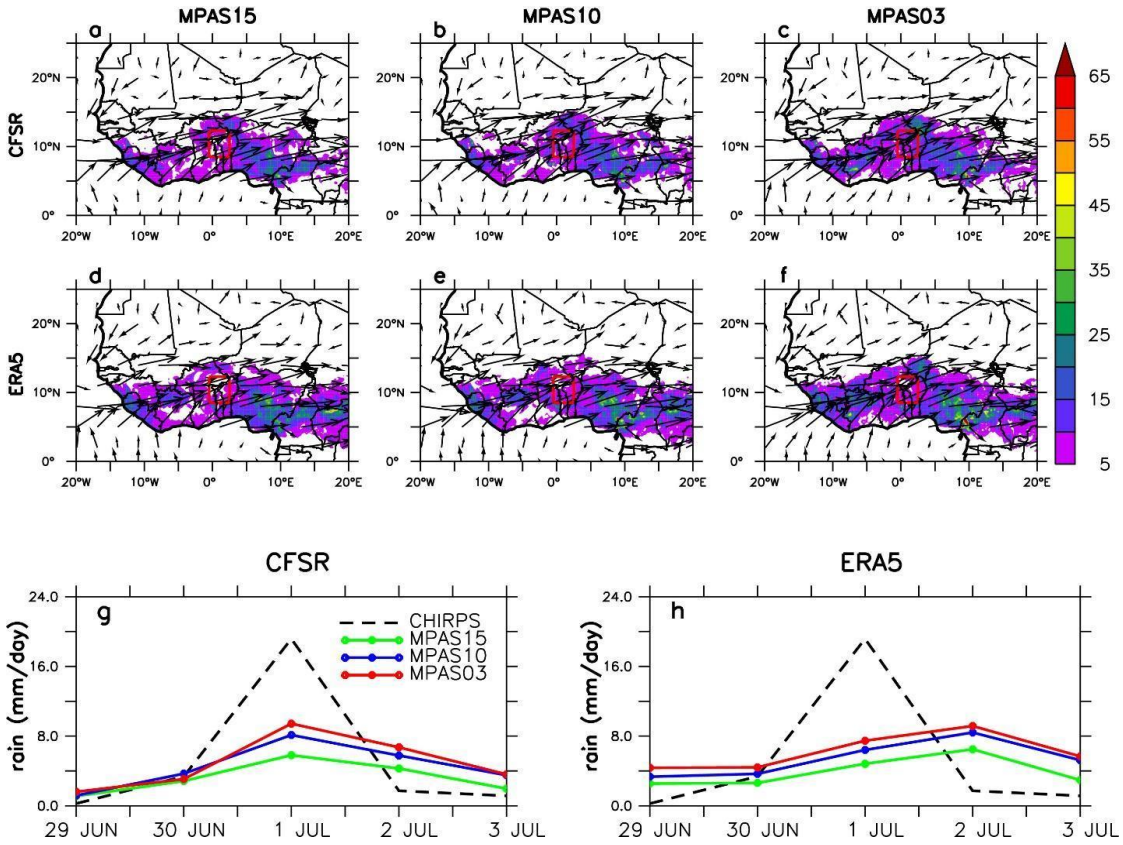

Figure 4.10: Simulated extreme rainfall events on 1 July 2007 (Case Study 1) (shaded, in mm/day) at 60–15km, 60–10km, and 60–03km variable resolution using CFSR and ERA5 as initial conditions dataset. The vectors show the moisture flux at 850hPa (units: 10^3 g $kg^{-1}ms^{-1}$).

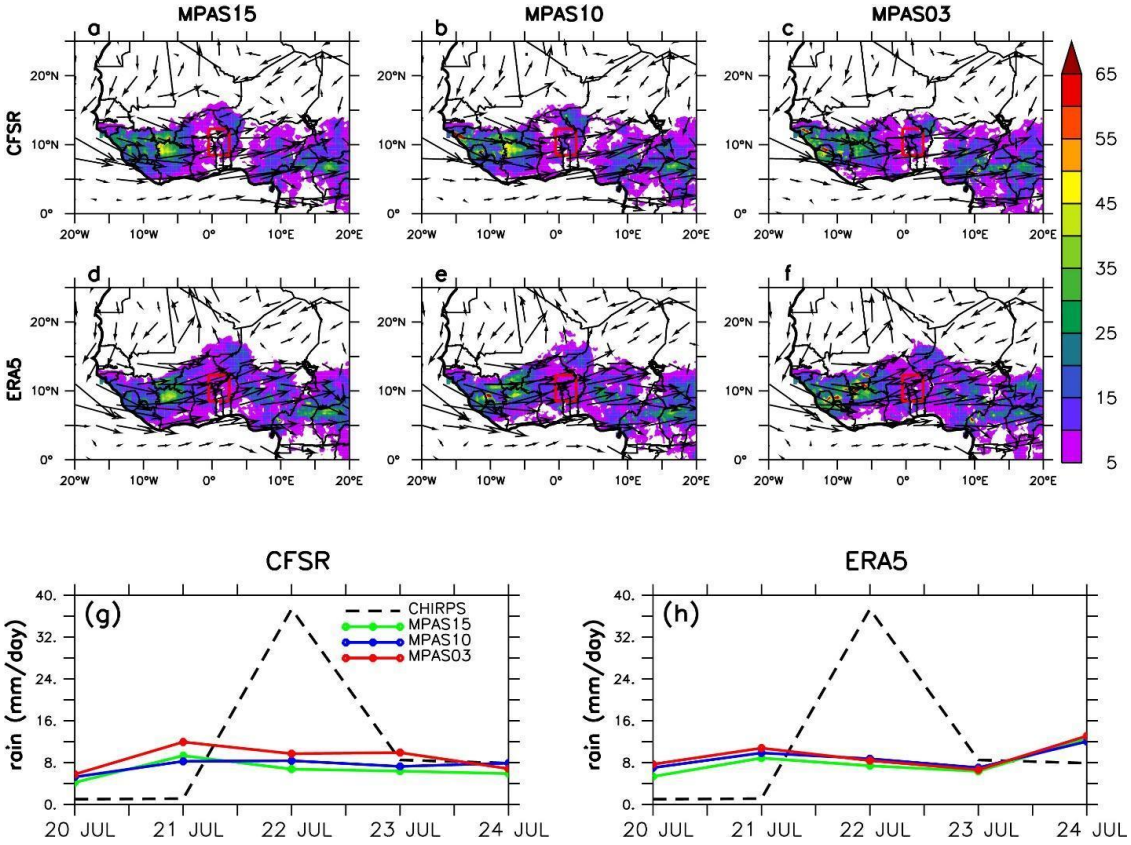

Figure 4.11: Simulated extreme rainfall events on 22 July 2017 (Case Study 2) (shaded, in mm/day) at 60–15km, 60–10km, and 60–03km variable resolution using CFSR and ERA5 as initial condition datasets. The vectors show the moisture flux at 850hPa (units: 10^3 g $kg^{-1}ms^{-1}$).

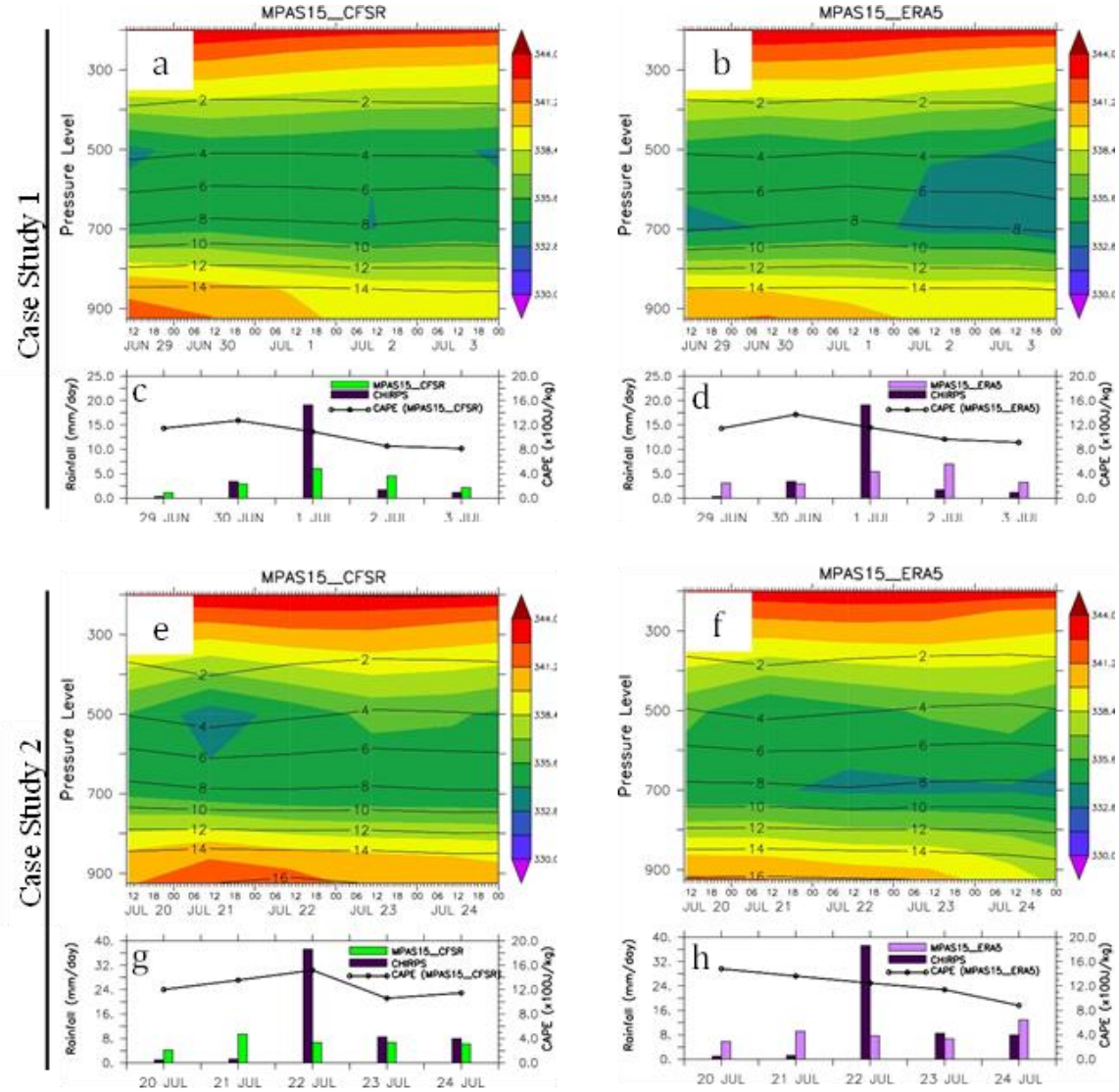

Figure 4.12: Same as figures 8 and 9, but for variable resolution 60-15 km

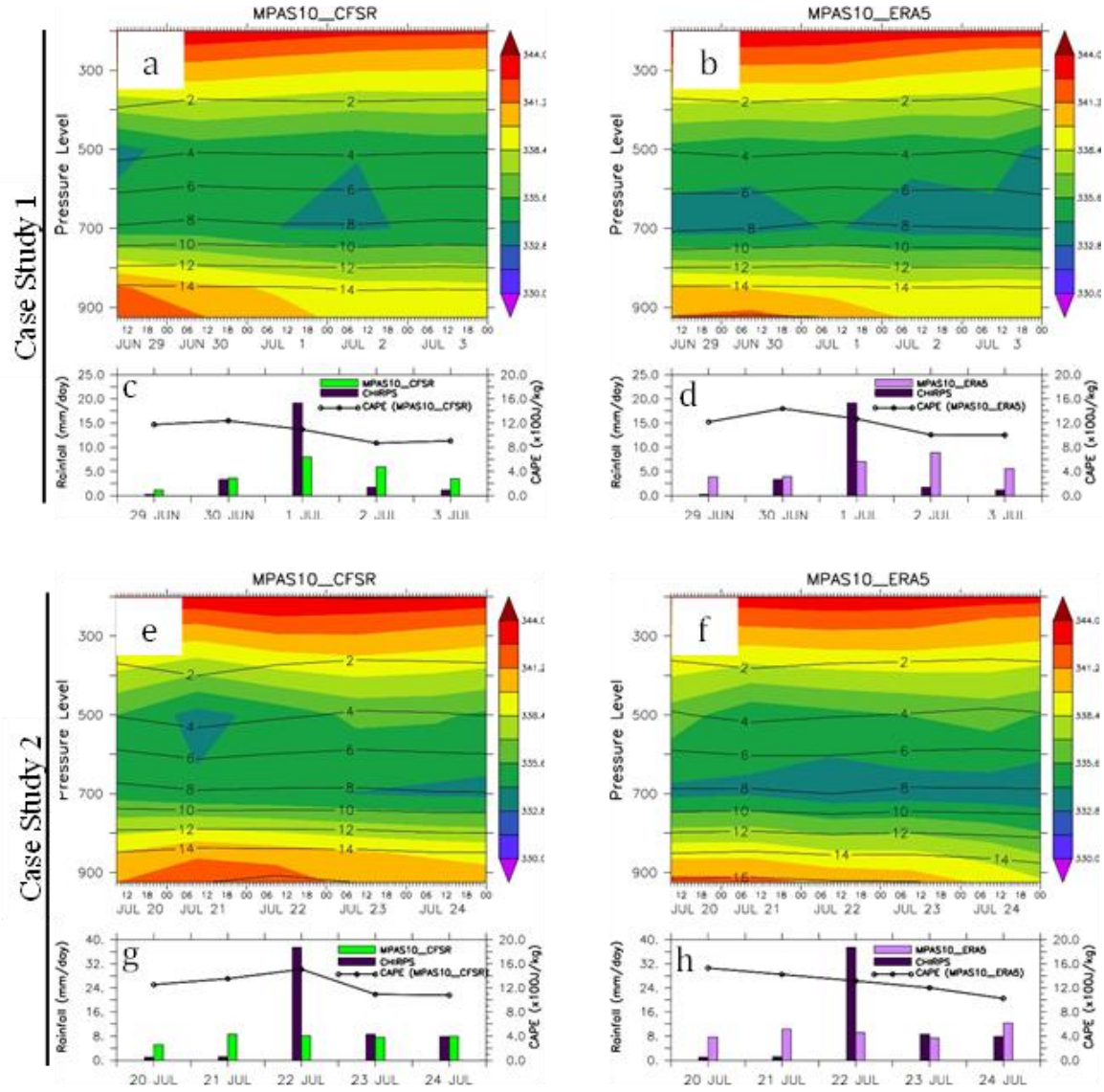

Figure 4.13: Same as figures 8 and 9, but for variable resolution at 60–10km.

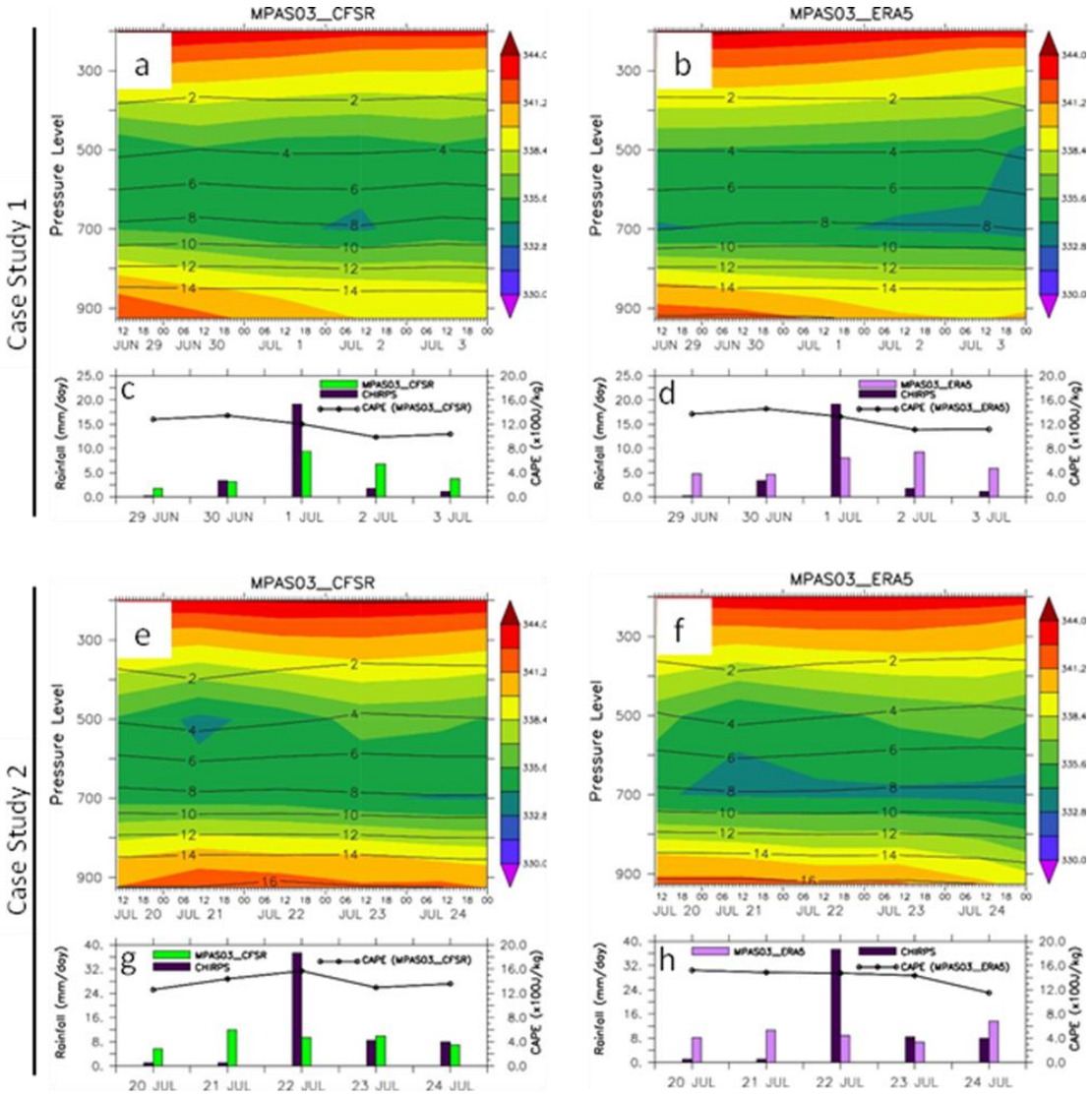

Figure 4.14: Same as figures 8 and 9, but for variable resolution at 60–03km.

4.2 SIMULATION OF FLOOD EVENT USING HEC-RAS MODEL

4.2.1 Temporal evolution of rainfall and river flow

Figure 4.15 shows the seasonal variation of the Oti River flow and precipitation datasets in Mango city over six years (2015-2020). It shows that the amount and timing of precipitation significantly influence river flow. For instance, the flow is relatively low during the driest months (e.g., 10.37 m^3s^{-1} in February) and quite high during the rainy season (e.g., 483.28 m^3s^{-1} in September). However, while the precipitation peak is recorded in July-August, the flow's peak is recorded in September. This suggests that the precipitation recorded at Mango is not the only contribution to the magnitude of river flow in Mango. Other factors, such as the magnitude of antecedent catchment water storage, including soil moisture, groundwater, the slope, and the topography of the watershed (Ye et al., 2017); Malede et al., 2022; Cigizoglu et al., 2005), may contribute to the observed time lag between the rainfall peak in August and the flow peak in September. Along the Oti River, especially in Mango, flood events often occur between July and October when the rainy season is well established. However, for certain devastating events that can occur within a few days, flow data at a daily timescale is needed to understand the flood's characteristics and thus prevent their impacts.

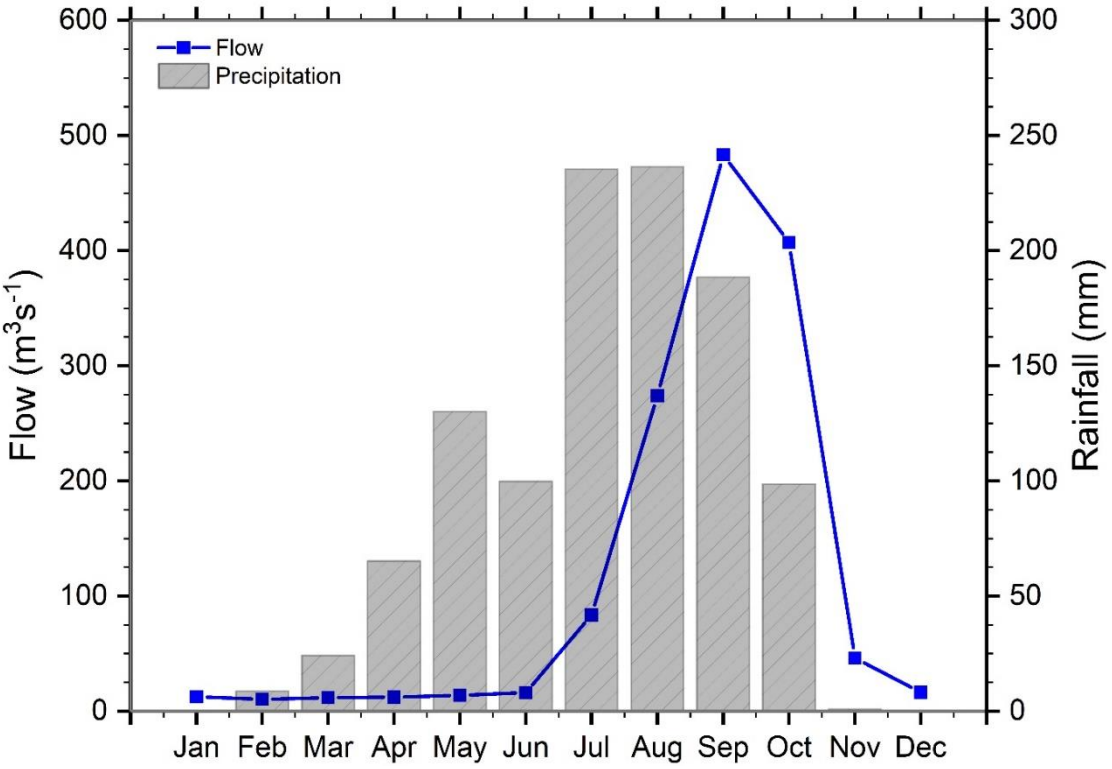

Figure 4.15: Seasonal variation of rainfall and river flow at Mango hydrological and meteorological stations over six years (2015-2020).

Figure 4.16 shows the temporal evolution of river flow in Mango along the Oti River at a daily timescale from 2015 to 2020. Generally, the maximum flow along the Oti River at Mango station is recorded between the end of September and earlier in October and ranged between 371.37 m^3s^{-1} on 19 October 2019 to 912.62 m^3s^{-1} on 2 and 3 October 2020. For example, the maximum flows in 2015 (867.25 m^3s^{-1}) and 2018 (857.73 m^3s^{-1}) were observed on 28 September and 29 September, respectively, while in 2016 (705 m^3s^{-1}) and 2020 (912.62 m^3s^{-1}), they were observed on 01-02 October and 02-03 October, respectively. Furthermore, Figure 4.16 shows that the maximum flows in 2015, 2016, 2018, and 2020 are higher than the maximum annual mean flow, while the flows in 2017 and 2019 are lesser. Given the highest values of the maximum flows, especially in 2020 along the Oti River in Mango, it is essential to investigate how these flows could be translated into flood extent, which is crucial for flood risk preparedness. So, in this study, we considered the year 2020 for further analysis.

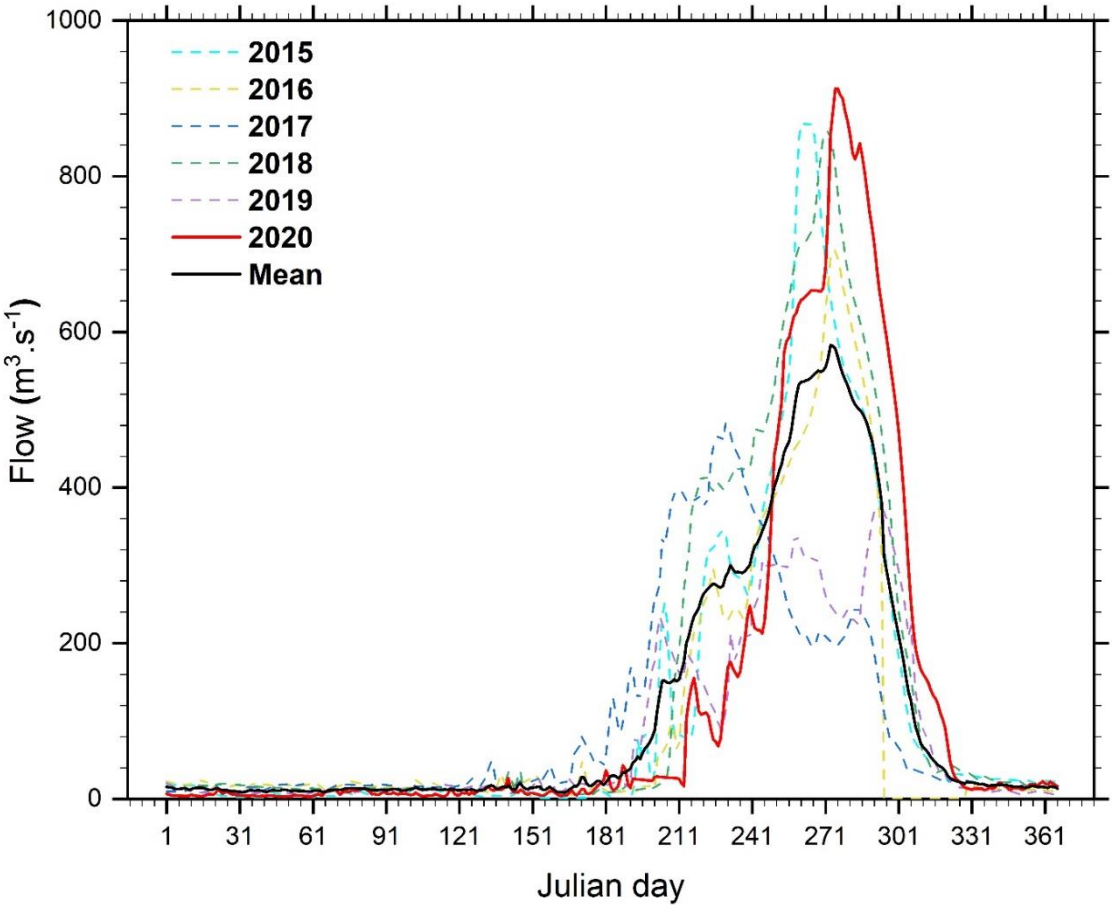

Figure 4.16: Daily variation of river flow at Mango hydrological station from 2015 to 2020.

Figure 4.17 presents the diurnal variation of river flow and precipitation in 2020, and it shows a lag time between the maximum rainfall and the maximum river flow. For example, while the maximum rainfall was recorded on 8 September 2020, the maximum river flow was observed almost one month later on 01 and 02 October 2020. In addition, rainfall amounts at the Mango weather station on the days of the recorded maximum flow are zero on 1 October and 1.3 mm on 02 October. This suggests that the observed maximum river flow on 01 and 02 October 2020 could be due to the rainfall in the previous month of September and other factors, as discussed previously. Besides the temporal characteristics of rainfall and river flow we have discussed previously, we are also motivated by understanding how the flow along the Oti River in Mango could be translated into flood extent, which is crucial for flood risk preparedness. So, in the next section, we considered the year 2020 for flood simulation.

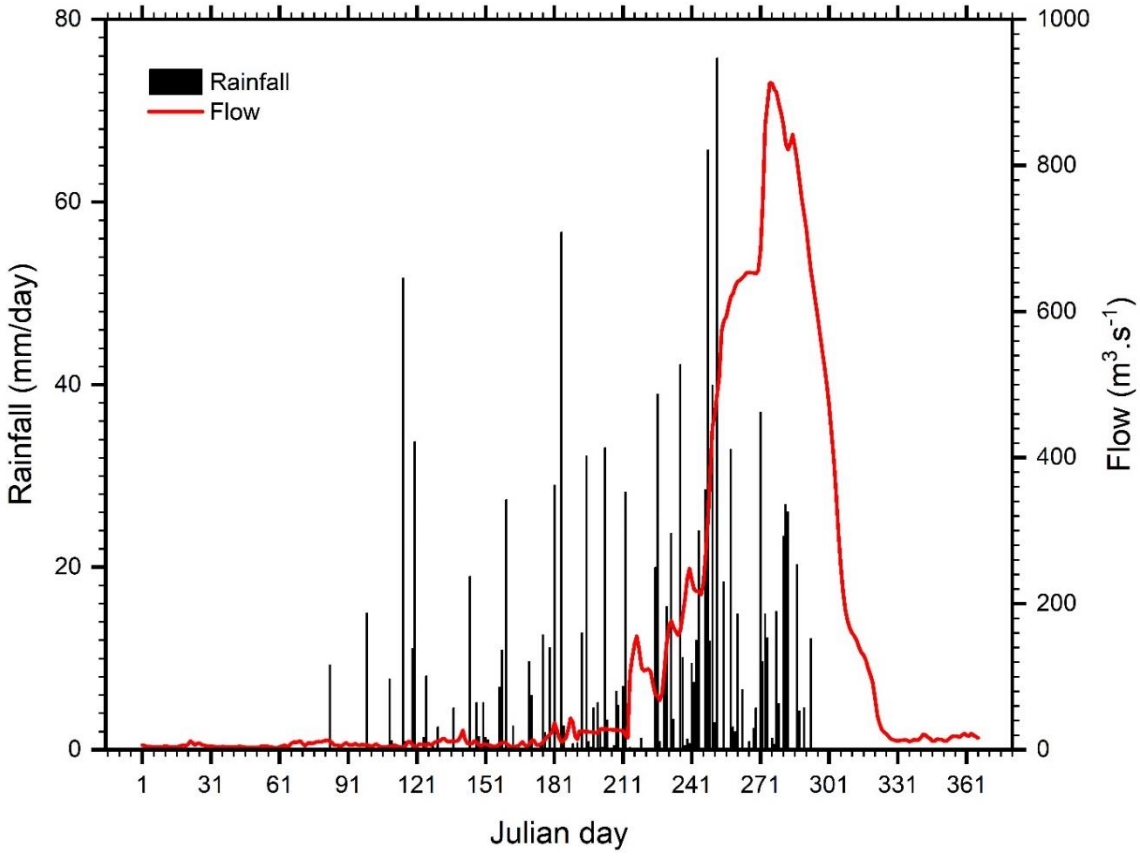

Figure 4.17: Daily variation of rainfall and river flow at Mango stations for the year 2020.

4.2.2 Performance of HEC-RAS model in simulating a real flood event

The hydraulic model evaluation against observations is generally based on quantifiable variables like flood extent and water velocity or depth. Therefore, a model that performs well in capturing these characteristics may be used for flood hazard assessment and thus indicate the vulnerability of built-up areas or farmlands to hydrological events with possible destructive impacts. In this study, we evaluated the performance of HEC-RAS 2D in simulating actual flood events considering the flood extent. The flood velocity and the water depth were not considered because the only available observed flood characteristic is the flood extent. So, figure 7 shows the simulated and observed flood extent on 17 October 2020 in Mango along the Oti River. Generally, the simulated flood extent agrees well with the observed one. It also agrees with the local topography (Figures 6a for the observed and 6b for the simulated one). However, while the model underestimates the expanse in some parts of the simulation area, it overestimates it in others, especially in areas A and B. Regarding the maximum inundation area, the HEC-RAS model gives an inundation area of 4.84 km2 (51.54% of the simulation area), while the observed inundation area is 4.10 km2 (43.74% of the simulation area). Besides the simulation of a actual flood event on 17 October 2020, we designed hypothetic modeling scenarios to evaluate the effects of combined fluvial and pluvial floods and the impact of various maximum flows (Figure 8) over two selected areas (area A and area B) within the simulation area.

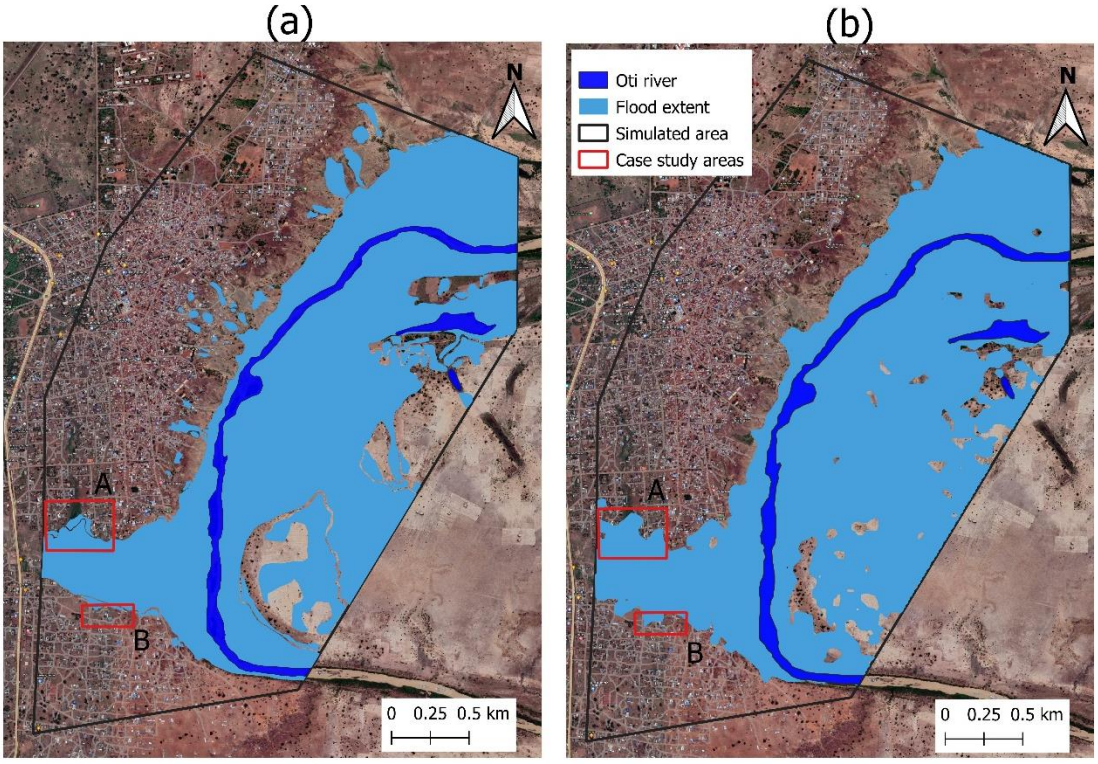

Figure 4.18: Flood extent at Mango on 17 October 2020 as shown by: (a) the observation from Copernicus) and (b) the HEC-RAS simulation using hydrograph data.

4.2.3 Impacts of the simulated composite fluvial and pluvial floods

First, the hypothetic fluvial flood and, secondly, the combined hypothetic fluvial and pluvial floods were simulated under 2D hydrodynamic unsteady flow conditions. Then, the impacts of the floods, in terms of water depth and flood extent, were analysed over the two small areas, A and B. Figures 4.19a and 4.20a show the evolution of the inundation area and depth over area A as a function of the maximum flows of hydrographs. It shows that the combined fluvial and pluvial conditions aggravate the flooding impacts. As a result, the flood extent and depths are more significant than the ones produced by a single type of flooding. For instance, the flood starts over area A from a maximum flow of 60 m3s-1 (fluvial flood) and inundates 0.38 % (0.055 ha) of the area. In contrast, it inundates 34.75 % (4.94 ha) of the area, considering the combined fluvial and pluvial floods (Figure 9a). Similarly, at the beginning of the inundation (flow of 60 m^3s^{-1}), considering the fluvial flood in area A, the recorded maximum flood depth was 0.05 m, while it was 0.27 m for the combined fluvial and pluvial (Figure 10a). Moreover, as the maximum flow of the hydrograph increases, the inundation area and depth increase. However, the deviation between the impacts of the fluvial flood and combined fluvial and pluvial floods remains constant when the flood extent is considered. At the same time, the deviation between the impacts reduces and becomes almost null when the inundation depth is considered. For example, when the maximum flow reaches its highest value (900 m3s-1), 81.16 % and 84.56 % of area A is flooded, considering the fluvial flood and the combined fluvial and pluvial foods, respectively. In contrast, the flood depths for both flood types are almost the same (0.782 m for fluvial flood and 0.784 m for combined fluvial and pluvial flood). This may be linked to soil saturation at a particular time that does not allow the water to infiltrate.

In area B, as in area A, the combined fluvial and pluvial floods enhance the flooding impacts in terms of flood extent and depth. However, the fluvial flood in area B begins from a maximum hydrograph flow of 100 m3s-1, unlike in area A, where the flood starts from 60 m3s-1. While the flood covers 84.56 % of area A with the highest flow value, it covers 70 % of area B with the same flow value. This result in area B may be associated with the high elevation of the floodplain in area B compared to area A. Overall, the flood impacts in area A are more significant compared to area B, and the consequences increase in both cases when the combined flood is considered.

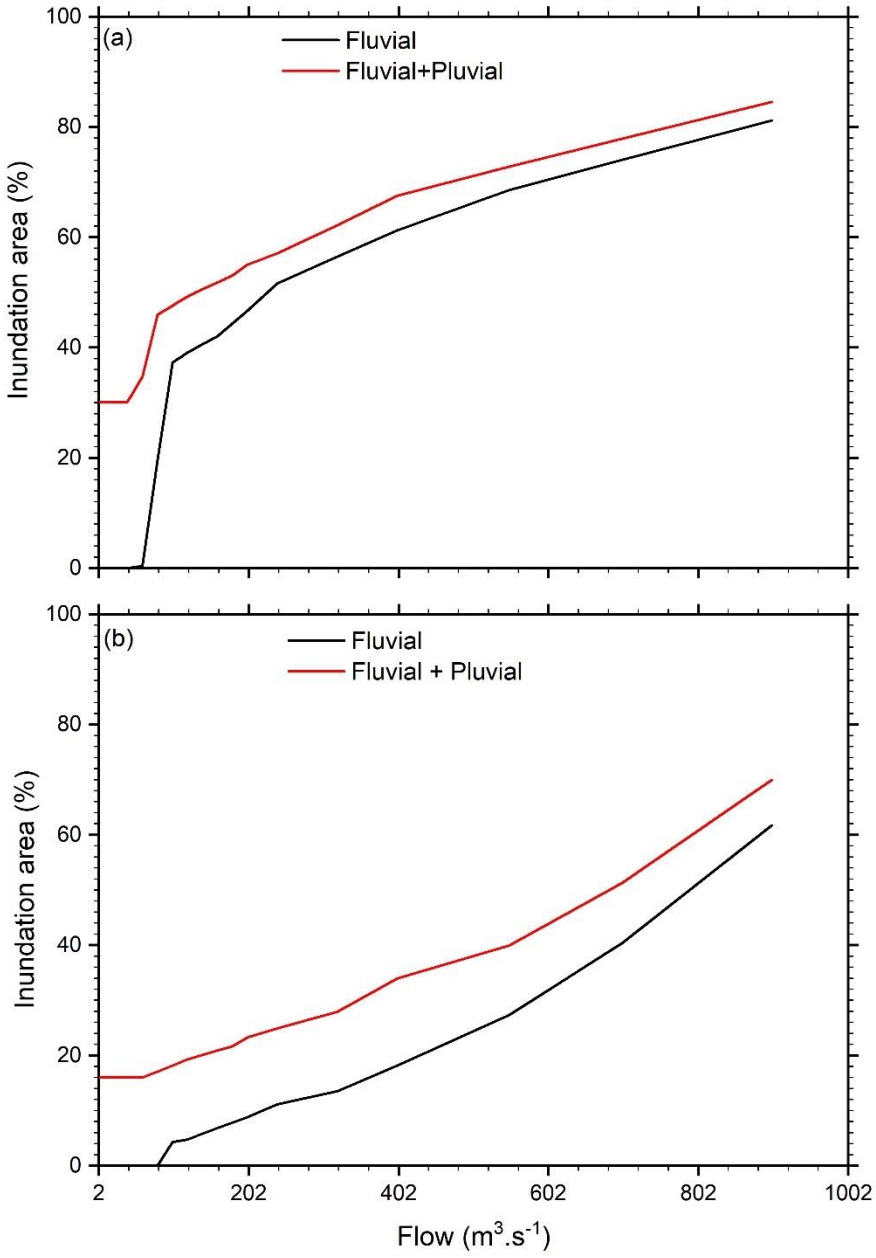

Figure 4.19: The inundation area as function of the maximum river flow of the hypothetical hydrographs, and the combined fluvial and pluvial floods as simulated over: (a) for area A and (b) for area (B).

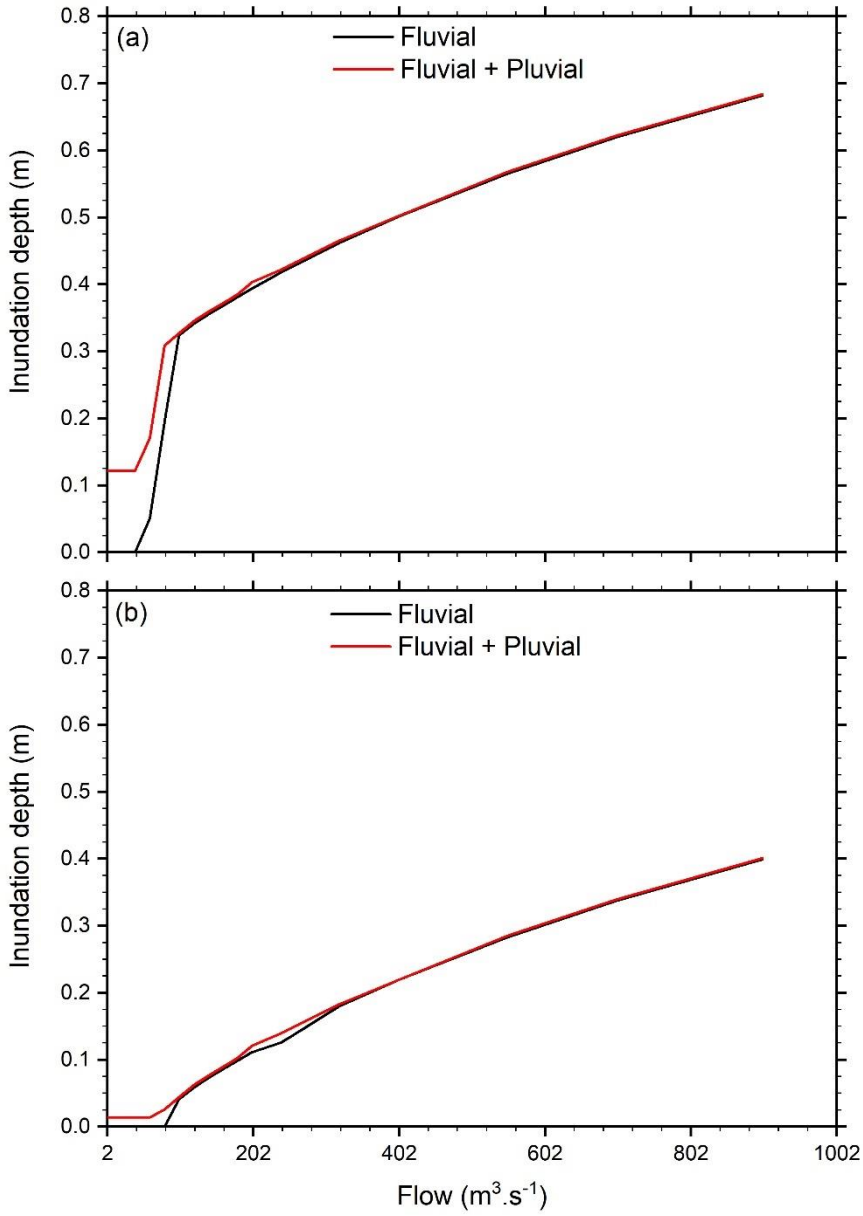

Figure 4.20: The inundation depth as function of the maximum river flow of the hypothetical hydrographs, and the combined fluvial and pluvial floods as simulated: (a) over area A and (b) over area (B).

CHAPTER FIVE

5.0 CONCLUSION AND RECOMMENDATIONS

5.1 CONCLUSION

As part of an effort to improve understanding of extreme rainfall and flood events over West Africa and to enhance prediction, this study has examined the capability of the climate model (MPAS) in simulating extreme rainfall characteristics over West Africa and the ability of the hydraulic model (HEC-RAS) in simulating flood event over the Oti river basin. For the climate study, daily precipitation data from four observation datasets (WFDEI-CRU, AgMERRA, AgCFSR, and CHIRPS) and two reanalyses (CFSR, ERA5) datasets were analysed. In contrast, daily hydrograph data of the Oti river, the DEM, and LUC datasets were used for the hydraulic study. The climate model simulations were mainly compared with the mean of the observation datasets, while the reanalysis datasets were used as initial condition datasets for the model simulation and the dynamic and thermodynamic analysis. First, the climate model evaluation for 30 years run (1981-2010) focused on how well the model reproduced the spatial patterns of eight rainfall indices (WDAYS, Rx5day, R20mm, CWD, RTOT, SDII, R97.5p, and R97.5pTOT) in West Africa. Then, several shorts run of climate simulations with the stretched-grid version of the model to study the sensitivity of the simulated extreme rainfall event to local enhancements in model resolution (i.e., 15 km, 10 km, 3 km) over West Africa, using two cases of extreme rainfall events over the Oti River were performed.

On the other hand, the hydraulic model (HEC-RAS) simulation was compared with an actual flood event in Mango along the Oti river. The model was evaluated using flood extent data from Copernicus-EMS. In addition, seventeen composite fluvial and

pluvial flood scenarios were designed, and their impacts on two selected areas in the Oti River basin were assessed. The impacts were determined by considering each scenario's flood extent and depths.

The results of the study can be summarised as follows:

- MPAS produces the observed spatial patterns of most rainfall indices (e.g., R97.5p, R97.5PTOT, RTOT, WDAYS, CWD, and Rx5day) with a high pattern correlation coefficient ($r > 0.8$), though with some biases. The model struggles to capture the spatial pattern of SDII and R20mm indices over the region.
- MPAS captures the rainfall intensity-frequency curves over the two basins (ORB and GRB). However, it shows substantial discrepancy compared to observation datasets and underestimates the frequency of heavy rainfall in these areas. The rainfall intensity-frequency curves of the reanalysis dataset are within the observed spread, meaning that these data are within the observed uncertainties.
- While MPAS simulates the highest number of WEREs in September over the two basins, the observed mean data reports the highest number in August. Also, while MPAS shows fewer WEREs than the observed mean in June and July over the basins, the CFSR does not even report any WEREs. In addition, MPAS shows a discrepancy compared with the peculiar observation datasets in reporting the number of WEREs.
- In case study 1 and regardless of the initial conditions, MPAS60 gives a credible representation of the three observed rainfall regimes, especially over the ORB. However, it underestimates the spatial rainfall intensity of the HRE over the ORB. Regarding temporal evolution, MPAS60_CFSR captures the event's peak a day before the observed HRE day, while MPAS60_ERA5 reproduces almost a constant rainfall amount throughout the simulation duration.

- In case 2, MPAS60_CFSR and MPAS60_ERA5 fail to replicate the event's intensity over the ORB, as shown in the observation dataset. This is consistent with the simulated temporal evolution of rainfall over the ORB, where the model underestimates and shifts the peak as the observation data does.
- Regardless of the initial condition dataset, MPAS variable resolution (MPAS15, MPAS10, and MPAS03) improves the simulation of the HRE over ORB in case study 1. As the model resolution increases, the model improves the simulated HRE over the basin. However, the model underestimates the observed rainfall intensity over the ORB. While the model replicates the peak of the temporal evolution of rainfall over the basin, as the observed dataset does in the case of CFSR as initial condition data, it shifts the peak a day after the event in the case of ERA5 as initial condition data.
- Similarly, in case study 2, the model improves the simulated HRE over the ORB as the model resolution increases with respect to CFSR and ERA5 data as initial condition data. However, regardless of the initial condition dataset, the three simulations (MPAS15, MPAS10, and MPAS03) reproduce the peak of the temporal evolution of rainfall a day before the event.
- HEC-RAS produces the observed flood extent, which agrees with the local topography; however, the model underestimates the expanse in some parts of the simulation area and overestimates it in others.
- The combined fluvial and pluvial conditions aggravate the flooding impacts over the two areas in terms of flood extent and depth.

- Area A is more vulnerable than area B considering both fluvial floods and the combined fluvial and pluvial floods. It gets flooded more rapidly in area A than in area B.
- The inundation depth in the two areas is more sensitive to the fluvial flood than the pluvial flood.

5.2 RECOMMENDATIONS

The findings of this study demonstrate the capability of MPAS in simulating extreme rainfall over West Africa, but there are opportunities to improve the robustness of the results further. For instance, simulating additional events with varying intensity and geographic location would enable a more robust assessment of the model's ability to simulate extreme rainfall events. Furthermore, while this study utilised a single default physics suite included in MPAS, the use of mesoscale reference, examining the impact of individual parameterization schemes on the characteristics of simulated extreme rainfall events would provide valuable insights into the sensitivity of MPAS. Nevertheless, by applying variable-resolution meshes, this study was able to simulate individual extreme rainfall events at high resolutions that would be computationally impractical in a uniform global model and potentially compromised by lateral boundary conditions in a regional model. Consequently, this study's results provide valuable insights into MPAS's suitability and sensitivity in simulating extreme rainfall, with practical applications for the refinement and implementation of MPAS to provide early warning for extreme rainfall-induced floods across West Africa.

On the other hand, the results of this study demonstrate the capability of HEC-RAS in simulating flood events in Mango, Togo. However, there are opportunities to improve the robustness of the model results further. For example, simulating additional

flood events in different locations would enable a more comprehensive assessment of the model's ability to simulate floods. Additionally, investigating the impact of high-resolution DEMs on the characteristics of simulated flood events would provide valuable insights into the sensitivity of HEC-RAS. Furthermore, incorporating observed flood characteristics like flood depth would benefit model evaluation. Despite these limitations, this study was able to simulate the actual flood event using a 10m resolution of DEM, which agrees with the observed flood extent. Therefore, the study provides valuable insights into the practical application and implementation of HEC-RAS for early warning of flood events across West Africa.

REFERENCES

Abba Omar, S., & Abiodun, B. J. (2017). How well do CORDEX models simulate extreme rainfall events over the East Coast of South Africa? *Theoretical and Applied Climatology*, *128*(1–2), 453–464. https://doi.org/10.1007/s00704-015-1714-5

Abiodun, B. J., Abba Omar, S., Lennard, C., & Jack, C. (2016). Using regional climate models to simulate extreme rainfall events in the Western Cape, South Africa. *International Journal of Climatology*, *36*(2), 689–705. https://doi.org/10.1002/joc.4376

Abiodun, B. J., Adegoke, J., Abatan, A. A., Ibe, C. A., Egbebiyi, T. S., Engelbrecht, F., & Pinto, I. (2017). Potential impacts of climate change on extreme precipitation over four African coastal cities. *Climatic Change*, *143*(3–4), 399–413. https://doi.org/10.1007/s10584-017-2001-5

Abiodun, B. J., Gutowski, W. J., Abatan, A. A., & Prusa, J. M. (2011). CAM-EULAG: A non-hydrostatic atmospheric climate model with grid stretching. *Acta Geophysica*, *59*(6), 1158–1167. https://doi.org/10.2478/s11600-011-0032-2

Abiodun, B. J., Mogebisa, T. O., Petja, B., Abatan, A. A., & Roland, T. R. (2019). Potential impacts of specific global warming levels on extreme rainfall events over southern Africa in CORDEX and NEX-GDDP ensembles. *International Journal of Climatology*, *40*(6), 3118–3141. https://doi.org/10.1002/joc.6386

Agnihotri, G., & Dimri, A. P. (2015). Simulation study of heavy rainfall episodes over the southern Indian peninsula. *Meteorological Applications*, *22*(2), 223–235. https://doi.org/10.1002/met.1446

Akinsanola, A. A., & Zhou, W. (2019a). Projection of West African summer monsoon rainfall in dynamically downscaled CMIP5 models. *Climate Dynamics*, *53*(1–2), 81–95. https://doi.org/10.1007/s00382-018-4568-6

Akinsanola, A. A., & Zhou, W. (2019b). Projections of West African summer monsoon rainfall extremes from two CORDEX models. *Climate Dynamics*, *52*(3–4), 2017–2028. https://doi.org/10.1007/s00382-018-4238-8

Amisigo, B. A., McCluskey, A., & Swanson, R. (2015). Modeling impact of climate change on water resources and agriculture demand in the Volta Basin and other basin systems in Ghana. *Sustainability (Switzerland)*, *7*(6), 6957–6975. https://doi.org/10.3390/su7066957

Amoussou, E., Awoye, H., Vodounon, H. S. T., Obahoundje, S., Camberlin, P., Diedhiou, A., Kouadio, K., Mahé, G., Houndénou, C., & Boko, M. (2020). Climate and extreme rainfall events in the mono river basin (West Africa): Investigating future changes with regional climate models. *Water (Switzerland)*, *12*(3). https://doi.org/10.3390/w12030833

Apel, H., Martínez Trepat, O., Nghia Hung, N., Thi Chinh, D., Merz, B., & Viet Dung, N. (2016). Combined fluvial and pluvial urban flood hazard analysis: Concept development and application to Can Tho city, Mekong Delta, Vietnam. *Natural Hazards and Earth System Sciences*, *16*(4), 941–961. https://doi.org/10.5194/nhess-16-941-2016

Argüeso, D., Hidalgo-Muñoz, J. M., Gámiz-Fortis, S. R., Esteban-Parra, M. J., Dudhia, J., & Castro-Díez, Y. (2011). Evaluation of WRF parameterizations for climate studies over southern Spain using a multistep regionalization. *Journal of Climate*, *24*(21), 5633–5651. https://doi.org/10.1175/JCLI-D-11-00073.1

Arnaud, Y., Desbois, M., & Maizi, J. (1992). Automatic tracking and characterization of African convective systems on Meteosat pictures. In *Journal of Applied Meteorology* (Vol. 31, Issue 5, pp. 443–453). https://doi.org/10.1175/1520-0450(1992)031<0443:ATACOA>2.0.CO;2

Balogun, R. A., Adefisan, E. A., Adeyewa, Z. D., & Okogbue, E. C. (2021). Thermodynamic Environment During the 2009 Burkina Faso and 2012 Nigeria Flood Disasters: Case Study. *African Handbook of Climate Change Adaptation*, 1705–1720. https://doi.org/10.1007/978-3-030-45106-6_143

Balogun, R. A., Liu, C., Adeyewa, Z. D., Okogbue, E. C., & Adefisan, E. A. (2019). Intra-seasonal and seasonal variability of convective properties of monsoon precipitation systems over West and Central Africa. *Theoretical and Applied Climatology*, *137*(3–4), 1715–1728. https://doi.org/10.1007/s00704-018-2692-1

Batebana, K., Ogwang, B. A., Ogou, F. K., Mie, Z., Sein, M., Ongoma, V., & Ngarukiyimana, J. P. (2015). Rainfall Characteristics over Togo and their related Atmospheric circulation Anomalies. *Journal of Environmental and Agricultural Sciences*, *5*(October), 34–48. https://www.researchgate.net/publication/282730103

Bekele, T. W., Haile, A. T., Trigg, M. A., & Walsh, C. L. (2022). Evaluating a new method of remote sensing for flood mapping in the urban and peri-urban areas: Applied to Addis Ababa and the Akaki catchment in Ethiopia. *Natural Hazards Research*, *2*(2), 97–110. https://doi.org/10.1016/j.nhres.2022.03.001

Berthou, S., Rowell, D. P., Kendon, E. J., Roberts, M. J., Stratton, R. A., Crook, J. A., & Wilcox, C. (2019). Improved climatological precipitation characteristics over West Africa at convection-permitting scales. *Climate Dynamics*, *53*(3–4), 1991–2011. https://doi.org/10.1007/s00382-019-04759-4

Bodian, A., Dezetter, A., Diop, L., Deme, A., Djaman, K., & Diop, A. (2018). Future climate change impacts on streamflows of Two Main West Africa River Basins: Senegal and Gambia. *Hydrology*, *5*(1). https://doi.org/10.3390/hydrology5010021

Browne, N. A. K., & Sylla, M. B. (2012). Regional climate model sensitivity to domain size for the simulation of the West African summer monsoon rainfall. *International Journal of Geophysics*, *2012*(May 2014). https://doi.org/10.1155/2012/625831

Bullock, O. R., Foroutan, H., Gilliam, R. C., & Herwehe, J. A. (2018). Adding four-dimensional data assimilation by analysis nudging to the Model for Prediction Across Scales - Atmosphere (version 4.0). *Geoscientific Model Development*, *11*(7), 2897–2922. https://doi.org/10.5194/gmd-11-2897-2018

Camargo, S. J., Robertson, A. W., Gaffney, S. J., Smyth, P., & Ghil, M. (2007). Cluster analysis of typhoon tracks. Part II: Large-scale circulation and ENSO. *Journal of Climate*, *20*(14), 3654–3676. https://doi.org/10.1175/JCLI4203.1

Chawla, I., Osuri, K. K., Mujumdar, P. P., & Niyogi, D. (2018). Assessment of the Weather Research and Forecasting (WRF) model for simulation of extreme rainfall

events in the upper Ganga Basin. *Hydrology and Earth System Sciences*, *22*(2), 1095–1117. https://doi.org/10.5194/hess-22-1095-2018

Cheikh, F. (2018). Precipitation trends in the Gambia River Basin (Senegal) for the period 1971-2010. *Glasnik Srpskog Geografskog Drustva*, *98*(2), 45–57. https://doi.org/10.2298/gsgd1802045f

Chen, A. S., Djordjević, S., Leandro, J., & Savić, D. A. (2010). An analysis of the combined consequences of pluvial and fluvial flooding. *Water Science and Technology*, *62*(7), 1491–1498. https://doi.org/10.2166/wst.2010.486

Chen, G., Lan, R., Zeng, W., Pan, H., & Li, W. (2018). Diurnal variations of rainfall in surface and satellite observations at the Monsoon Coast (South China). *Journal of Climate*, *31*(5), 1703–1724. https://doi.org/10.1175/JCLI-D-17-0373.1

Chomba, I. C., Banda, K. E., Winsemius, H. C., Chomba, M. J., Mataa, M., Ngwenya, V., Sichingabula, H. M., Nyambe, I. A., & Ellender, B. (2021). A review of coupled hydrologic-hydraulic models for floodplain assessments in Africa: Opportunities and challenges for floodplain wetland management. *Hydrology*, *8*(1). https://doi.org/10.3390/hydrology8010044

Cifelli, R., Lang, T., Rutledge, S. A., Guy, N., Zipser, E. J., Zawislak, J., & Holzworth, R. (2010). Characteristics of an African easterly wave observed during NAMMA. *Journal of the Atmospheric Sciences*, *67*(1), 3–25. https://doi.org/10.1175/2009JAS3141.1

Cigizoglu, H. K., Bayazit, M., & Önöz, B. (2005). Trends in the maximum, mean, and low flows of Turkish rivers. *Journal of Hydrometeorology*, *6*(3), 280–290. https://doi.org/10.1175/JHM412.1

Climate, J. O. F. (2001). Dai_JClimate_part_I_2001.pdf. *Journal of Climate*, *Dai 1999*, 1092–1111.

Continent, P. (2015). 346 reported disasters 22,773 people dead 98.6 million people affected US$66.5 billion economic damage. *United Nations Office for Disaster Risk Reduction Publications*, *1*, 2. https://www.unisdr.org/we/inform/publications/47804

Cook, K. H., & Vizy, E. K. (2006). Coupled model simulations of the West African monsoon system: Twentieth- and twenty-first-century simulations. *Journal of Climate*, *19*(15), 3681–3703. https://doi.org/10.1175/JCLI3814.1

Crétat, J., Pohl, B., Drobinski, P., & Richard, Y. (2010). Désagrégation numérique de précipitations en Afrique australe et dynamique atmosphérique associée. *Bulletin d'Association de Geographes Francais*, *87*(2), 194–206.

Crétat, J., Vizy, E. K., & Cook, K. H. (2014). How well are daily intense rainfall events captured by current climate models over Africa? *Climate Dynamics*, *42*(9–10), 2691–2711. https://doi.org/10.1007/s00382-013-1796-7

Crétat, J., Vizy, E. K., & Cook, K. H. (2015). The relationship between African easterly waves and daily rainfall over West Africa: observations and regional climate simulations. *Climate Dynamics*, *44*(1–2), 385–404. https://doi.org/10.1007/s00382-014-2120-x

Cui, X., & Li, X. (2009). Diurnal responses of tropical convective and stratiform rainfall

to diurnally varying sea surface temperature. *Meteorology and Atmospheric Physics*, *104*(1–2), 53–61. https://doi.org/10.1007/s00703-008-0016-1

Dai, A. (2001). Global Precipitation and Thunderstorm Frequencies. Part II: Diurnal Variations. *Journal of Climate*, *14*(1963), 1112–1128.

Dai, A. (2006). Precipitation characteristics in eighteen coupled climate models. *Journal of Climate*, *19*(18), 4605–4630. https://doi.org/10.1175/JCLI3884.1

David, A., & Schmalz, B. (2021). A systematic analysis of the interaction between rain-on-grid-simulations and spatial resolution in 2d hydrodynamic modeling. *Water (Switzerland)*, *13*(17). https://doi.org/10.3390/w13172346

Davis, C. A., Ahijevych, D. A., Wang, W., & Skamarock, W. C. (2016). Evaluating medium-range tropical cyclone forecasts in uniform- and variable-resolution global models. *Monthly Weather Review*, *144*(11), 4141–4160. https://doi.org/10.1175/MWR-D-16-0021.1

Dayan, U., Nissen, K., & Ulbrich, U. (2015). Review Article : Atmospheric conditions inducing extreme precipitation over the eastern and western Mediterranean. *Natural Hazards and Earth System Sciences*, *15*(11), 2525–2544. https://doi.org/10.5194/nhess-15-2525-2015

Dhurmea, R. K. (2015). *by Dissertation Submitted in Partial Fulfilment For a Master in Applied Supervisor : September*.

Dirmeyer, P. A., Cash, B. A., Kinter, J. L., Jung, T., Marx, L., Satoh, M., Stan, C., Tomita, H., Towers, P., Wedi, N., Achuthavarier, D., Adams, J. M., Altshuler, E. L., Huang, B., Jin, E. K., & Manganello, J. (2012). Simulating the diurnal cycle of rainfall in global climate models: Resolution versus parameterization. *Climate Dynamics*, *39*(1–2), 399–418. https://doi.org/10.1007/s00382-011-1127-9

Donkin, P. T., & Abiodun, B. J. (2022). Capability and sensitivity of MPAS-A in simulating tropical cyclones over the South-West Indian Ocean. *Modeling Earth Systems and Environment*, *0123456789*. https://doi.org/10.1007/s40808-022-01517-0

Doswell, C. A., Brooks, H. E., & Maddox, R. A. (1996). Flash flood forecasting: An ingredients-based methodology. *Weather and Forecasting*, *11*(4), 560–581. https://doi.org/10.1175/1520-0434(1996)011<0560:FFFAIB>2.0.CO;2

Doswell, C. A., Edwards, R., Thompson, R. L., Hart, J. A., & Crosbie, K. C. (2006). A simple and flexible method for ranking severe weather events. *Weather and Forecasting*, *21*(6), 939–951. https://doi.org/10.1175/WAF959.1

Driver, P., Abiodun, B., & Reason, C. J. C. (2019). Modelling the precipitation response over southern Africa to the 2009–2010 El Niño using a stretched grid global atmospheric model. *Climate Dynamics*, *52*(7–8), 3929–3949. https://doi.org/10.1007/s00382-018-4362-5

Du, Q., Faber, V., & Gunzburger, M. (1999). Centroidal Voronoi tessellations: Applications and algorithms. *SIAM Review*, *41*(4), 637–676. https://doi.org/10.1137/S0036144599352836

Duda, M. G., Fowler, L., Skamarock, B., Roesch, C., Jacobsen, D., & Ringler, O. (2019). *MPAS-Atmosphere Model User's Guide Version 7.0*. *July*.

https://www2.mmm.ucar.edu/projects/mpas/mpas_atmos%0Aphere_users_guide_7.0.pdf

El-Saoud, W. A., & Othman, A. (2022). An integrated hydrological and hydraulic modelling approach for flash flood hazard assessment in eastern Makkah city, Saudi Arabia. *Journal of King Saud University - Science*, *34*(4), 102045. https://doi.org/10.1016/j.jksus.2022.102045

Engel, T., Fink, A. H., Knippertz, P., Pante, G., & Bliefernicht, J. (2017). Extreme Precipitation in the West African Cities of Dakar and Ouagadougou: Atmospheric Dynamics and Implications for Flood Risk Assessments. *Journal of Hydrometeorology*, *18*(11), 2937–2957. https://doi.org/10.1175/JHM-D-16-0218.1

Faye, A., & Akinsanola, A. A. (2022). Evaluation of extreme precipitation indices over West Africa in CMIP6 models. *Climate Dynamics*, *58*(3–4), 925–939. https://doi.org/10.1007/s00382-021-05942-2

Ferrett, S., Yang, G. Y., Woolnough, S. J., Methven, J., Hodges, K., & Holloway, C. E. (2020). Linking extreme precipitation in Southeast Asia to equatorial waves. *Quarterly Journal of the Royal Meteorological Society*, *146*(727), 665–684. https://doi.org/10.1002/qj.3699

Fox-Rabinovitz, M., Cote, J., Dugas, B., Deque, M., McGregor, J. L., & Belochitski, A. (2008). Stretched-grid Model Intercomparison Project: Decadal regional climate simulations with enhanced variable and uniform-resolution GCMs. *Meteorology and Atmospheric Physics*, *100*(1–4), 159–178. https://doi.org/10.1007/s00703-008-0301-z

Fox-Rabinovitz, M. S., Takacs, L. L., Govindaraju, R. C., & Suarez, M. J. (2001). A variable-resolution stretched-grid general circulation model: Regional climate simulation. *Monthly Weather Review*, *129*(3), 453–469. https://doi.org/10.1175/1520-0493(2001)129<0453:AVRSGG>2.0.CO;2

Fundamentals, D. (2007). *年度工作报告 Annual Report 2007*. *October*, 1–10.

Funk, C., Peterson, P., Landsfeld, M., Pedreros, D., Verdin, J., Shukla, S., Husak, G., Rowland, J., Harrison, L., Hoell, A., & Michaelsen, J. (2015). The climate hazards infrared precipitation with stations - A new environmental record for monitoring extremes. *Scientific Data*, *2*, 1–21. https://doi.org/10.1038/sdata.2015.66

Gbobaniyi, E., Sarr, A., Sylla, M. B., Diallo, I., Lennard, C., Dosio, A., Dhiédiou, A., Kamga, A., Klutse, N. A. B., Hewitson, B., Nikulin, G., & Lamptey, B. (2014). Climatology, annual cycle and interannual variability of precipitation and temperature in CORDEX simulations over West Africa. *International Journal of Climatology*, *34*(7), 2241–2257. https://doi.org/10.1002/joc.3834

Gharbi, M., Soualmia, A., Dartus, D., & Masbernat, L. (2016). Comparison of 1D and 2D hydraulic models for floods simulation on the medjerda riverin tunisia. *Journal of Materials and Environmental Science*, *7*(8), 3017–3026.

Gnitou, G. T., Ma, T., Tan, G., Ayugi, B., Nooni, I. K., Alabdulkarim, A., & Tian, Y. (2019). Evaluation of the rossby centre regional climate model rainfall simulations over west africa using large-scale spatial and temporal statistical metrics. In

Atmosphere (Vol. 10, Issue 12). https://doi.org/10.3390/ATMOS10120802

Gounou, A., Guichard, F., & Couvreux, F. (2012). Observations of Diurnal Cycles Over a West African Meridional Transect: Pre-Monsoon and Full-Monsoon Seasons. *Boundary-Layer Meteorology*, *144*(3), 329–357. https://doi.org/10.1007/s10546-012-9723-8

Gray, W. M., & Jacobson, R. W. (1977). Diurnal Variation of Deep Cumulus Convection. In *Monthly Weather Review* (Vol. 105, Issue 9, pp. 1171–1188). https://doi.org/10.1175/1520-0493(1977)105<1171:dvodcc>2.0.co;2

Gu, G., Adler, R. F., Huffman, G. J., & Curtis, S. (2004). African easterly waves and their association with precipitation. *Journal of Geophysical Research: Atmospheres*, *109*(4). https://doi.org/10.1029/2003jd003967

Guha-Sapir, D., Hoyois, P., & Below, R. (2016). Annual Disaster Statistical Review 2015. The numbers and trends Centre for Research on the Epidemiology of Disasters (CRED). *Centre for Research on the Epidemiology of Disasters (CRED) Institute of Health and Society (IRSS) Université Catholique de Louvain – Brussels, Belgium*.

Guo, J., Zhai, P., Wu, L., Cribb, M., Li, Z., Ma, Z., Wang, F., Chu, D., Wang, P., & Zhang, J. (2014). Diurnal variation and the influential factors of precipitation from surface and satellite measurements in Tibet. *International Journal of Climatology*, *34*(9), 2940–2956. https://doi.org/10.1002/joc.3886

Haarsma, R. J., Hazeleger, W., Severijns, C., De Vries, H., Sterl, A., Bintanja, R., Van Oldenborgh, G. J., & Van Den Brink, H. W. (2013). More hurricanes to hit western Europe due to global warming. *Geophysical Research Letters*, *40*(9), 1783–1788. https://doi.org/10.1002/grl.50360

Hagos, S., Leung, R., Rauscher, S. A., & Ringler, T. (2013). Error Characteristics of Two Grid Refinement Approaches in Aquaplanet Simulations: MPAS-A and WRF. *Monthly Weather Review*, *141*(9), 3022–3036. https://doi.org/10.1175/MWR-D-12-00338.1

Hazeleger, W., Van Den Hurk, B. J. J. M., Min, E., Van Oldenborgh, G. J., Petersen, A. C., Stainforth, D. A., Vasileiadou, E., & Smith, L. A. (2015). Tales of future weather. *Nature Climate Change*, *5*(2), 107–113. https://doi.org/10.1038/nclimate2450

He, H., & Zhang, F. (2010). Diurnal variations of warm-season precipitation over Northern China. *Monthly Weather Review*, *138*(4), 1017–1025. https://doi.org/10.1175/2010MWR3356.1

Heinzeller, D., Duda, M. G., & Kunstmann, H. (2016). Towards convection-resolving, global atmospheric simulations with the Model for Prediction Across Scales (MPAS) v3.1: An extreme scaling experiment. *Geoscientific Model Development*, *9*(1), 77–110. https://doi.org/10.5194/gmd-9-77-2016

Hersbach, H., Bell, B., Berrisford, P., Hirahara, S., Horányi, A., Muñoz-Sabater, J., Nicolas, J., Peubey, C., Radu, R., Schepers, D., Simmons, A., Soci, C., Abdalla, S., Abellan, X., Balsamo, G., Bechtold, P., Biavati, G., Bidlot, J., Bonavita, M., … Thépaut, J. N. (2020). The ERA5 global reanalysis. *Quarterly Journal of the Royal Meteorological Society*, *146*(730), 1999–2049. https://doi.org/10.1002/qj.3803

Hertel, T. W. (2016). Food security under climate change. *Nature Climate Change*, *6*(1), 10–13. https://doi.org/10.1038/nclimate2834

Huang, C. Y., Zhang, Y., Skamarock, W. C., & Hsu, L. H. (2017). Influences of large-scale flow variations on the track evolution of typhoons Morakot (2009) and Megi (2010): Simulations with a global variable-resolution model. *Monthly Weather Review*, *145*(5), 1691–1716. https://doi.org/10.1175/MWR-D-16-0363.1

Im, E. S., & Eltahir, E. A. B. (2018). Simulation of the diurnal variation of rainfall over the western Maritime Continent using a regional climate model. *Climate Dynamics*, *51*(1–2), 73–88. https://doi.org/10.1007/s00382-017-3907-3

Imaoka, K., & Spencer, R. W. (2000). Diurnal variation of precipitation over the tropical oceans observed by TRMM/TMI combined with SSM/I. *Journal of Climate*, *13*(23), 4149–4158. https://doi.org/10.1175/1520-0442(2000)013<4149:DVOPOT>2.0.CO;2

Imberger, M., Larsén, X. G., & Davis, N. (2021). Investigation of Spatial and Temporal Wind-Speed Variability During Open Cellular Convection with the Model for Prediction Across Scales in Comparison with Measurements. *Boundary-Layer Meteorology*, *179*(2), 291–312. https://doi.org/10.1007/s10546-020-00591-0

Iroume, J. Y. A., Onguéné, R., Djanna Koffi, F., Colmet-Daage, A., Stieglitz, T., Essoh Sone, W., Bogning, S., Olinga Olinga, J. M., Ntchantcho, R., Ntonga, J. C., Braun, J. J., Briquet, J. P., & Etame, J. (2022). The 21st August 2020 Flood in Douala (Cameroon): A Major Urban Flood Investigated with 2D HEC-RAS Modeling. *Water (Switzerland)*, *14*(11), 1–19. https://doi.org/10.3390/w14111768

Jackson, L. S., Keane, R. J., Finney, D. L., Marsham, J. H., Parker, D. J., Senior, C. A., & Stratton, R. A. (2019). Regional differences in the response of rainfall to convectively coupled Kelvin waves over tropical Africa. *Journal of Climate*, *32*(23), 8143–8165. https://doi.org/10.1175/JCLI-D-19-0014.1

Jiang, J., & Yao, S. (2021). Winter persistent extreme cold events in xinjiang region and their associations with the quasi-biweekly oscillation of the polar front jet. *Atmosphere*, *12*(5). https://doi.org/10.3390/atmos12050597

Jiang, Z., Zhang, D.-L., Xia, R., & Qian, T. (2017). Diurnal Variations of Presummer Rainfall over Southern China. *Journal of Climate*, *30*(2), 755–773. https://doi.org/10.1175/jcli-d-15-0666.1

Ju, L., Ringler, T., & Gunzburger, M. (2011). Voronoi Tessellations and Their Application to Climate and Global Modeling. *Lecture Notes in Computational Science and Engineering*, *80*, 313–342. https://doi.org/10.1007/978-3-642-11640-7_10

Kalthoff, N., Lohou, F., Brooks, B., Jegede, G., Adler, B., Babić, K., DIone, C., Ajao, A., Amekudzi, L. K., Aryee, J. N. A., Ayoola, M., Bessardon, G., Danuor, S. K., Handwerker, J., Kohler, M., Lothon, M., Pedruzo-Bagazgoitia, X., Smith, V., Sunmonu, L., … Knippertz, P. (2018). An overview of the diurnal cycle of the atmospheric boundary layer during the West African monsoon season: Results from the 2016 observational campaign. *Atmospheric Chemistry and Physics*, *18*(4), 2913–2928. https://doi.org/10.5194/acp-18-2913-2018

Katsumata, M., Mori, S., Hamada, J. I., Hattori, M., Syamsudin, F., & Yamanaka, M.

D. (2018). Diurnal cycle over a coastal area of the Maritime Continent as derived by special networked soundings over Jakarta during HARIMAU2010. *Progress in Earth and Planetary Science*, *5*(1). https://doi.org/10.1186/s40645-018-0216-3

Kaunda, C. S., Kimambo, C. Z., & Nielsen, T. K. (2012). Hydropower in the Context of Sustainable Energy Supply: A Review of Technologies and Challenges. *ISRN Renewable Energy*, *2012*, 1–15. https://doi.org/10.5402/2012/730631

Kendon, E. J., Roberts, N. M., Fowler, H. J., Roberts, M. J., Chan, S. C., & Senior, C. A. (2014). Heavier summer downpours with climate change revealed by weather forecast resolution model. *Nature Climate Change*, *4*(7), 570–576. https://doi.org/10.1038/nclimate2258

Kim, H., Lee, M. I., Cha, D. H., Lim, Y. K., & Putman, W. M. (2019). Improved representation of the diurnal variation of warm season precipitation by an atmospheric general circulation model at a 10 km horizontal resolution. *Climate Dynamics*, *53*(11), 6523–6542. https://doi.org/10.1007/s00382-019-04943-6

Kim, I. W., Oh, J., Woo, S., & Kripalani, R. H. (2019). Evaluation of precipitation extremes over the Asian domain: observation and modelling studies. *Climate Dynamics*, *52*(3–4), 1317–1342. https://doi.org/10.1007/s00382-018-4193-4

Kirtsaeng, S., Chantara, S., & Kreasuwun, J. (2010). Mesoscale simulation of a very heavy rainfall event over mumbai, using the weather research and forecasting (wrf) model. *Chiang Mai Journal of Science*, *37*(3), 429–442.

Kishtawal, C. M., & Krishnamurti, T. N. (2001). Diurnal variation of summer rainfall over Taiwan and its detection using TRMM observations. *Journal of Applied Meteorology*, *40*(3), 331–344. https://doi.org/10.1175/1520-0450(2001)040<0331:DVOSRO>2.0.CO;2

Klein, C., Heinzeller, D., Bliefernicht, J., & Kunstmann, H. (2015). Variability of West African monsoon patterns generated by a WRF multi-physics ensemble. *Climate Dynamics*, *45*(9–10), 2733–2755. https://doi.org/10.1007/s00382-015-2505-5

Klemp, J. B., Skamarock, W. C., & Dudhia, J. (2007). Conservative split-explicit time integration methods for the compressible nonhydrostatic equations. *Monthly Weather Review*, *135*(8), 2897–2913. https://doi.org/10.1175/MWR3440.1

Klutse, N. A. B., Quagraine, K. A., Nkrumah, F., Quagraine, K. T., Berkoh-Oforiwaa, R., Dzrobi, J. F., & Sylla, M. B. (2021). The Climatic Analysis of Summer Monsoon Extreme Precipitation Events over West Africa in CMIP6 Simulations. *Earth Systems and Environment*, *5*(1), 25–41. https://doi.org/10.1007/s41748-021-00203-y

Klutse, N. A. B., Sylla, M. B., Diallo, I., Sarr, A., Dosio, A., Diedhiou, A., Kamga, A., Lamptey, B., Ali, A., Gbobaniyi, E. O., Owusu, K., Lennard, C., Hewitson, B., Nikulin, G., Panitz, H. J., & Büchner, M. (2016). Daily characteristics of West African summer monsoon precipitation in CORDEX simulations. *Theoretical and Applied Climatology*, *123*(1–2), 369–386. https://doi.org/10.1007/s00704-014-1352-3

Køltzow, M. A. Ø., Iversen, T., & Haugen, J. E. (2011). The importance of lateral boundaries, surface forcing and choice of domain size for dynamical downscaling of global climate simulations. *Atmosphere*, *2*(2), 67–95.

https://doi.org/10.3390/atmos2020067

Komi, K., Neal, J., Trigg, M. A., & Diekkrüger, B. (2017). Modelling of flood hazard extent in data sparse areas: a case study of the Oti River basin, West Africa. *Journal of Hydrology: Regional Studies*, *10*, 122–132. https://doi.org/10.1016/j.ejrh.2017.03.001

Kotamarthi, V. R., & Feng, Y. (2016). *MPAS Atmospheric Boundary Layer Simulation under Selected Stability Conditions: Evaluation Using the SWIFT Datasen*. https://doi.org/10.2172/1332759

Kramer, M., Heinzeller, D., Hartmann, H., van den Berg, W., & Steeneveld, G. J. (2018). Assessment of MPAS variable resolution simulations in the grey-zone of convection against WRF model results and observations: An MPAS feasibility study of three extreme weather events in Europe. *Climate Dynamics*, *0*(0), 0. https://doi.org/10.1007/s00382-018-4562-z

Kramer, M., Heinzeller, D., Hartmann, H., van den Berg, W., & Steeneveld, G. J. (2020). Assessment of MPAS variable resolution simulations in the grey-zone of convection against WRF model results and observations: An MPAS feasibility study of three extreme weather events in Europe. *Climate Dynamics*, *55*(1–2), 253–276. https://doi.org/10.1007/s00382-018-4562-z

Krishnamurti, T. N., & Kishtawal, C. M. (2000). A pronounced continental-scale diurnal mode of the Asian summer monsoon. *Monthly Weather Review*, *128*(2), 462–473. https://doi.org/10.1175/1520-0493(2000)128<0462:APCSDM>2.0.CO;2

Krishnamurti, T. N., Stefanova, L., Misra, V., & Introduction, A. (2014). Tropical meteorology: an introduction. In *Choice Reviews Online* (Vol. 51, Issue 06). https://doi.org/10.5860/choice.51-3261

Kupfer, S., Santamaria-Aguilar, S., Van Niekerk, L., Lück-Vogel, M., & Vafeidis, A. T. (2022). Investigating the interaction of waves and river discharge during compound flooding at Breede Estuary, South Africa. *Natural Hazards and Earth System Sciences*, *22*(1), 187–205. https://doi.org/10.5194/nhess-22-187-2022

Kwawuvi, D., Mama, D., Agodzo, S. K., Hartmann, A., Larbi, I., Bessah, E., Abraham, T., Dotse, S. Q., & Limantol, A. M. (2022). An investigation into the future changes in rainfall onset, cessation and length of rainy season in the Oti River Basin, West Africa. *Modeling Earth Systems and Environment*, *8*(4), 5077–5095. https://doi.org/10.1007/s40808-022-01410-w

Lafore, J. P., Beucher, F., Peyrillé, P., Diongue-Niang, A., Chapelon, N., Bouniol, D., Caniaux, G., Favot, F., Ferry, F., Guichard, F., Poan, E., Roehrig, R., & Vischel, T. (2017). A multi-scale analysis of the extreme rain event of Ouagadougou in 2009. *Quarterly Journal of the Royal Meteorological Society*, *143*(709), 3094–3109. https://doi.org/10.1002/qj.3165

Láng-Ritter, J., Berenguer, M., Dottori, F., Kalas, M., & Sempere-Torres, D. (2022). Compound flood impact forecasting: Integrating fluvial and flash flood impact assessments into a unified system. *Hydrology and Earth System Sciences*, *26*(3), 689–709. https://doi.org/10.5194/hess-26-689-2022

Lea, D., Yeonsu, K., & Hyunuk, A. (2019). Case study of HEC-RAS 1D-2D coupling simulation: 2002 Baeksan flood event in Korea. *Water (Switzerland)*, *11*(10), 1–

14. https://doi.org/10.3390/w11102048

Lee, M., Schubert, S. D., Suarez, M. J., Bell, T. L., & Kim, K. (2007). *Diurnal cycle of precipitation in the NASA Seasonal to Interannual Prediction Project atmospheric general circulation model*. *112*, 1–12. https://doi.org/10.1029/2006JD008346

Legras, B. (n.d.). *Thermodynamics of convection in the moist atmosphere*. 1–82.

Letson, F., Shepherd, T. J., Barthelmie, R. J., & Pryor, S. C. (2020). Modelling Hail and Convective storms with WRF for Wind Energy Applications. *Journal of Physics: Conference Series*, *1452*(1). https://doi.org/10.1088/1742-6596/1452/1/012051

Li, J., Chen, H., Rong, X., Su, J., Xin, Y., Furtado, K., Milton, S., & Li, N. (2018). How well can a climate model simulate an extreme precipitation event: A case study using the transpose-AMIP experiment. *Journal of Climate*, *31*(16), 6543–6556. https://doi.org/10.1175/JCLI-D-17-0801.1

Li, X., Sui, C. H., Lau, K. M., & Chou, M. D. (1999). Large-scale forcing and cloud-radiation interaction in the tropical deep convective regime. *Journal of the Atmospheric Sciences*, *56*(17), 3028–3042. https://doi.org/10.1175/1520-0469(1999)056<3028:LSFACR>2.0.CO;2

Lian, Y., Chan, I. C., Singh, J., Demissie, M., Knapp, V., & Xie, H. (2007). Coupling of hydrologic and hydraulic models for the Illinois River Basin. *Journal of Hydrology*, *344*(3–4), 210–222. https://doi.org/10.1016/j.jhydrol.2007.08.004

Liu, C., Ikeda, K., Thompson, G., Rasmussen, R., & Dudhia, J. (2011). High-resolution simulations of wintertime precipitation in the Colorado headwaters region: Sensitivity to physics parameterizations. *Monthly Weather Review*, *139*(11), 3533–3553. https://doi.org/10.1175/MWR-D-11-00009.1

Liu, C., & Moncrieff, M. W. (1998). A numerical study of the diurnal cycle of tropical oceanic convection. *Journal of the Atmospheric Sciences*, *55*(13), 2329–2344. https://doi.org/10.1175/1520-0469(1998)055<2329:ANSOTD>2.0.CO;2

Liu, W., Cook, K. H., & Vizy, E. K. (2019). The role of mesoscale convective systems in the diurnal cycle of rainfall and its seasonality over sub-Saharan Northern Africa. *Climate Dynamics*, *52*(1–2), 729–745. https://doi.org/10.1007/s00382-018-4162-y

Liu, X., Bai, A., & Liu, C. (2009). Diurnal variations of summertime precipitation over the Tibetan Plateau in relation to orographically-induced regional circulations. *Environmental Research Letters*, *4*(4). https://doi.org/10.1088/1748-9326/4/4/045203

Mahmood, S., Rahman, A. ur, & Shaw, R. (2019). Spatial appraisal of flood risk assessment and evaluation using integrated hydro-probabilistic approach in Panjkora River Basin, Pakistan. *Environmental Monitoring and Assessment*, *191*(9). https://doi.org/10.1007/s10661-019-7746-z

Malede, D. A., Agumassie, T. A., Kosgei, J. R., Linh, N. T. T., & Andualem, T. G. (2022). Analysis of rainfall and streamflow trend and variability over Birr River watershed, Abbay basin, Ethiopia. *Environmental Challenges*, *7*(April), 100528. https://doi.org/10.1016/j.envc.2022.100528

Malik, S., Pal, S. C., Sattar, A., Singh, S. K., Das, B., Chakrabortty, R., & Mohammad,

P. (2020). Trend of extreme rainfall events using suitable Global Circulation Model to combat the water logging condition in Kolkata Metropolitan Area. *Urban Climate*, *32*(January), 100599. https://doi.org/10.1016/j.uclim.2020.100599

Manatsa, D., Chingombe, W., & Matarira, C. H. (2008). The impact of the positive Indian Ocean dipole on Zimbabwe droughts Tropical climate is understood to be dominated by. *International Journal of Climatology*, *2029*(March 2008), 2011–2029. https://doi.org/10.1002/joc

Manfreda, S., Samela, C., Gioia, A., Consoli, G. G., Iacobellis, V., Giuzio, L., Cantisani, A., & Sole, A. (2015). Flood-prone areas assessment using linear binary classifiers based on flood maps obtained from 1D and 2D hydraulic models. *Natural Hazards*, *79*(2), 735–754. https://doi.org/10.1007/s11069-015-1869-5

Mangukiya, N. K., & Yadav, S. M. (2022). Integrating 1D and 2D hydrodynamic models for semi-arid river basin flood simulation. *International Journal of Hydrology Science and Technology*, *14*(2), 206–228. https://doi.org/10.1504/IJHST.2021.10035928

Maoyi, M. L., & Abiodun, B. J. (2021). How well does MPAS-atmosphere simulate the characteristics of the Botswana High? *Climate Dynamics*, *57*(7–8), 2109–2128. https://doi.org/10.1007/s00382-021-05797-7

Maoyi, M. L., Abiodun, B. J., Prusa, J. M., & Veitch, J. J. (2018). Simulating the characteristics of tropical cyclones over the South West Indian Ocean using a Stretched-Grid Global Climate Model. *Climate Dynamics*, *50*(5–6), 1581–1596. https://doi.org/10.1007/s00382-017-3706-x

Marbaix, P., Gallée, H., Brasseur, O., & van Ypersele, J. P. (2003). Lateral boundary conditions in regional climate models: A detailed study of the relaxation procedure. *Monthly Weather Review*, *131*(3), 461–479. https://doi.org/10.1175/1520-0493(2003)131<0461:LBCIRC>2.0.CO;2

Martinez-Villalobos, C., & Neelin, J. D. (2021). Climate models capture key features of extreme precipitation probabilities across regions. *Environmental Research Letters*, *16*(2). https://doi.org/10.1088/1748-9326/abd351

Mathon, V., & Laurent, H. (2001). Life cycle of Sahelian mesoscale convective cloud systems. *Quarterly Journal of the Royal Meteorological Society*, *127*(572), 377–406. https://doi.org/10.1256/smsqj.57207

Mawulolo, Y. (2018). *Master Dissertation Submitted in partial fulfilment of the requirements for the Master Degree in Presented by CHALLENGING ENVIRONMENT : CASE STUDY OF*. 2017–2018.

McDonald, A. (2000). Boundary conditions for semi-Lagrangian schemes: Testing some alternatives in one-dimensional models. *Monthly Weather Review*, *128*(12), 4084–4096. https://doi.org/10.1175/1520-0493(2000)129<4084:BCFSLS>2.0.CO;2

Mcmillen, J. D., & Steenburgh, W. J. (2015). Capabilities and limitations of convection-permitting WRF simulations of lake-effect systems over the great salt lake. *Weather and Forecasting*, *30*(6), 1711–1731. https://doi.org/10.1175/WAF-D-15-0017.1

Mekonnen, A., Schreck, C. J., & Enyew, B. D. (2020). The impact of Kelvin wave activity during dry and wet African summer rainfall years. *Atmosphere*, *11*(6), 1–15. https://doi.org/10.3390/atmos11060568

Michaelis, A. C., Lackmann, G. M., & Robinson, W. A. (2019). Evaluation of a unique approach to high-resolution climate modeling using the Model for Prediction Across Scales-Atmosphere (MPAS-A) version 5.1. *Geoscientific Model Development*, *12*(8), 3725–3743. https://doi.org/10.5194/gmd-12-3725-2019

Michel-kerjan, E., Tramblay, Y., Villarini, G., & Zhang, W. (2020). *Observed changes in flood hazard in Africa OPEN ACCESS*.

Mihu-pintilie, A., Cîmpianu, I., Stoleriu, C. C., & Paveluc, L. E. (2019). Using High-Density LiDAR Data and 2D Streamflow Hydraulic Modeling to Improve Urban Flood Hazard. *Water*.

Mooney, P. A., Mulligan., F. J., & Fealy, R. (2013). Evaluation of the sensitivity of the weather research and forecasting model to parameterization schemes for regional climates of europe over the period 1990-95. *Journal of Climate*, *26*(3), 1002–1017. https://doi.org/10.1175/JCLI-D-11-00676.1

Moshinsky, M. (1959). No Titleيليب. *Nucl. Phys.*, *13*(1), 104–116.

Mourre, L., Condom, T., Junquas, C., Lebel, T., E. Sicart, J., Figueroa, R., & Cochachin, A. (2016). Spatio-temporal assessment of WRF, TRMM and in situ precipitation data in a tropical mountain environment (Cordillera Blanca, Peru). *Hydrology and Earth System Sciences*, *20*(1), 125–141. https://doi.org/10.5194/hess-20-125-2016

Mukherjee, S., Aadhar, S., Stone, D., & Mishra, V. (2018). Increase in extreme precipitation events under anthropogenic warming in India. *Weather and Climate Extremes*, *20*(July 2017), 45–53. https://doi.org/10.1016/j.wace.2018.03.005

Munir, B. A., Ahmad, S. R., & Hafeez, S. (2019). Integrated hazard modeling for simulating torrential stream response to flash flood events. *ISPRS International Journal of Geo-Information*, *9*(1). https://doi.org/10.3390/ijgi9010001

Myhre, G., Alterskjær, K., Stjern, C. W., Hodnebrog, Marelle, L., Samset, B. H., Sillmann, J., Schaller, N., Fischer, E., Schulz, M., & Stohl, A. (2019). Frequency of extreme precipitation increases extensively with event rareness under global warming. *Scientific Reports*, *9*(1), 1–10. https://doi.org/10.1038/s41598-019-52277-4

Nakaegawa, T., Pinzon, R., Fabrega, J., Cuevas, J. A., de Lima, H. A., Cordoba, E., Nakayama, K., Lao, J. I. B., Melo, A. L., Gonzalez, D. A., & Kusunoki, S. (2019). Seasonal changes of the diurnal variation of precipitation in the upper Río Chagres basin, Panamá. *PLoS ONE*, *14*(12), 1–22. https://doi.org/10.1371/journal.pone.0224662

Nguyen, P., Thorstensen, A., Sorooshian, S., Hsu, K., AghaKouchak, A., Sanders, B., Koren, V., Cui, Z., & Smith, M. (2016). A high resolution coupled hydrologic–hydraulic model (HiResFlood-UCI) for flash flood modeling. *Journal of Hydrology*, *541*, 401–420. https://doi.org/10.1016/j.jhydrol.2015.10.047

Nicholson, S. E., & Palao, I. M. (1993). A re-evaluation of rainfall variability in the sahel. Part I. Characteristics of rainfall fluctuations. *International Journal of*

Climatology, *13*(4), 371–389. https://doi.org/10.1002/joc.3370130403

Novella, N., & Thiaw, W. (2004). Africa Rainfall Climatology Version 2. *CWL Publishing Enterprises, Inc., Madison*, *2004*, 352. http://onlinelibrary.wiley.com/doi/10.1002/cbdv.200490137/abstract

Ntajal, J., Lamptey, B. L., & Sogbedji, J. M. (2016). Flood Vulnerability Mapping in the Lower Mono River Basin in Togo, West Africa. *International Journal of Scientific & Engineering Research*, *7*(10), 1553–1562. https://www.ijser.org/research-paper-publishing-october-2016_page6.aspx

Ntanganedzeni, B., & Nobert, J. (2021). Flood risk assessment in Luvuvhu river, Limpopo province, South Africa. *Physics and Chemistry of the Earth*, *124*(October), 102959. https://doi.org/10.1016/j.pce.2020.102959

Ogwang, B. A., Chen, H., Tan, G., Ongoma, V., & Ntwali, D. (2015). Diagnosis of East African climate and the circulation mechanisms associated with extreme wet and dry events: A study based on RegCM4. *Arabian Journal of Geosciences*, *8*(12), 10255–10265. https://doi.org/10.1007/s12517-015-1949-6

Olanrewaju, C. C., & Reddy, M. (2022). Assessment and prediction of flood hazards using standardized precipitation index—A case study of eThekwini metropolitan area. *Journal of Flood Risk Management*, *15*(2), 1–12. https://doi.org/10.1111/jfr3.12788

Ongdas, N., Akiyanova, F., Karakulov, Y., & Muratbayeva, A. (2020). Application of HEC-RAS (2D) for Flood Hazard Maps. *Mdpi*, *12*(2672), 20.

Ongoma, V., Chena, H., & Gaoa, C. (2018). Projected changes in mean rainfall and temperature over east Africa based on CMIP5 models. *International Journal of Climatology*, *38*(3), 1375–1392. https://doi.org/10.1002/joc.5252

Ou, T., Chen, D., Linderholm, H. W., & Jeong, J. H. (2013). Evaluation of global climate models in simulating extreme precipitation in China. *Tellus, Series A: Dynamic Meteorology and Oceanography*, *65*, 1–16. https://doi.org/10.3402/tellusa.v65i0.19799

Ouikotan, B. ., Van der Kwast, J., Mynett, A., & Afouda, A. (2017). Gaps and challenges of flood risk management in West African coastal cities. *16th World Water Congress*, 1–12.

Ozdemir, H., Sampson, C. C., De Almeida, G. A. M., & Bates, P. D. (2013). Evaluating scale and roughness effects in urban flood modelling using terrestrial LIDAR data. *Hydrology and Earth System Sciences*, *17*(10), 4015–4030. https://doi.org/10.5194/hess-17-4015-2013

Paeth, H., Fink, A. H., Pohle, S., Keis, F., & Hermann, M. (2011). *Meteorological characteristics and potential causes of the 2007 flood in sub-Saharan Africa*. *1926*(July 2010), 1908–1926. https://doi.org/10.1002/joc.2199

Park, M. S., Ho, C. H., Kim, J., & Elsberry, R. L. (2011). Diurnal circulations and their multi-scale interaction leading to rainfall over the South China Sea upstream of the Philippines during intraseasonal monsoon westerly wind bursts. *Climate Dynamics*, *37*(7–8), 1483–1499. https://doi.org/10.1007/s00382-010-0922-z

Parker, D. J., Burton, R. R., Diongue-Niang, A., Ellis, R. J., Felton, M., Taylor, C. M.,

Thorncroft, C. D., Bessemoulin, P., & Tompkins, A. M. (2005). The diurnal cycle of the West African monsoon circulation. *Quarterly Journal of the Royal Meteorological Society*, *131*(611), 2839–2860. https://doi.org/10.1256/qj.04.52

Patra, J. P., Kumar, R., & Mani, P. (2016). Combined Fluvial and Pluvial Flood Inundation Modelling for a Project Site. *Procedia Technology*, *24*, 93–100. https://doi.org/10.1016/j.protcy.2016.05.014

Peel, M., Finlayson, B., & McMahon, T. (2007). Updated world map of the Köppen-Geiger climate classification. *Hydrology and Earth System Sciences*, *11*(5), 1633–1644. https://doi.org/10.1002/ppp.421

Pérez-Méndez, M., Tejeda-Martínez, A., & Fitzjarrald, D. R. (2019). Diurnal variation of rainfall in a tropical coastal region with complex orography. *Atmosphere*, *10*(10), 1–19. https://doi.org/10.3390/atmos10100604

Pilon, R., Zhang, C., & Dudhia, J. (1955). Journal of geophysical research. *Nature*, *175*(4449), 238. https://doi.org/10.1038/175238c0

Pilon, R., Zhang, C., & Dudhia, J. (2016). Journal of geophysical research. *Nature*, *175*(4449), 238. https://doi.org/10.1038/175238c0

Pinos, J., & Timbe, L. (2019). Performance assessment of two-dimensional hydraulic models for generation of flood inundation maps in mountain river basins. *Water Science and Engineering*, *12*(1), 11–18. https://doi.org/10.1016/j.wse.2019.03.001

Pinos, J., Timbe, L., & Timbe, E. (2019). Evaluation of 1D hydraulic models for the simulation of mountain fluvial floods: A case study of the santa bárbara river in Ecuador. *Water Practice and Technology*, *14*(2), 341–354. https://doi.org/10.2166/wpt.2019.018

Preisser, M., Passalacqua, P., Bixler, R. P., & Hofmann, J. (2022). Intersecting near-real time fluvial and pluvial inundation estimates with sociodemographic vulnerability to quantify a household flood impact index. *Hydrology and Earth System Sciences*, *26*(15), 3941–3964. https://doi.org/10.5194/hess-26-3941-2022

Pribadi, A., Wongwises, P., Humphries, U., Limsakul, A., & Wangwongchai, A. (2012). Diurnal Rainfall Variation over Three Rainfall Regions within Indonesia Based on Ten Years of TRMM Data. *Journal of Sustainable Energy & Environment*, *3*(February 2015), 81–86. http://www.jgsee.kmutt.ac.th/jsee/JSEE 2012/PDF file_JSEE 3(2) 2012/11. Diurnal Rainfall pp. 81-86.pdf

Qian, W. (2017). *Temporal Climatology and Anomalous Weather Analysis*. https://doi.org/10.1007/978-981-10-3641-5

Qian, W., Du, J., Shan, X., & Jiang, N. (2015). Incorporating the effects of moisture into a dynamical parameter: Moist vorticity and moist divergence. *Weather and Forecasting*, *30*(6), 1411–1428. https://doi.org/10.1175/WAF-D-14-00154.1

Ramachandran, A., Palanivelu, K., Mudgal, B. V., Jeganathan, A., Guganesh, S., Abinaya, B., & Elangovan, A. (2019). Climate change impact on fluvial flooding in the Indian sub-basin: A case study on the Adyar sub-basin. *PLoS ONE*, *14*(5), 1–24. https://doi.org/10.1371/journal.pone.0216461

Rana, V. K., & Suryanarayana, T. M. V. (2021). Estimation of flood influencing characteristics of watershed and their impact on flooding in data-scarce region.

Annals of GIS, *27*(4), 397–418. https://doi.org/10.1080/19475683.2021.1960603

Rangari, V. A., Umamahesh, N. V., & Bhatt, C. M. (2019a). Assessment of inundation risk in urban floods using HEC RAS 2D. *Modeling Earth Systems and Environment*, *5*(4), 1839–1851. https://doi.org/10.1007/s40808-019-00641-8

Rangari, V. A., Umamahesh, N. V., & Bhatt, C. M. (2019b). Assessment of inundation risk in urban floods using HEC RAS 2D. *Modeling Earth Systems and Environment*, *5*(4), 1839–1851. https://doi.org/10.1007/s40808-019-00641-8

Reay, D., Sabine, C., Smith, P., & Hymus, G. (2007). Intergovernmental Panel on Climate Change. Fourth Assessment Report. Geneva, Switzerland: Inter-governmental Panel on Climate Change. Cambridge; UK: Cambridge University Press; 2007. Available from: www. ipcc.ch. In *Intergovernmental Panel on Climate Change*. https://doi.org/10.1038/446727a

Rienecker, M. M., Suarez, M. J., Gelaro, R., Todling, R., Bacmeister, J., Liu, E., Bosilovich, M. G., Schubert, S. D., Takacs, L., Kim, G. K., Bloom, S., Chen, J., Collins, D., Conaty, A., Da Silva, A., Gu, W., Joiner, J., Koster, R. D., Lucchesi, R., … Woollen, J. (2011). MERRA: NASA's modern-era retrospective analysis for research and applications. *Journal of Climate*, *24*(14), 3624–3648. https://doi.org/10.1175/JCLI-D-11-00015.1

Ringler, T. D., Thuburn, J., Klemp, J. B., & Skamarock, W. C. (2010). A unified approach to energy conservation and potential vorticity dynamics for arbitrarily-structured C-grids. *Journal of Computational Physics*, *229*(9), 3065–3090. https://doi.org/10.1016/j.jcp.2009.12.007

Ringler, T., Ju, L., & Gunzburger, M. (2008). A multiresolution method for climate system modeling: Application of spherical centroidal Voronoi tessellations. *Ocean Dynamics*, *58*(5–6), 475–498. https://doi.org/10.1007/s10236-008-0157-2

Risanto, C. B., Castro, C. L., Moker, J. M., Arellano, A. F., Adams, D. K., Fierro, L. M., & Sosa, C. M. M. (2019). Evaluating forecast skills of moisture from convective-permitting WRF-ARW Model during 2017 North American Monsoon season. *Atmosphere*, *10*(11). https://doi.org/10.3390/atmos10110694

Rizeei, H. M., Pradhan, B., & Saharkhiz, M. A. (2019). An integrated fluvial and flash pluvial model using 2D high-resolution sub-grid and particle swarm optimization-based random forest approaches in GIS. *Complex and Intelligent Systems*, *5*(3), 283–302. https://doi.org/10.1007/s40747-018-0078-8

Rosa, D., & Collins, W. D. (2013). A case study of subdaily simulated and observed continental convective precipitation: CMIP5 and multiscale global climate models comparison. *Geophysical Research Letters*, *40*(22), 5999–6003. https://doi.org/10.1002/2013GL057987

Rosbjerg, D., Blöschl, G., Burn, D. H., Castellarin, A., Croke, B., Di Baldassarre, G., Iacobellis, V., Kjeldsen, T. R., Kuczera, G., Merz, R., Montanari, A., Morris, D., Ouarda, T. B. M. J., Ren, L., Rogger, M., Salinas, J. L., Toth, E., & Viglione, A. (2013). Prediction of floods in ungauged basins. In *Runoff Prediction in Ungauged Basins*. https://doi.org/10.1017/cbo9781139235761.012

Rouault, M., Roy, S. Sen, & Balling, R. C. (2013). The diurnal cycle of rainfall in South Africa in the austral summer. *International Journal of Climatology*, *33*(3), 770–

777. https://doi.org/10.1002/joc.3451

Roxy, M. K., Ghosh, S., Pathak, A., Athulya, R., Mujumdar, M., Murtugudde, R., Terray, P., & Rajeevan, M. (2017). A threefold rise in widespread extreme rain events over central India. *Nature Communications*, *8*(1), 1–11. https://doi.org/10.1038/s41467-017-00744-9

Rummukainen, M. (2010). State-of-the-art with regional. *Clim Change*, *1*(1), 82–96. https://doi.org/10.1002/wcc.008

Saha, S., Moorthi, S., Pan, H. L., Wu, X., Wang, J., Nadiga, S., Tripp, P., Kistler, R., Woollen, J., Behringer, D., Liu, H., Stokes, D., Grumbine, R., Gayno, G., Wang, J., Hou, Y. T., Chuang, H. Y., Juang, H. M. H., Sela, J., … Goldberg, M. (2010). The NCEP climate forecast system reanalysis. *Bulletin of the American Meteorological Society*, *91*(8), 1015–1057. https://doi.org/10.1175/2010BAMS3001.1

Salathé, E. P., Leung, L. R., Qian, Y., & Zhang, Y. (2010). Regional climate model projections for the State of Washington. *Climatic Change*, *102*(1–2), 51–75. https://doi.org/10.1007/s10584-010-9849-y

Samimi, C., Fink, A. H., & Paeth, H. (2012). The 2007 flood in the Sahel: Causes, characteristics and its presentation in the media and FEWS NET. *Natural Hazards and Earth System Science*, *12*(2), 313–325. https://doi.org/10.5194/nhess-12-313-2012

Sane, Y., Bonazzola, M., Rio, C., Chambon, P., Fiolleau, T., Musat, I., Hourdin, F., Roca, R., Grandpeix, J. Y., & Diedhiou, A. (2012). An analysis of the diurnal cycle of precipitation over Dakar using local rain-gauge data and a general circulation model. *Quarterly Journal of the Royal Meteorological Society*, *138*(669), 2182–2195. https://doi.org/10.1002/qj.1932

Sarchani, S., Seiradakis, K., Coulibaly, P., & Tsanis, I. (2020). Flood inundation mapping in an ungauged basin. *Water (Switzerland)*, *12*(6), 1–21. https://doi.org/10.3390/W12061532

Schwartz, C. S. (2019). Medium-range convection-allowing ensemble forecasts with a variable-resolution global model. *Monthly Weather Review*, *147*(8), 2997–3023. https://doi.org/10.1175/MWR-D-18-0452.1

Schwartz1, C. S. (2014). Journal of Advances in Modeling Earth Systems. *Journal of Advances in Modeling Earth Systems*, *6*, 513–526. https://doi.org/10.1002/2014MS000363.Received

Sharma, V. C., & Regonda, S. K. (2021). Two-dimensional flood inundation modeling in the godavari river basin, India—insights on model output uncertainty. *Water (Switzerland)*, *13*(2). https://doi.org/10.3390/w13020191

Shinoda, M., Okatani, T., & Saloum, M. (1999). Diurnal variations of rainfall over Niger in the West African Sahel: A comparison between wet and drought years. *International Journal of Climatology*, *19*(1), 81–94. https://doi.org/10.1002/(SICI)1097-0088(199901)19:1<81::AID-JOC350>3.0.CO;2-F

Shustikova, I., Domeneghetti, A., Neal, J. C., Bates, P., & Castellarin, A. (2019).

Comparing 2D capabilities of HEC-RAS and LISFLOOD-FP on complex topography. *Hydrological Sciences Journal*, *64*(14), 1769–1782. https://doi.org/10.1080/02626667.2019.1671982

Skamarock, W. C., & Gassmann, A. (2011). Conservative transport schemes for spherical geodesic grids: High-order flux operators for ODE-based time integration. *Monthly Weather Review*, *139*(9), 2962–2975. https://doi.org/10.1175/MWR-D-10-05056.1

Skamarock, W. C., Klemp, J. B., Duda, M. G., Fowler, L. D., Park, S. H., & Ringler, T. D. (2012). A multiscale nonhydrostatic atmospheric model using centroidal Voronoi tesselations and C-grid staggering. *Monthly Weather Review*, *140*(9), 3090–3105. https://doi.org/10.1175/MWR-D-11-00215.1

Skamarock, W. C., Ringler, T., Klemp, J. B., Thuburn, J., Duda, M. G., Gunzburger, M., Ju, L., Park, S. H., & Fowler, L. (2010). Global Non-Hydrostatic Modeling Using Voronoi Meshes: The MPAS Model. *ECMWF Workshop on Non-Hydrostatic Modelling*, *November*, 8–10.

Sow, M., Diakhaté, M., Dixon, R. D., Guichard, F., Dieng, D., & Gaye, A. T. (2020). Uncertainties in the annual cycle of rainfall characteristics over West Africa in CMIP5 models. *Atmosphere*, *11*(2), 1–28. https://doi.org/10.3390/atmos11020216

Subrahmanyam, K. V., Kishore Kumar, K., & Babu, A. N. (2015). Phase relation between CAPE and precipitation at diurnal scales over the Indian summer monsoon region. *Atmospheric Science Letters*, *16*(3), 346–354. https://doi.org/10.1002/asl2.566

Sui, C. H., Li, X., & Lau, K. M. (1998). Radiative-convective processes in simulated diurnal variations of tropical oceanic convection. *Journal of the Atmospheric Sciences*, *55*(13), 2345–2357. https://doi.org/10.1175/1520-0469(1998)055<2345:RCPISD>2.0.CO;2

Sultan, B., & Gaetani, M. (2016). Agriculture in West Africa in the twenty-first century: Climate change and impacts scenarios, and potential for adaptation. *Frontiers in Plant Science*, *7*(AUG2016), 1–20. https://doi.org/10.3389/fpls.2016.01262

Sultan, B., Janicot, S., & Drobinski, P. (2007). Characterization of the diurnal cycle of the West African monsoon around the monsoon onset. *Journal of Climate*, *20*(15), 4014–4032. https://doi.org/10.1175/JCLI4218.1

Sylla, B. M., Kebe, I., Nikiema, P. N., & Klutse, B. N. (2016). Adaptation to climate change and variability in rural West Africa. *Adaptation to Climate Change and Variability in Rural West Africa*, *April*, 1–244. https://doi.org/10.1007/978-3-319-31499-0

Sylla, M. B., Coppola, E., Mariotti, L., Giorgi, F., Ruti, P. M., Dell'Aquila, A., & Bi, X. (2010). Multiyear simulation of the African climate using a regional climate model (RegCM3) with the high resolution ERA-interim reanalysis. *Climate Dynamics*, *35*(1), 231–247. https://doi.org/10.1007/s00382-009-0613-9

Sylla, M. B., Giorgi, F., Coppola, E., & Mariotti, L. (2013). Uncertainties in daily rainfall over Africa: Assessment of gridded observation products and evaluation of a regional climate model simulation. *International Journal of Climatology*, *33*(7), 1805–1817. https://doi.org/10.1002/joc.3551

Sylla, M. B., Giorgi, F., Pal, J. S., Gibba, P., Kebe, I., & Nikiema, M. (2015). Projected changes in the annual cycle of high-intensity precipitation events over West Africa for the late twenty-first century. *Journal of Climate*, *28*(16), 6475–6488. https://doi.org/10.1175/JCLI-D-14-00854.1

Sylla, M. B., Nikiema, P. M., Gibba, P., Kebe, I., & Klutse, N. A. B. (2016). Adaptation to climate change and variability in rural West Africa. *Adaptation to Climate Change and Variability in Rural West Africa*, 1–244. https://doi.org/10.1007/978-3-319-31499-0

Sylla, M. B., Pal, J. S., Wang, G. L., & Lawrence, P. J. (2016). Impact of land cover characterization on regional climate modeling over West Africa. *Climate Dynamics*, *46*(1–2), 637–650. https://doi.org/10.1007/s00382-015-2603-4

Ta, S., Kouadio, K. Y., Ali, K. E., Toualy, E., Aman, A., & Yoroba, F. (2016). West Africa Extreme Rainfall Events and Large-Scale Ocean Surface and Atmospheric Conditions in the Tropical Atlantic. *Advances in Meteorology*, *2016*, 14. https://doi.org/10.1155/2016/1940456

Tanessong, R. S., Vondou, D. A., Djomou, Z. Y., & Igri, P. M. (2017). WRF high resolution simulation of an extreme rainfall event over Douala (Cameroon): a case study. *Modeling Earth Systems and Environment*, *3*(3), 927–942. https://doi.org/10.1007/s40808-017-0343-7

Tang, B., Hu, W., & Duan, A. (2021). Assessment of extreme precipitation indices over Indochina and South China in CMIP6 models. *Journal of Climate*, *34*(18), 7507–7524. https://doi.org/10.1175/JCLI-D-20-0948.1

Tao, H. C., Lei, T., Shi, G., Sun, X. N., Wei, X. Y., Zhang, L. J., & Wu, W. M. (2014). Removal of heavy metals from fly ash leachate using combined bioelectrochemical systems and electrolysis. *Journal of Hazardous Materials*, *264*(May), 1–7. https://doi.org/10.1016/j.jhazmat.2013.10.057

Tao, W. K., Lang, S., Simpson, J., Sui, C. H., Ferrier, B., & Chou, M. D. (1996). Mechanisms of cloud-radiation interaction in the tropics and midlatitudes. In *Journal of the Atmospheric Sciences* (Vol. 53, Issue 18, pp. 2624–2651). https://doi.org/10.1175/1520-0469(1996)053<2624:MOCRII>2.0.CO;2

Taylor, M. A., Edwards, J., & Cyr, A. S. (2008). Petascale atmospheric models for the Community Climate System Model: New developments and evaluation of scalable dynamical cores. *Journal of Physics: Conference Series*, *125*, 1–10. https://doi.org/10.1088/1742-6596/125/1/012023

Teng, J., Jakeman, A. J., Vaze, J., Croke, B. F. W., Dutta, D., & Kim, S. (2017). Flood inundation modelling: A review of methods, recent advances and uncertainty analysis. *Environmental Modelling and Software*, *90*, 201–216. https://doi.org/10.1016/j.envsoft.2017.01.006

Thuburn, J., Ringler, T. D., Skamarock, W. C., & Klemp, J. B. (2009). Numerical representation of geostrophic modes on arbitrarily structured C-grids. *Journal of Computational Physics*, *228*(22), 8321–8335. https://doi.org/10.1016/j.jcp.2009.08.006

Tian, X., & Ide, K. (2021). Hurricane predictability analysis with singular vectors in the multiresolution global shallow water model. *Journal of the Atmospheric Sciences*,

78(4), 1259–1273. https://doi.org/10.1175/JAS-D-20-0238.1

Tiepolo, M., Belcore, E., Braccio, S., Issa, S., Massazza, G., Rosso, M., & Tarchiani, V. (2021). Method for fluvial and pluvial flood risk assessment in rural settlements. *MethodsX*, *8*, 101463. https://doi.org/10.1016/j.mex.2021.101463

Tiepolo, M., Braccio, S., Fiorillo, E., Galligari, A., Katiellou, G. L., Massazza, G., Sitta, A. A., Tankari, A. M., & Tarchiani, V. (2021). Method for pluvial flood risk assessment in rural settlements characterised by scant information availability. *MethodsX*, *8*(September), 101532. https://doi.org/10.1016/j.mex.2021.101532

Tiepolo, M., Rosso, M., Massazza, G., Belcore, E., Issa, S., & Braccio, S. (2019). Flood assessment for risk-informed planning along the Sirba River, Niger. *Sustainability (Switzerland)*, *11*(15). https://doi.org/10.3390/su11154003

Trenberth, K. E., Smith, L., Qian, T., Dai, A., & Fasullo, J. (2007). Estimates of the global water budget and its annual cycle using observational and model Data. *Journal of Hydrometeorology*, *8*(4), 758–769. https://doi.org/10.1175/JHM600.1

Tschakert, P., Sagoe, R., Ofori-Darko, G., & Codjoe, S. N. (2010). Floods in the Sahel: An analysis of anomalies, memory, and anticipatory learning. *Climatic Change*, *103*(3), 471–502. https://doi.org/10.1007/s10584-009-9776-y

Urzică, A., Mihu-Pintilie, A., Stoleriu, C. C., Cîmpianu, C. I., Huţanu, E., Pricop, C. I., & Grozavu, A. (2021). Using 2D HEC-RAS modeling and embankment dam break scenario for assessing the flood control capacity of a multireservoir system (Ne Romania). *Water (Switzerland)*, *13*(1), 1–28. https://doi.org/10.3390/w13010057

Version, M. (1989). Guide for Selecting Manning ' s Roughness Coefficients for Natural Channels and Flood Plains United States Geological Survey Water-supply Paper 2339. *Area*, *2339*(2339), 39. http://www.fhwa.dot.gov/BRIDGE/wsp2339.pdf

Vizy, E. K., & Cook, K. H. (2012). Mid-twenty-first-century changes in extreme events over northern and tropical Africa. *Journal of Climate*, *25*(17), 5748–5767. https://doi.org/10.1175/JCLI-D-11-00693.1

Wagner, S., Souvignet, M., Walz, Y., Balogun, K., Komi, K., Kreft, S., & Rhyner, J. (2021). When does risk become residual? A systematic review of research on flood risk management in West Africa. *Regional Environmental Change*, *21*(3), 1–18. https://doi.org/10.1007/s10113-021-01826-7

Wahl, T., Jain, S., Bender, J., Meyers, S. D., & Luther, M. E. (2015). Increasing risk of compound flooding from storm surge and rainfall for major US cities. *Nature Climate Change*, *5*(12), 1093–1097. https://doi.org/10.1038/nclimate2736

Wang, J., Kim, H., Kim, D., Henderson, S. A., Stan, C., & Maloney, E. D. (2020). MJO teleconnections over the PNA region in climate models. Part I: Performance- And process-based skill metrics. *Journal of Climate*, *33*(3), 1051–1067. https://doi.org/10.1175/JCLI-D-19-0253.1

Wang, Y., Leung, L. R., McGregor, J. L., Lee, D. K., Wang, W. C., Ding, Y., & Kimura, F. (2004). Regional climate modeling: Progress, challenges, and prospects. *Journal of the Meteorological Society of Japan*, *82*(6), 1599–1628. https://doi.org/10.2151/jmsj.82.1599

Washington, W. M., Buja, L., & Craig, A. (2009). The computational future for climate

and Earth system models: On the path to petaflop and beyond. *Philosophical Transactions of the Royal Society A: Mathematical, Physical and Engineering Sciences*, *367*(1890), 833–846. https://doi.org/10.1098/rsta.2008.0219

Watters, D., & Battaglia, A. (2019). The summertime diurnal cycle of precipitation derived from IMERG. *Remote Sensing*, *11*(15), 1–17. https://doi.org/10.3390/rs11151781

Weedon, G. P., Balsamo, G., Bellouin, N., Gomes, S., Best, M. J., & Viterbo, P. (2014). Data methodology applied to ERA-Interim reanalysis data. *Water Resources Research*, *50*, 7505–7514. https://doi.org/10.1002/2014WR015638.Received

Wehner, M., Lee, J., Risser, M., Ullrich, P., Gleckler, P., & Collins, W. D. (2021). Evaluation of extreme sub-daily precipitation in high-resolution global climate model simulations. *Philosophical Transactions of the Royal Society A: Mathematical, Physical and Engineering Sciences*, *379*(2195). https://doi.org/10.1098/rsta.2019.0545

Williamson, D. L. (2007). The evolution of dynamical cores for global atmospheric models. *Journal of the Meteorological Society of Japan*, *85 B*, 241–269. https://doi.org/10.2151/jmsj.85B.241

Wu, L., Shao, Y., & Cheng, A. Y. S. (2011). A diagnostic study of two heavy rainfall events in South China. *Meteorology and Atmospheric Physics*, *111*(1), 13–25. https://doi.org/10.1007/s00703-010-0112-x

Wu, M. L. C., Reale, O., & Schubert, S. D. (2013). A characterization of African easterly waves on 2.5-6-day and 6-9-day time scales. *Journal of Climate*, *26*(18), 6750–6774. https://doi.org/10.1175/JCLI-D-12-00336.1

Xiao, C., Yuan, W., & Yu, R. (2018). Diurnal cycle of rainfall in amount, frequency, intensity, duration, and the seasonality over the UK. *International Journal of Climatology*, *38*(13), 4967–4978. https://doi.org/10.1002/joc.5790

Xu, J., Zhang, B., Wang, M., & Wang, H. (2012). Diurnal variation of summer precipitation over the Tibetan Plateau: A cloud-resolving simulation. *Annales Geophysicae*, *30*(11), 1575–1586. https://doi.org/10.5194/angeo-30-1575-2012

Yaro, J. A., & Hesselberg, J. (2016). Adaptation to climate change and variability in rural West Africa. *Adaptation to Climate Change and Variability in Rural West Africa*, *April*, 1–244. https://doi.org/10.1007/978-3-319-31499-0

Ye, S., Li, H. Y., Leung, L. R., Guo, J., Ran, Q., Demissie, Y., & Sivapalan, M. (2017). Understanding flood seasonality and its temporal shifts within the contiguous United States. *Journal of Hydrometeorology*, *18*(7), 1997–2009. https://doi.org/10.1175/JHM-D-16-0207.1

Yomo, M., Mourad, K. A., & Gnazou, M. D. T. (2019). Examining water security in the challenging environment in Togo, West Africa. *Water (Switzerland)*, *11*(2), 1–19. https://doi.org/10.3390/w11020231

Zarzyck, C., & Jablonowski, C. (2014). Journal of Advances in Modeling Earth Systems. *Journal of Advances in Modeling Earth Systems*, *6*, 1065–1094. https://doi.org/10.1002/2014MS000352.Received

Zhang, G., Cook, K. H., & Vizy, E. K. (2016a). The diurnal cycle of warm season

rainfall over West Africa. Part I: Observational analysis. *Journal of Climate*, *29*(23), 8423–8437. https://doi.org/10.1175/JCLI-D-15-0874.1

Zhang, G., Cook, K. H., & Vizy, E. K. (2016b). The diurnal cycle of warm season rainfall over West Africa. Part II: Convection-permitting simulations. *Journal of Climate*, *29*(23), 8439–8454. https://doi.org/10.1175/JCLI-D-15-0875.1

Zhang, L., Cheng, I., Wu, Z., Harner, T., Schuster, J., Charland, J.-P., Muir, D., & Parnis, J. M. (2015). Journal of Advances in Modeling Earth Systems. *Journal of Advances in Modeling Earth Systems*, *7*, 1339–1350. https://doi.org/10.1002/2017MS001065

Zhang, X., Anagnostou, E. N., Frediani, M., Solomos, S., & Kallos, G. (2013). Using NWP simulations in satellite rainfall estimation of heavy precipitation events over mountainous areas. *Journal of Hydrometeorology*, *14*(6), 1844–1858. https://doi.org/10.1175/JHM-D-12-0174.1

Zhang, Y., & Fueglistaler, S. (2020). How Tropical Convection Couples High Moist Static Energy Over Land and Ocean. *Geophysical Research Letters*, *47*(2), 1–8. https://doi.org/10.1029/2019GL086387

Zhang, Z., Li, Y., Chen, F., Barlage, M., & Li, Z. (2018). Evaluation of convection-permitting WRF CONUS simulation on the relationship between soil moisture and heatwaves. *Climate Dynamics*. https://doi.org/10.1007/s00382-018-4508-5

Zhang, Z., Xu, C. Y., El-Tahir, M. E. H., Cao, J., & Singh, V. P. (2012). Spatial and temporal variation of precipitation in Sudan and their possible causes during 1948-2005. *Stochastic Environmental Research and Risk Assessment*, *26*(3), 429–441. https://doi.org/10.1007/s00477-011-0512-6

Zhao, C., Xu, M., Wang, Y., Zhang, M., Guo, J., Hu, Z., Leung, L. R., Duda, M., & Skamarock, W. (2019). Modeling extreme precipitation over East China with a global variable-resolution modeling framework (MPASv5.2): Impacts of resolution and physics. *Geoscientific Model Development*, *12*(7), 2707–2726. https://doi.org/10.5194/gmd-12-2707-2019

Zhao, Y., Wang, M., Li, J., Yang, X., Zhang, N., & Chen, H. (2019). Diurnal Variations in Summer Precipitation over the Yellow River Basin. *Advances in Meteorology*, *2019*. https://doi.org/10.1155/2019/2482656